Fabrication of micro-structured surfaces with increased light absorption and their influence on intense laser-plasma experiments

Herstellung mikrostrukturierter Oberflächen mit erhöhter Lichtabsorption und deren Einfluss auf intensive Laser-Plasma Experimente

Zur Erlangung des Grades eines Doktors der Naturwissenschaften (Dr. rer. nat.)
genehmigte Dissertation von Nico Wilfrid Neumann aus Darmstadt
Tag der Einreichung: 8. Mai 2018, Tag der Prüfung: 6. Juni 2018
Darmstadt — D 17

1. Gutachten: Prof. Dr. Markus Roth
2. Gutachten: Prof. Dr. Thomas Walther

TECHNISCHE UNIVERSITÄT DARMSTADT

Fachbereich Physik
Institut für Kernphysik
Laser und Plasmaphysik

Graduate School of Energy Science and Engineering

Fabrication of micro-structured surfaces with increased light absorption and their influence on intense laser-plasma experiments
Herstellung mikrostrukturierter Oberflächen mit erhöhter Lichtabsorption und deren Einfluss auf intensive Laser-Plasma Experimente

Genehmigte Dissertation von Nico Wilfrid Neumann aus Darmstadt

1. Gutachten: Prof. Dr. Markus Roth
2. Gutachten: Prof. Dr. Thomas Walther

Tag der Einreichung: 8. Mai 2018
Tag der Prüfung: 6. Juni 2018

Darmstadt — D 17

Version: Neumann_2018_Juni_06

Bitte zitieren Sie dieses Dokument als:
URN: urn:nbn:de:tuda-tuprints-74808
URL: http://tuprints.ulb.tu-darmstadt.de/74808

Dieses Dokument wird bereitgestellt von tuprints,
E-Publishing-Service der TU Darmstadt
http://tuprints.ulb.tu-darmstadt.de
tuprints@ulb.tu-darmstadt.de

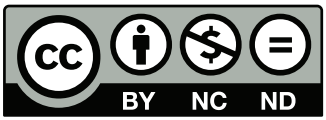

"Fall in love with some activity, and do it! Nobody ever figures out what life is all about, and it doesn't matter. Explore the world. Nearly everything is really interesting if you go into it deeply enough. Work as hard and as much as you want to on the things you like to do the best. Don't think about what you want to be, but what you want to do. Keep up some kind of a minimum with other things so that society doesn't stop you from doing anything at all."

– RICHARD P. FEYNMAN, Surely You're Joking, Mr. Feynman!

Zusammenfassung

Die vorliegende Arbeit untersucht erstmalig den Einfluss stark Licht absobierender mikrostrukturierter Oberflächen auf Laser-Plasma Experimente. Dabei wird die Wechselwirkung eines dünnen Siliziumsubstrats mit ultrakurzen Laserpulsen bei Spitzenintensitäten oberhalb $10^{20}\,\mathrm{W/cm^2}$ untersucht. Durch diesen lasergetriebenen Prozess werden Elektronen auf kürzesten Strecken zu relativistischen Energien und durch das Target beschleunigt. Darüber hinaus werden Ionen senkrecht zu den Oberflächen der Siliziumfolie beschleunigt und intensive elektromagnetische Strahlung erzeugt.

Im Rahmen dieser Arbeit wurde ein Aufbau entwickelt, der es erlaubt variierbare Strukturen in der Größenordnung von Mikrometern auf Siliziumoberflächen zu erzeugen. Dabei werden ultrakurze Laserpulse mit Pulslängen in der Größenordnung von Femtosekunden verwendet um mit einem lasergetriebenen Ablations- und Ätzprozess periodische Oberflächen zu induzieren (engl. *laser-induced periodic surface structures*, kurz LIPSS). Die erzeugten Strukturen bestehen aus runden Siliziumnadeln mit einer signifikant erhöhten Lichtabsorption über einen breiten Bereich des sichtbaren und infraroten Spektrums. Der experimentelle Aufbau wird gemeinsam mit der Charakterisierung relevanter Parameterbereiche demonstriert, die es erlaubt genaue Vorhersagen über die Nadelhöhe und -verteilung zu treffen.

Die mit diesem Aufbau hergestellten Siliziumtargets werden in einem Laser-Plasma Experiment mit üblicherweise eingesetzten flachen Folien und anderen Strukturen mit periodischer Geometrie verglichen. Die strukturierte Fläche zeigt dabei in Richtung des einfallenden Laserpulses. Dafür wurde am *Vulcan* Lasersystem der *Central Laser Facility*, Oxfordshire in Großbritannien eine experimentelle Kampagne ermöglicht. Die Vermessung der spektralen und räumlichen Verteilung von reflektiertem Laserlicht, erzeugter Röntgenstrahlung, sowie der Beschleunigung von Elektronen und Ionen zeigt dabei eine deutliche Verbesserung durch die Verwendung mikrostrukturierter Oberflächen. Die Ausbeute hoch energetischer Elektronen, Ionen und brillanter Röntgenstrahlung ist im Vergleich zu flachen Folien und geometrischen Strukturen deutlich erhöht. Reflexionsverluste von Laserenergie an der Targetoberfläche werden verringert.

Die Ergebnisse und Rückschlüsse aus der experimentellen Kampagne motivieren die Verwendung strukturierter Siliziumoberflächen in Kombination mit weiteren Materialien. Zum Beispiel kann durch eine protonenreiche Schicht

auf der Targetrückseite eine zuverlässige und energiereiche lasergetriebene Protonenquelle erzeugt werden. Des Weiteren kann durch die Kombination der Oberflächenstruktur mit einem räumlich begrenzten Material eine intensive Röntgenquelle mit verringerter Quellgröße generiert werden. Die Energie der charakteristischen Photonen kann dabei durch die Wahl des Materials gezielt gesteuert werden. Durch den im Verlauf dieser Arbeit entwickelten Produktionsaufbau konnten die apparativen Möglichkeiten des *Detektor- und Targetlabors* erweitert werden. Die weitere Entwicklung dieses Aufbaus mit Blick auf hochrepetitive Laser, die einfache und kostengünstige Produktion komplexer Targets und Anwendungen absorbierender Strukturen ist vielversprechend.

Abstract

The thesis reports on the influence of customisable and highly light absorbing surfaces on laser-plasma experiments. For the first time, a thin microstructured silicon substrate is interacting with a short laser pulse with peak intensity exceeding $10^{20}\,\mathrm{W/cm^2}$. In this process, electrons are accelerated and pushed into the target to relativistic energies. Furthermore, ions are accelerated perpendicular to the target surfaces and electromagnetic radiation is generated.
In the framework of this work, a fabrication setup is developed that produces customisable structured silicon surfaces using a laser-assisted ablation and etching process with light pulses of femtosecond pulse length and the effect of *laser-induced periodic surface structures* (LIPSS). The evolving structure consists of conical silicon spikes with a significant increase in light absorption over a broad spectral range in the visible and infrared region. The experimental setup is demonstrated together with a characterisation of the resulting surface structures. Thereby, a precise prediction of needle height and separation is possible.
Following, these structured silicon targets are compared to flat foils and different periodic geometric structures, typically used in laser-plasma experiments, in an experimental campaign using the petawatt class *Vulcan* laser system of the *Central Laser Facility*, Oxfordshire, UK. Spectral and spatial investigation of reflected laser light, X-ray generation, electron and ion acceleration in the experiment demonstrate an enhanced performance of the robust microstructured silicon needle structure facing the incident laser pulse. A significant increase in high energetic electrons, ions and brilliant X-ray radiation is observed in comparison to flat foils and targets with geometric structures. Reflection losses from the interaction area are decreased substantially.
With the results of the experimental campaign a combination of the microstructured silicon surfaces with different materials is motivated. E.g. proton-rich materials can generate a reliable and auspicious source of laser-accelerated protons. Joining the structured target with a confined piece of material, point-like sources of brilliant X-ray radiation of selectable photon energy become available. Employing the fabrication setup developed within the framework of this thesis a valuable addition to the scope of the *Detektor & Targetlabor* is given. The further development of the setup towards high-repetition rate laser facilities, production of customisable and more complex targets and evaluation of applications for highly light absorbing surfaces is promising.

Contents

Role of the author

Theses supervised within this work in the *Detektor- & Targetlabor*:

- RENÉ LEONHARDT: Konstruktion und Charakterisierung eines Galvanometer Systems zur zweidimensionalen Strahlablenkung, **Miniforschung** (2015)
- RENÉ LEONHARDT: Aufbau und Charakterisierung eines zweidimensionalen Galvanometersystem, **Bachelor Thesis** (2016)
- TINA EBERT: Homogene Oberflächenstrukturierung von Silizium durch ultrakurze Laserpulse, **Master Proposal** (2016)
- TINA EBERT: Homogeneous Surface Structuring of Silicon with Ultrashort Laser Pulses, **Master Thesis** (2017)
- LAURA D. GEULIG: Diffraktive optische Strahlformung zur homogenen Strukturierung von Oberflächen mittels ultrakurzer Laserpulse, **Bachelor Thesis** (2018)

Publications with the author involved:

- **N. W. NEUMANN**, L. N. K. DÖHL, J. JARRETT, C. BAIRD, T. EBERT, R. HEATHCOTE, M. HESSE, A. HUGHES, P. MCKENNA, D. NEELY, D. RUSBY, G. SCHAUMANN, C. SPINDLOE, A. TEBARTZ, N. WOOLSEY and M. ROTH, A bright laser-driven X-ray and particle source using microstructured silicon targets. *Nature Physics*, under submission (2018).
- **N. W. NEUMANN**, T. EBERT, G. SCHAUMANN and M. ROTH. A setup for micro-structured silicon targets by femtosecond laser irradiation, *Journal of Physics: Conference Series*, accepted for publication (2018).
- T. EBERT, **N. W. NEUMANN**, T. ABEL, G. SCHAUMANN and M. ROTH. Laser-induced microstructures on silicon for laser-driven acceleration experiments, *High Power Laser Science and Engineering* **5**, 13 (2016).
- W. CAYZAC, A. FRANK, A. ORTNER, V. BAGNOUD, M. M. BASKO, S. BEDACHT, C. BLÄSER, A. BLAZEVIC, S. BUSOLD, O. DEPPERT, J. DING, M. EHRET, P. FIALA, S. FRYDRYCH, D.O. GERICKE, L. HALLO, J. HELFRICH, D. JAHN, E. KJARTANSSON, A. KNETSCH, D. KRAUS, G. MALKA,

N. W. Neumann, K. Pépitone, D. Pepler, S. Sander, G. Schaumann, T. Schlegel, N. Schroeter, D. Schumacher, M. Seibert, A. Tauschwitz, J. Vorberger, F. Wagner, S. Weih, Y. Zobus and M. Roth. Experimental discrimination of ion stopping models near the Bragg peak in highly ionized matter, *Nature Communications* **8**, 15693 (2017).

- E. Oks, E. Dalimier, A. Y. Faenov, P. Angelo, S. A. Pikuz, T. A. Pikuz, I. Y. Skobelev, S. N. Ryazanzev, P. Durey, L. Doehl, D. Farley, C. Baird, K. L. Lancaster, C. D. Murphy, N. Booth, C. Spindloe, P. McKenna, **N. W. Neumann**, M. Roth, R. Kodama and N. Woolsey. In-depth study of intra-Stark spectroscopy in the x-ray range in relativistic laser–plasma interactions, *Journal of Physics B: Atomic, Molecular and Optical Physics* **50**, 245006 (2017).

- W. Cayzac, V. Bagnoud, A. Blazevic, S. Busold, O. Deppert, J. Ding, P. Fiala, S. Frydrych, D. Jahn, **N. W. Neumann**, A. Ortner, G. Schaumann, D. Schumacher, F. Wagner, S. Weih and M. Roth. Charge-state equilibration of a carbon beam at 0.65 MeV per nucleon energy in thin solid carbon foils, *GSI annual report 2016* (2017).

- A. Alejo, S. Kar, A. Tebartz, H. Ahmed, S. Astbury, D. C. Carroll, J. Ding, D. Doria, A. Higginson, P. McKenna, **N. W. Neumann**, G. G. Scott, F. Wagner, M. Roth and M. Borghesi. High resolution Thomson Parabola Spectrometer for full spectral capture of multi-species ion beams, *Review of Scientific Instruments* **87**, 083304 (2016).

Participation in **Conferences and further education**:

- **N. W. Neumann**. "Laser-induced microstructures on silicon for laser-driven acceleration experiments", talk, conference contribution to the *Christmas Meeting of the High Power Laser User Community*, Abingdon, UK, 18th-20th December 2017.

- **N. W. Neumann**. "Micro-structured Targets by Femtosecond Laser Irradiation for High Repetition Rate Laser Plasma Science", talk, conference contribution to the *Targ3 - 3rd Targetry for High Repetition Rate Laser-Driven Sources* workshop, Colegio Fonseca, Salamanca, Spain, 21st-23rd June 2017.

- Participation in the *Network on Extreme Intensity Laser System Meeting 2017 - NEILS 2017*, Centro de Laseres Pulsados (CLPU), Salamanca, Spain, 20th June 2017

- **N. W. Neumann**, T. Ebert, G. Schaumann and M. Roth. "A setup for micro-structured silicon targets by femtosecond laser irradiation", poster, conference contribution to the *6th Target Fabrication Workshop*, University of Greenwich, London, UK, 8th-11th May 2017

- Completion of *Target Area Operator Training* course, Central Laser Facility, Oxfordshire, UK, 4th-7th April 2017

Contribution to experimental campaigns:

- **N. W. Neumann**, Laser-driven acceleration by microstructured silicon targets, *Central Laser Facility*, Oxfordshire, UK, 10th January-26th February 2017.

- P. Durey, Extreme x-ray radiation fields created during an ultra-intense laser-solid interaction, *Central Laser Facility*, Oxfordshire, UK, 1st August-2nd September 2016.

- A. Tebartz, Laser-Driven Ion Acceleration with Freestanding Cryogenic Deuterium Targets, *PHELIX Laser Facility*, Darmstadt, Germany, 3rd-26th February 2016.

- A. Tebartz, Laser-Driven Ion Acceleration with Freestanding Cryogenic Deuterium Targets, *Central Laser Facility*, Oxfordshire, UK, 9th November-13th December 2015.

- W. Cayzac, Experimental discrimination of ion stopping models near the Bragg peak in highly ionized matter, *PHELIX Laser Facility*, Darmstadt, Germany, 2nd-16th September 2015.

- W. Cayzac, Experimental discrimination of ion stopping models near the Bragg peak in highly ionized matter, *PHELIX Laser Facility*, Darmstadt, Germany, 26th July-2nd August 2015.

Vita

Name	Nico Wilfrid Neumann
Date of birth	6th August 1988
Place of birth	Darmstadt
Nationality	German
Marital status	Married

Tertiary education

2015 - 2018	Technische Universität Darmstadt Doctoral studies Stipendiary at Darmstadt Graduate School of Excellence Energy Science and Engineering
2013 - 2014	Technische Universität Darmstadt Physics studies (Master of Science, M.Sc.) Thesis: Untersuchungen zur Adiabatischen Frequenzkonversion in den XUV Spektralbereich
2008 - 2013	Technische Universität Darmstadt Physics studies (Bachelor of Science, B.Sc.) Thesis: Aufbau eines kompakten, nichtlinearen optischen Mikroskops

School education

2008	Bertolt-Brecht-Schule Darmstadt Higher education entrance qualification

Community activities

since 2015	Makerspace Darmstadt e.V. Club management director
since 2013	Federal Agency for Technical Relief, Darmstadt Assistant squad leader, first rescue group

List of abbreviations and symbols

$1/e^2$-width	full width at $1/e^2$ intensity
A	area
$\mathscr{A}(t)$	amplitude envelope
a_B	Bohr radius
α	attenuation coefficient
B	magnetic field strength
β	ratio of particle speed and speed of light
BOA	breakout after burner
BPP	beam parameter product
c	speed of light
c_0	speed of light in vacuum
C	capacitance
CCD	charge coupled device
CMOS	complementary metal-oxide-semiconductor
CPA	chirped pulse amplification
CSA	collisionless shock acceleration
cw	continuous wave
d	distance
$\Delta\lambda$	bandwidth
$\Delta\omega$	spectral width
Δt	temporal length, typically pulse length
DPSS	diode pumped solid state
e	fundamental electron charge
$E(t)$	temporal electric field
E_0	electric field amplitude
$\mathscr{E}$	energy
ϵ_0	vacuum permittivity
ϵ_i	permittivity
f	focal length
ν	frequency
FEG	field emission gun
F_L	Lorentz force
F_c	centripetal force
$\mathscr{F}$	energy fluence
FWHM	full width at half maximum
G	gain

γ	Lorentz factor
h	height
$s(\nu)$	sensitivity function
$\hbar$	reduced Planck constant
i	imaginary unit
$I(t)$	temporal intensity
I_0	intensity amplitude
$\tilde{I}(\omega)$	spectral intensity
IP	image plate
k	wave vector
$k(\lambda)$	imaginary part of the refractive index
k_B	Boltzmann constant
L	resonator length
λ	wavelength
λ_{Debye}	Debye length
LIDT	laser-induced damage threshold
LIPSS	laser-induced periodic surface structure
m	mass
M	mirror
M^2	beam quality factor
m_e	electron mass
μ_i	permittivity
n	refractive index
N	total number
$\omega_0(t)$	carrier wave frequency
ω_p	plasma frequency
p	impulse
ϕ, φ, θ	angular position
Φ_0	absolute phase
$\Phi_a(t)$	time dependent phase
$\mathscr{P}$	power
PSL	photo stimulated luminescence
Q	absolute charge
q	charge
R	reflectivity
$R(z)$	wave front curvature
R^2	coefficient of determination
RES	scanning resolution

RCF	radiochromic film
ρ	density
RPA	radiation pressure acceleration
SEM	scanning electron microscope
SF_6	sulphur hexafluoride
SHG	second harmonic generation
SRIM	stopping and range of ions in matter
STFC	science and technology facility council
T	transmittivity
TEM_{00}	fundamental Gaussian mode
θ_i	angle of incidence
THG	third harmonic generation
Ti:sa	titanium:sapphire
TNSA	target normal sheath acceleration
TP	Thomson parabola
TRIM	transport of ions in matter
UK	United Kingdom
UV	ultraviolet radiation
v	velocity
VIS	visible radiation
$w(z)$	beam radius
w_0	beam waist radius
x, y, z	spatial coordinates
z_0	Rayleigh length

List of figures

List of tables

1 Introduction

The development and fabrication of functional materials and surfaces have attracted increasing attention in materials science and engineering. For instance, bio-inspired functional surfaces solve various specific problems like wettability,[1] friction,[2] wear,[3] antifouling,[4] reflectivity and absorption.[5,6] Consequently, numerous techniques and activities have been developed that rely on physical, chemical and mechanical methods to create functional surfaces.

Within the framework of this thesis surfaces with increased light absorption are created. Increasing light absorption of materials and consequently decreasing reflectivity, scattering and transmission is a substantial motivation for a number of applications. Particularly, increasing the efficiency of photovoltaic systems,[7] camera sensors[8] and photodiodes[9] are topics relevant to society. Generally speaking, functional surfaces can considerably increase the luminous efficiency of photochemical and -electrical devices and systems.

Within the field of laser and plasma physics, including the working group of Prof. Dr. MARKUS ROTH, increasing the absorption efficiency in laser-driven processes is of large interest.[10] The interaction of ultra-intense high power lasers with matter is a dynamically growing field of activities.[10–14] The need for powerful, compact and reliable high energy particle and radiation sources is an ongoing catalyst for new techniques and materials within this field.

1 J.-N. Wang et al. *Nat. Publ. Gr.* **10**, e470, 2018.
2 N. Li et al. *Sci. Rep.* **6**, 39388, 2016.
3 D. Berman et al. *Nat. Commun.* **9**, 1164, 2018.
4 L. Wang et al. *Nat. Nanotechnol.* **12**, 509–522, 2017.
5 M. Malinauskas et al. *Light Sci. Appl.* **5**, e16133, 2016.
6 C. Wu et al. *Appl. Phys. Lett.* **78**, 1850–1852, 2001.
7 S. Kontermann et al. *Energy Procedia* **27**, 390–395, 2012.
8 J. Lv et al. *Nanoscale Res. Lett.* **13**, 110, 2018.
9 Z. Huang et al. *Appl. Phys. Lett.* **89**, 033506, 2006.
10 M. Borghesi et al. *Fusion Sci. Technol.* **49**, 412–439, 2006.
11 S. C. Wilks and W. L. Kruer. *IEEE J. Quantum Electron.* **33**, 1954–1968, 1997.
12 G. A. Mourou, T. Tajima, and S. V. Bulanov. *Rev. Mod. Phys.* **78**, 309–371, 2006.
13 H. Daido, M. Nishiuchi, and A. S. Pirozhkov. *Reports Prog. Phys.* **75**, 056401, 2012.
14 A. Macchi, M. Borghesi, and M. Passoni. *Rev. Mod. Phys.* **85**, 751–793, 2013.

The development of improved custom tailored targets is necessary to cope with the range of scientific research and applications evolving.[15] Especially, the development of laser-induced sources of intense particle bunches and electromagnetic radiation benefits from an increased efficiency of the target.
A series of ground-breaking experiments have demonstrated the influence of microstructured targets to high power laser experiments from laser absorption and specular reflectivity[16] to heating of electrons,[17] acceleration of ions[18] and the generation of brilliant X-ray radiation.[19–22]
Over the last decades, lasers have evolved to become the driving force of cost-efficient and high quality material processing like drilling, cutting, welding and additive manufacturing.[5,23] With efficient and affordable sources of ultra-short laser beams with a pulse duration in the femtosecond-range ($1\,\mathrm{fs} = 10^{-15}\,\mathrm{s}$) various functional surfaces can be created based on the technique of *laser-induced periodic surface structures* (LIPSS). This universal phenomenon can be observed with all classes of materials when irradiated with short laser-pulses and pulse energies near the ablation threshold.[24]
In 1998 *Her et al.* demonstrated LIPSS fabricated on silicon under femtosecond irradiation in a gaseous sulphur hexafluoride (SF_6) atmosphere.[25] The resulting conical spikes on the surface increase the absorption of photons below and above the bandgap of silicon over a broad spectral range (visible and infrared).[26] The process involved is comparably easy and the structure scale of several micrometres perfectly suited for the application in a laser plasma experiment where nanoscale structures on the target would be destroyed long before the main laser pulse arrives.
Within this thesis, an extensive fabrication setup for microstructured silicon targets is developed, based on the work of *Her et al.* (part I). The influence of a functional structured target surface incident to the laser pulse is following

[15] I. Prencipe et al. *High Power Laser Sci. Eng.* **5**, e17, 2017.
[16] O. Klimo et al. *New J. Phys.* **13**, 053028, 2011.
[17] G. Cristoforetti et al. *Sci. Rep.* **7**, 1479, 2017.
[18] A. Lübcke et al. *Sci. Rep.* **7**, 44030, 2017.
[19] Z. Zhao et al. *Phys. Plasmas* **17**, 123108, 2010.
[20] L. C. Jarrott et al. *Phys. Plasmas* **21**, 031211, 2014.
[21] W. Yan et al. *Nat. Photonics* **11**, 514–520, 2017.
[22] F. Ráksi et al. *J. Chem. Phys.* **104**, 6066–6069, 1996.
[23] K. Sugioka and Y. Cheng. *Light Sci. Appl.* **3**, e149, 2014.
[24] J. Bonse et al. *Conf. Lasers Electro-Optics* **23**, 9000615, 2016.
[25] T. H. Her et al. *Appl. Phys. Lett.* **73**, 1673–1675, 1998.
[26] M. A. Sheehy et al. *Chem. Mater.* **17**, 3582–3586, 2005.

investigated in a high power laser-plasma experimental campaign at the *Vulcan* laser system of the *Central Laser Facility*, Oxfordshire, UK (part II). The results of this experiment demonstrate an increased performance of microstructured silicon surfaces in comparison to conventional target types.

This work is structured as follows:
Chapter 2 demonstrates fundamental processes and techniques involved in this work. A basic mathematical description of pulsed laser light and Gaussian beam optics is presented, followed by the description of the working principle of ultrafast laser sources and the technique of *chirped pulse amplification* (CPA). The interaction of matter and laser pulses with different intensities over several orders of magnitudes is described, motivating the generation of LIPSS and laser-driven particle acceleration from intense plasma conditions. Concluding, fundamental work within the field of laser-plasma experiments as well as laser-induced fabrication of microstructures is identified and illustrated.
Chapter 3 shows the experimental implementation of the fabrication setup for customised microstructured surfaces. Required parameters and components are presented, prior to the adaption of the laser system. Two fabrication setups have been developed within this work for a) single exposure and b) continuous scanning of surfaces. The processing chamber for different ambient media and parameter ranges is presented. Closing, techniques of characterising highly light absorbing surfaces are given.
The influence of various processing and laser parameters to the fabrication of microstructures is illustrated in chapter 4. For the processing of silicon in sulphur hexafluoride the prediction of needle height and separation of the resulting structure is presented.
Chapter 5 summarises the planning and preparation phase of the experimental campaign. A diagnostic setup for a complete as possible picture of the influence of a structured surface to the reflection and absorption of laser light, generation of X-ray radiation and acceleration of electrons and ions is shown. The production of four different target types and optimisation of the laser system and temporal contrast is included.
Chapter 6 illustrates the working principle of the main diagnostic equipment used in the experiment and the acquisition of data. Thereby, the diagnostic channels are categorised into four groups: light, X-ray radiation, electrons and ions. The spatial and spectral distribution of these categories is considered.
Chapter 7 derives the results of the experimental campaign. A comprehensive picture of the interaction of structured surfaces in comparison to flat foils is

shown. The structured functional surface, fabricated and characterised within the framework of this thesis, shows a substantial increase in efficiency to the acceleration of ions, generation of energetic electrons and X-ray radiation.
A summary of this work is disclosed in the final chapter 8. Concluding, an outlook and motivation for future work is given.

Part I.

Generation of laser-induced microstructures on silicon

2 Fundamentals

The core of this work is the interaction of intense laser pulses with matter. The following chapter gives a brief summary of processes and techniques contained in this thesis.
First, an overview of the underpinning physics is given. This involves the foundations for the theoretical description of pulsed laser light (section 2.1) and the generation and amplification of these intense and ultra-short pulses of energy (section 2.2).
Following, an outline of the interaction physics of light and matter is given (section 2.3). Thereby, several orders of magnitude in intensity of the driving light fields are considered, from the excitation of atoms and precisely controlled ablation of matter to the generation of plasma and laser-driven acceleration of particles.
Concluding, scientific work within the field is described that led to the motivation for this thesis (section 2.4).

2.1 Theory of pulsed laser light

The key techniques employed through part I and part II of this work are all based on the unique behaviour of ultra-short laser pulses. For this purpose it is elementary to show methods for the mathematical description of electric field and intensity for such short pulses of light and their propagation in space. The latter is based on Gaussian beam optics as a paraxial approximation. Furthermore, the generation of femtosecond laser pulses using the titanium:sapphire laser and the intensification through chirped pulse amplification is explained.

2.1.1 Mathematical description

For the mathematical description of laser radiation, the linear polarised electric field at the position of a fixed detector can be written as function $E(t)$. The real part of the time dependent electric field, neglecting the spatial distribution

at this point, can be written as the product of a carrier wave and amplitude envelope $\mathscr{A}(t)$[27]

$$E(t) = \mathscr{A}(t) \cdot \cos[\omega_0 t + \Phi_0 + \Phi_a(t)]. \tag{2.1}$$

With carrier frequency ω_0, absolute phase Φ_0 and time dependent phase $\Phi_a(t)$. The carrier frequency for an optical pulse centred at $\lambda = 800\,\text{nm}$ (as used within this work) equals $\omega_0 = {}^{2\pi c_0}/_{\lambda} \approx 2.35\,{}^{\text{rad}}/_{\text{fs}}$, taking the speed of light c_0 in vacuum into account. The period of the carrier wave is therefore approximately 2.67 fs. The absolute phase Φ_0, describing the phase relation between carrier wave and envelope function $\mathscr{A}(t)$, is of particular influence for very few cycles. The time dependent phase $\Phi_a(t)$ summarises the temporal change of the carrier frequency. For the overall phase $\Phi(t) = \omega_0 t + \Phi_0 + \Phi_a(t)$, the instantaneous light frequency $\omega(t)$ is[27]

$$\omega(t) = \frac{\mathrm{d}\Phi(t)}{\mathrm{d}t} = \omega_0 + \frac{\mathrm{d}\Phi_a(t)}{\mathrm{d}t}. \tag{2.2}$$

The term ${}^{\mathrm{d}\Phi_a(t)}/_{\mathrm{d}t}$ describes variations of the laser frequency in time and is called chirp. These variations are typically introduced by the laser system and all optical components (dispersive elements) either deliberately, unrecognised or unfeasible.
The oscillating intensity $I_{\text{osc}}(t)$ and the mean temporal intensity $I(t)$ of a laser pulse can be described as[28]

$$I_{\text{osc}}(t) = \frac{1}{2}\epsilon_0 c n E(t)^2 \qquad I(t) = \frac{1}{2}\epsilon_0 c n_i \mathscr{A}(t)^2, \tag{2.3}$$

with speed of light c, vacuum permittivity ϵ_0 and refractive index n_i.
Figure 2.1 shows the electric field $E(t)$ and intensity $I(t)$ for a Gaussian temporal envelope[28]

$$\mathscr{A}(t) = \frac{E_0}{2} \cdot \exp\left[-2\ln(2) \cdot \left(\frac{t}{\Delta t}\right)^2\right]. \tag{2.4}$$

[27] M. Wollenhaupt, A. Assion, and T. Baumert. Springer Handbook of Lasers and Optics. 2012. 1047–1094 DOI: 10.1007/978-3-642-19409-2_12.

[28] J. C. Diels and W. Rudolph. Ultrashort Laser Pulse Phenomena. Elsevier, 2006. DOI: 10.1016/B978-012215493-5/50021-5.

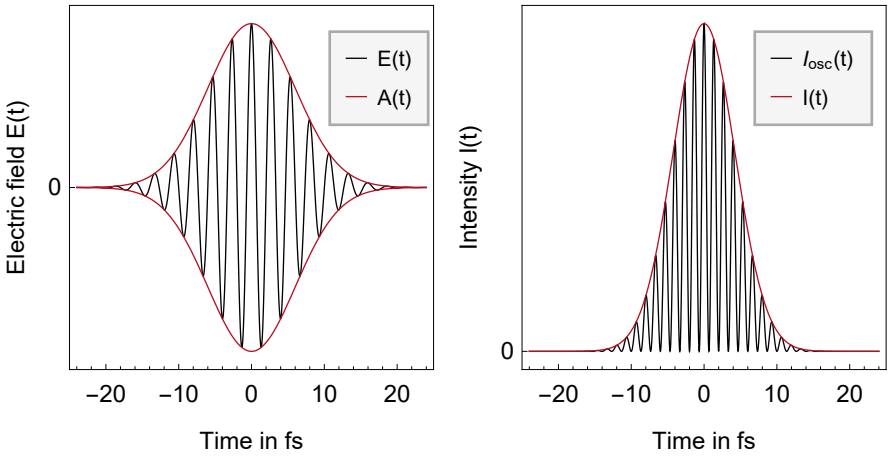

Figure 2.1.: The oscillating electric field $E(t)$ (left, black) and intensity $I_{\mathrm{osc}}(t)$ (right, black) for a laser pulse with a Gaussian temporal envelope $\mathscr{A}(t)$ (red) with a length of $\Delta t = 10\,\mathrm{fs}$. The intensity envelope $I(t)$ (red) is thereby also Gaussian distributed. For illustration, no absolute phase and chirp is applied.

Here, no absolute phase and chirp is applied. For a Gaussian amplitude envelope $\mathscr{A}(t)$ the length Δt is typically given as full width at half maximum (FWHM). Here an exemplary pulse length of $\Delta t = 10\,\mathrm{fs}$ is illustrated. Using equation 2.2 and 2.3, the depicted time response is found. The oscillating intensity does not coincide with the mean temporal intensity if nonlinear effects have to be taken into account.
The spectral intensity $\tilde{I}(\omega)$ of the laser pulse can be obtained by the Fourier inversion theorem.[27] Thereby, the spectral width $\Delta\omega$ and the pulse length Δt are connected by the time-bandwidth product[28]

$$\Delta\omega \cdot \Delta t \geq \frac{2\ln(2)}{\pi} \approx 0.441. \tag{2.5}$$

The shortest temporal lengths are achieved for laser pulses without chirp. This case is called a bandwidth-limited laser pulse. An important consequence from equation 2.5 is that the shorter the pulse length Δt, the larger the spectral width $\Delta\omega$. The spectral bandwidth is limited by the gain medium. For a central wavelength of 800 nm the minimum pulse length is given

by $\Delta\lambda \cdot \Delta t = 940\,\text{nm} \cdot \text{fs}$.[28] A 10 fs bandwidth limited pulse centred at 800 nm, for example, has a minimum spectral width of about $\Delta\lambda = 100\,\text{nm}$[27] and thereby notable requirements for the laser gain medium. This is described in section 2.2 in more detail with focus on the unique properties of the titanium:sapphire laser.

2.1.2 Gaussian beam optics

For most cases throughout this thesis, Gaussian beam optics is considered as a powerful formalism to describe and obtain the characteristics of laser beams in the setup. Gaussian beams are a solution of the scalar Helmholtz equation for coherent laser beams close to the optical axis (paraxial approximation[29]). The Helmholtz equation represents a time-independent form to describe electromagnetic waves based on Maxwell's equations.[27]
In this section the propagation of coherent laser beams and their transformation by optical components is described. Here, a Gaussian spatial distribution of the electric field amplitude is considered, in addition to the temporal Gaussian envelope $A(t)$ described in the previous section. For a radial symmetric transverse electromagnetic TEM_{00} mode in polar coordinates (r,z) the electric field can be written as[28]

$$E(r,z,t) = A(t) \cdot \tfrac{w_0}{w(z)} \cdot \exp\left[-\left(\tfrac{r}{w(z)}\right)^2\right] \cdot \exp\left[-ik\tfrac{r^2}{2R(z)}\right] \cdot \exp[i(\zeta(t)+kz)]. \quad (2.6)$$

With wave number $k = {}^{2\pi}/_{\lambda}$, beam radius $w(z)$ at position z and the minimal beam radius w_0 at $z = 0$. The Gouy phase $\zeta(t)$ describes the phase shift of the fundamental mode, when passing the beam waist from $z \ll 0$ to $z \gg 0$. Higher mode patterns are described by a combination of Laguerre polynomials and a Gaussian beam profile with TEM_{nm}. Here, only the fundamental mode TEM_{00} is considered. The radial intensity of a Gaussian beam is also a Gaussian distribution[27]

$$I(r,z) = I_0 \cdot \left(\frac{w_0}{w(z)}\right)^2 \cdot \exp\left[-2 \cdot \left(\frac{r}{w(z)}\right)^2\right]. \quad (2.7)$$

[29] M. Lax, W. H. Louisell, and W. B. McKnight. *Phys. Rev. A* **11**, 1365–1370, 1975.

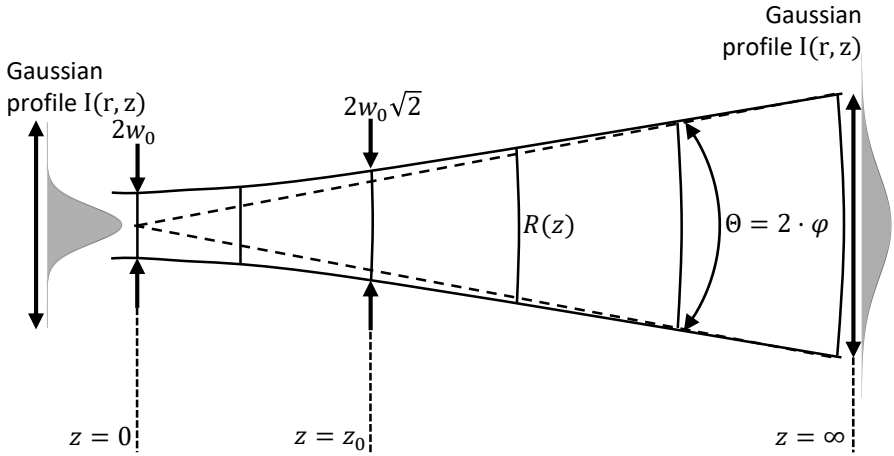

Figure 2.2.: The propagation of an ideal Gaussian beam is characterised by the beam waist radius w_0 at $z = 0$ and the Rayleigh length z_0 where the beam radius has increased by a factor of $\sqrt{2}$ and the cross section has doubled, respectively. The wave front curvature is labelled with $R(z)$. For $z = 0$ and $z = \infty$ planar wavefronts are observed, as $R = \infty$. Furthermore, in far field a full (half) opening angle θ (ϕ) is defined.

The beam radius is defined as the radial position, where the intensity has dropped to $1/e^2$.
The z dependent beam radius $w(z)$ and wave front curvature $R(z)$ are[27]

$$w(z) = w_0 \cdot \sqrt{1 + (z/z_0)^2}, \qquad R(z) = z \cdot \left(1 + (z_0/z)^2\right). \tag{2.8}$$

Figure 2.2 illustrates the properties of such a Gaussian beam. The Rayleigh length $z_0 = \pi w_0^2/\lambda$ equals the distance from $z = 0$ to where the beam radius has increased by a factor of $\sqrt{2}$ and the cross section has doubled. At this position $\pm z_0$, the wave front curvature is maximised. Furthermore, the half opening angle φ of the beam in far field is defined as $\tan(\varphi) = \lambda/\pi w_0$. Thus, the full divergence angle of a laser beam in far field is $\theta = 2 \cdot \phi$.
The physical quantity that describes the quality of a Gaussian beam is the beam parameter product[27]

$$\mathrm{BPP} = \varphi \cdot w_0 = M^2 \cdot \frac{\lambda}{\pi} \tag{2.9}$$

and characterises how well a beam can be focussed to a small spot. It is specified by wavelength λ and the beam quality factor M^2.
For an ideal single mode TEM_{00} Gaussian laser beam M^2 is exactly one. The method of measurement of the beam quality factor is regulated as ISO standard 11146:2-2005(en):[30]
Introducing an ideal and thin lens with focal length f to the beam path, the minimum focal radius is $w_f = {}^{BPP}/_{\theta}$ with $\tan(\theta) = {}^{w_L}/_{f}$ and beam radius w_L at the lens position.[27] For small divergence angles ($\tan(\theta) \approx \theta$) this simplifies to:

$$w_f \approx M^2 \cdot \frac{\lambda \cdot f}{\pi \cdot w_L}. \tag{2.10}$$

As a result, the focal width is smaller if a short focal length f and large entrance beam radius w_L is chosen. The achievable focal width is limited by the beam quality. In the experiment, with a fixed M^2 value of the laser system, the focus area can be precisely set by the combination of lens and entrance beam.

2.1.3 Energy measurands

In the laboratory laser, radiation can typically not be characterised by the electric field strength $E(t)$. Concrete and obtainable measurement values are the intensity I, energy fluence $\mathscr{F}$, power P or energy $\mathscr{E}$. Following, the spatial profile of the electric field has to be considered. For a rotationally symmetric beam profile (like TEM_{00}), the spatial and temporal intensity distribution $I(r,t)$ is obtained by integration of the electric field $E(r,t)$ over a full oscillation period T[28]

$$I(r,t) = \epsilon_0 c n \frac{1}{T} \int_{t-T/2}^{t+T/2} E\left(r,t'\right)^2 \mathrm{d}t' = \frac{1}{2}\epsilon_0 c n \mathscr{A}(r,t)^2 . \tag{2.11}$$

Typically, the intensity is given in units of ${}^{W}/_{cm^2}$.

[30] *Lasers and laser-related equipment — Test methods for laser beam widths, divergence angles and beam propagation ratios — Part 2: General astigmatic beams.* Standard Geneva, CH: International Organization for Standardization., 2005.

The momentary laser power $\mathscr{P}(t)$ is received by integrating the intensity over the full beam area A[27]

$$\mathscr{P}(t) = \int_A I(r,t)\,\mathrm{d}A \tag{2.12}$$

with unit W. In contrast, the fluence $\mathscr{F}$ or energy density is a measurand for the energy flow through the laser beam profile. It is given by the temporal integral over the full laser pulse intensity[28]

$$\mathscr{F}(r) = \int_{-\infty}^{\infty} I(r,t)\,\mathrm{d}t. \tag{2.13}$$

Here, it is given in $\mathrm{kJ/m^2}$ to conform with literature.[25] In this work, fluence $\mathscr{F}$ is the main measure for the laser-driven microstructuring process. The energy content $\mathscr{E}$ of a single laser pulse is obtained by the complete spatial and temporal envelope[28]

$$\mathscr{E} = \int_{-\infty}^{\infty}\int_A I(r,t)\,\mathrm{d}A\,\mathrm{d}t. \tag{2.14}$$

The physical unit of $\mathscr{E}$ is J. In the laboratory, energy content of highly intense laser radiation is typically measured with a calorimetric power meter. In our case, the average power $\bar{P}$ is measured over a period $\bar{T}$ that is several orders of magnitude longer than the pulse length. For a laser system with pulse repetition frequency $f_{\mathrm{rep}} = 1/T'$ the average power

$$\bar{\mathscr{P}} = \frac{1}{T'}\int_{-T'/2}^{T'/2} \mathscr{P}(t)\,\mathrm{d}t = \mathscr{E}\cdot f_{\mathrm{rep}} \tag{2.15}$$

is measured. Using the example of the laser system in this thesis (see section 3.2.1), a maximum average power of $\bar{\mathscr{P}} = 1\,\mathrm{W}$ is measured. With a repetition frequency of $f_{\mathrm{rep}} = 5000\,1/s = 5\,\mathrm{kHz}$ the resulting energy per pulse is $\mathscr{E} = 2\cdot 10^{-4}\,\mathrm{J} = 200\,\mu\mathrm{J}$. The energy fluence $\mathscr{F}$ and intensity $I(r,t)$ depend strongly on the beam profile and temporal envelope for a given pulse energy. A spatial and temporal Gaussian beam with a width of 50 µm ($1/e^2$) has a peak

fluence of $\mathscr{F}(r = 0\,\mu\text{m}) = 3.75\,^{J}/_{\text{cm}^2}$. With a pulse length $\Delta t = 100\,\text{fs}$ (FWHM) centred around $t = 0\,\text{fs}$ the resulting peak intensity is[28]

$$I(r = 0\,\mu\text{m}, t = 0\,\text{fs}) = 5 \cdot 10^{13}\,^{W}/_{\text{cm}^2} = 50\,^{\text{TW}}/_{\text{cm}^2}. \tag{2.16}$$

This intensity corresponds to extreme electric field strengths of up to $4 \cdot 10^{6}\,^{\text{V}}/_{\text{m}}$.

2.2 Generation of ultra-short laser pulses

There is no standard definition for the duration of an ultra-short laser pulse. Typically, a pulse length is denoted ultra-short, if it is shorter than the major solid relaxation processes.[31,32]

Within only a few decades after the demonstration of the first working laser by *Maiman*,[33] the shortest duration of laser pulses was compressed from nanoseconds ($1\,\text{ns} = 10^{-9}\,\text{s}$) to the length of femtoseconds ($1\,\text{fs} = 10^{-15}\,\text{s}$).[34–36] In the last decades the attosecond regime ($1\,\text{as} = 10^{-18}\,\text{s}$) became available.[37]

For illustration a light pulse of 1 s spans approximately the distance between moon and earth, considering the speed of light in vacuum. Whereas a 10 fs pulse is equivalent to a 3 µm thin slice of light.[27] In comparison, the fastest molecular vibrations in nature oscillate with a 10 fs period. Thereby, fundamental processes in nature can be observed employing ultra-short laser pulses.[38] At the time of this thesis, femtosecond laser pulses can be generated directly from compact and reliable oscillators (and amplifiers).[27]

Femtosecond laser pulses can be generated with a variety of lasers with wavelengths ranging from the ultraviolet to the infrared. The most common laser source for 20 years is the titanium:sapphire laser[39], which is also employed in this thesis.

[31] E. G. Gamaly and A. V. Rode. *Prog. Quantum Electron.* **37**, 215–323, 2013.
[32] Tina Ebert. Homogeneous Surface Structuring of Silicon with Ultrashort Laser Pulses. Master Thesis. Technische Universität Darmstadt, 2017.
[33] T. H. Maiman. *Nature* **187**, 493–494, 1960.
[34] D. E. Spence, P. N. Kean, and W. Sibbett. *Opt. Lett.* **16**, 42, 1991.
[35] F Salin, J Squier, and M Piché. *Opt. Lett.* **16**, 1674–1676, 1991.
[36] M. L. M. Balistreri. *Science (80-.).* **294**, 1080–1082, 2001.
[37] P. Corkum and R. L. Davis. *Nature* **403**, 845–846, 2000.
[38] S. K. Sundaram and E. Mazur. *Nat. Mater.* **1**, 217–224, 2002.
[39] H. Frowein. *Opt. Photonik* **1**, 48–53, 2007.

The following section illustrates the working principle of this source. Afterwards, the fundamental technique of amplification to high intensities using chirped laser pulses is explained.

2.2.1 The titanium:sapphire laser

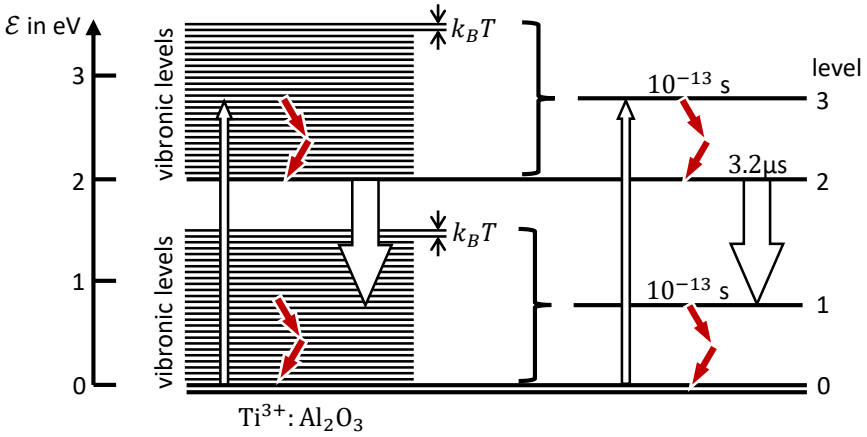

Figure 2.3.: A titanium:sapphire crystal as gain medium for a laser oscillator offers a broad bandwidth due to a high number of vibronic levels above ground state ($\mathcal{E} = 0\,\mathrm{eV}$) and the lowest excited state ($\mathcal{E} \approx 2\,\mathrm{eV}$). The system can be described as a simplified four-level scheme as indicated on the right. Level 1 and 3 have a short relaxation time in comparison to the laser level (2). As an optical pump typically lasers around $530\,\mathrm{nm}$ are used. The level scheme is an adapted version from ref. [40].

The first titanium:sapphire laser (Ti:sa) in continuous wave operation (cw) was demonstrated in 1986 by *P. F. Moulton*.[41] The term titanium:sapphire refers to the gain medium Ti^{3+}:Al_2O_3 of the laser. A sapphire crystal (Al_2O_3) is doped with Ti^{3+} ions at a concentration of typically 0.03% by weight.[40]

[41] P. F. Moulton. *J. Opt. Soc. Am. B* **3**, 125, 1986.

[40] K. F. Renk. Basics of Laser Physics: For Students of Science and Engineering. 2nd ed. Graduate Texts in Physics, Springer, 2012.

Due to titanium ions, the emission band of Ti:sa is shifted towards low energies (750 nm) and shows a broad spectral width as large as 200 nm.[42] Due to a high thermal conductivity (as high as metals) at low temperatures, high optical powers are achievable in this material.

Figure 2.3 shows the energy level scheme of a titanium:sapphire crystal, adapted version from ref. [40]. Key to the broad bandwidth of the gain medium are vibronic levels above the ground state ($\mathscr{E} = 0$) and above the lowest excited state ($\mathscr{E} \approx 2\,\mathrm{eV}$). Due to the long lifetime of the lowest excited state in comparison to the fast relaxation of the other states, the system can be described as a four-level system.[40] Figure 2.3 illustrates the simplified level diagram with a broad pump level (3), a sharp upper laser level (2), a broad lower laser level (1) and a sharp ground state level.[40] This system offers a broad absorption maximum for the optical pump of $490 - 600\,\mathrm{nm}$ and at the same time an enormous gain bandwidth between $670 - 1070\,\mathrm{nm}$.[39] Typically, frequency-doubled neodymium doped solid state lasers in the green spectrum are used for the excitation of the system.

The laser frequency ω in cw operation is mainly determined by the resonance length of the laser resonator. For a stable lasing process, the resonator length L needs to be a multiple of the half wavelength λ. Because of the broad gain bandwidth of the titanium:sapphire crystal a number of longitudinal modes with different wavelengths can build up in the oscillator. The circulating intensity inside the resonator is the sum of all single modes. If the longitudinal modes inside the resonator have a fixed phase relationship the resulting interference pattern is an intense train of light pulses.[39]

Figure 2.4 shows a number of single longitudinal modes (blue) and the resulting time-dependent intensity inside the resonator. Without constant phase relation, the laser operates in continuous wave mode (P_{cw}, black dashed line in figure 2.4). With a fixed relation, in contrast, a single and intense laser pulse is generated inside the resonator. The temporal distance of these pulses is thereby equal to $2L/c$, with resonator length L and speed of light c. Outside of the pulse, the intensity sum is close to zero. The higher the number of longitudinal modes, the sharper the intensity maximum and the shorter the pulse length Δt. Laser pulses generated by a number of 5 modes (red) and 50 modes (black) are shown in figure 2.4. The number of modes applied is inverse proportional to the bandwidth $\Delta\omega$ of the laser.

[42] C. Rullière. Femtosecond Laser Pulses: Principles and Experiments. 2nd ed. Springer, 2005.

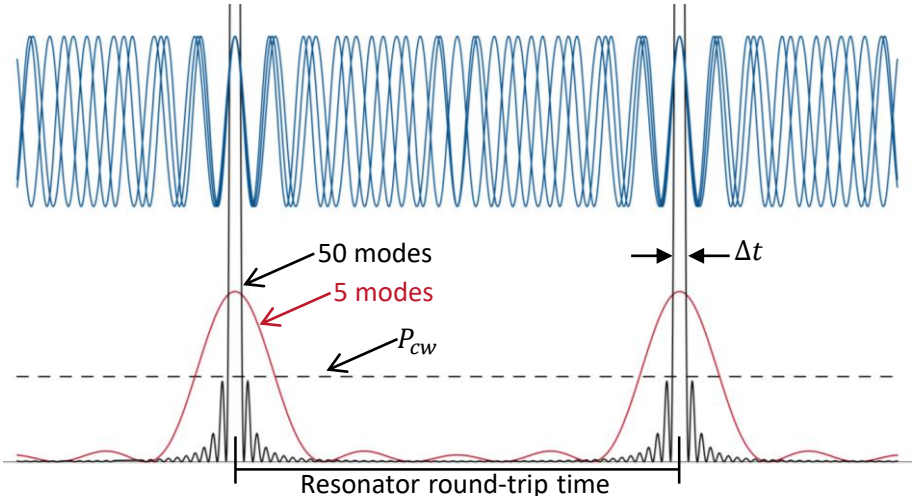

Figure 2.4.: Using the technique called mode-locking short pulses are created inside a resonator. In contrast to a continuous wave (cw) output (dashed line), the fixed phase relation and matching of longitudinal modes (blue) generates high intense ultra-short pulses with temporal length Δt. Laser pulses are illustrated here for a number of 5 (red) and 50 (black) longitudinal modes for a fixed resonator round-trip time. For a stable output in addition, cw operation of the resonator needs to be suppressed. On the basis of ref. [40].

Key to the reliable generation of femtosecond laser pulses is therefore (a) a fixed phase relation and (b) a suppression of P_{cw}. This is achieved by a technique called mode-locking.[27,39,42] In this thesis, passive Kerr-lens mode-locking is employed, based on the nonlinear optical Kerr effect. Titanium:sapphire lasers based on this technique lead to proven commercial systems with shorter pulse lengths compared to other mode-locking techniques.[27,42]

Due to the intensity dependent nonlinear properties of the laser crystal, pulsed wave fronts are focussed. Thereby, the beam diameter of pulsed radiation is narrower in comparison to cw radiation. Introducing an aperture in the resonator, that lets the high intensities pass while cw modes are blocked, the lasing process starts preferentially in pulsed operation. A problem with the number of different longitudinal modes in the resonator is pulse broadening due to dispersive elements.

Thence, a prism or grating pair is typically added to the resonator in order to compensate for dispersive broadening.
In summary, generation of femtosecond laser pulses is possible using the outstanding properties of the titanium:sapphire gain medium. The necessary key elements are a green optical pump source, adjustable resonator length, mode-locking using the optical Kerr effect and dispersion compensation. The pulsed radiation leaves the resonator through a partially reflective mirror. The laser system employed in this work is described in more detail in section 3.2.1. Following, the further intensification of high intense laser pulses using chirped pulse amplification (CPA) is demonstrated.

2.2.2 Chirped pulse amplification

The amplification of femtosecond laser pulses is limited by the damage threshold of the gain medium. State-of-the-art technology is the amplification using a technique called chirped pulse amplification demonstrated by *D. Strickland and G. Mourou* in 1985.[43] Thereby, a femtosecond laser pulse (e.g. generated by a mode-locked Ti:sa oscillator as described in 2.2.1) is temporally stretched to several hundred picoseconds or few nanoseconds. Afterwards the energy of the pulse is increased in consecutive amplifier stages (e.g. an optical pumped Ti:sa crystal) while the peak intensity of the pulse remains below the damage threshold of the system. After intensification, the laser pulse is recompressed to the femtosecond regime. Stretching and compression of laser pulses is typically achieved with a combination of optical gratings.[44]

2.3 Laser-matter interaction

The generation and amplification of laser light with pulse lengths on the scale of femtoseconds enables high peak intensities for the interaction with materials. The enormous number of resulting effects and mechanisms evolved is beyond the scope of this thesis.
Here, a brief overview for ultra-short laser pulses interacting with silicon is given. Considering only linear optical phenomena the propagation of light in materials is given in section 2.3.1. Following, dominant energy absorption

[43] D. Strickland and G. Mourou. *Opt. Commun.* **55**, 447–449, 1985.
[44] A. Vaupel et al. *Opt. Eng.* **53**, 051507, 2013.

mechanisms for electromagnetic radiation and their time scales in comparison to the laser pulse length are presented in section 2.3.2. Section 2.3.3 illustrates the formation and interaction of plasma with ultra intense laser light. This leads to the generation of highly ionised matter and acceleration of particles which is described in section 2.3.4 as an outlook to the high power experiment in part II of this thesis.

2.3.1 Propagation in materials

In this section the principles that describe the propagation and absorption of laser energy are demonstrated.
In the simplest case, the optical properties of a material only depend on the index of refraction n_i. This refractive index is a dimensionless number and connected to the electric and magnetic properties of the material over[45]

$$n_i = \sqrt{\epsilon_i \mu_i} = \frac{c_0}{c_i} \tag{2.17}$$

with permittivity ϵ_i and permeability μ_i. It is equivalent to the ratio of speed of light in vacuum and the reduced propagation velocity inside the material.
Consider the scenario of an electromagnetic wave reaching the surface of a material with different optical properties. A portion of the incident light will be reflected from the interface, as the refractive indices n_1, n_2 are different. The fraction of power that is reflected depends on these refractive indices and the angle of incident θ_i as well as the polarisation. The latter are separated for a linear polarised electromagnetic wave into polarisation components perpendicular (s-like) and parallel (p-like) to the reflecting surface. Derived from Fresnel's equations the relative reflection coefficients R_s and R_p write[45]

$$R_s = \left(\frac{E_r}{E_i}\right)^2 = \left(\frac{n_1 \cos(\theta_i) - n_2 \cos(\theta_t)}{n_1 \cos(\theta_i) + n_2 \cos(\theta_t)}\right)^2, \tag{2.18}$$

$$R_p = \left(\frac{E_r}{E_i}\right)^2 = \left(\frac{n_1 \cos(\theta_t) - n_2 \cos(\theta_i)}{n_1 \cos(\theta_t) + n_2 \cos(\theta_i)}\right)^2. \tag{2.19}$$

[45] Eugene Hecht. Optik. 6., De Gruyter, 2014.

Thereby, E_r and E_i denote the reflected and incident electric field amplitude. The transmission angle is θ_t. The coefficients of transmission T_s and T_p follow through $T_s = 1 - R_s$ and $T_p = 1 - R_p$, respectively.
Thence, the reflectivity of a given material depends on the refractive index, which is a function of the central wavelength λ. In addition, the reflectivity is subject to the material temperature through changes in the band structure, permittivity, permeability and plasma oscillations.
Transmitted light decays in intensity determined by a material attenuation coefficient α. A constant coefficient leads to an exponential decay in intensity with depth according to the Beer-Lambert law[45]

$$I(z) = I_0 \exp[-\alpha z]\,. \tag{2.20}$$

The absorption properties of a material can be included by defining a complex valued refractive index $\bar{n}_m = n_m + i\tilde{n}_m$ with $\alpha = 2\tilde{n}\omega/c$. Exemplary, the left side of figure 2.5 shows the complex refractive index of Silicon at 300 K, as derived from the work of *M. Green*.[46] The associated attenuation coefficient α is depicted on the right side.
Figure 2.5 illustrates that the complex index of refraction is obviously a wavelength dependent quantity. The equations and properties described so far consider only linear optical effects. This it not the case for all materials and laser parameters. Especially ultra-short laser pulses in the picosecond and femtosecond regime enable additional phenomena due to the high intensities. Typical absorption mechanisms on this time scale are discussed in the following section.

2.3.2 Absorption mechanisms and time scales

A laser pulse with a length of several femtoseconds delivers energy to matter on ultra-short time scales that are comparable to the natural oscillation periods of atoms and molecules. During the interaction with a light pulse the movement of atoms is insignificant and the atomic structure stays intact.[38]
Consider the interaction of a 100 fs laser pulse with an intensity below $10^{16}\,\mathrm{W/cm^2}$ and a crystalline silicon surface. Above this intensity threshold the movement of excited electrons has to be considered relativistic and the interaction changes dramatically .[31] Depending on the absorbed laser energy to

[46] M. A. Green. *Sol. Energy Mater. Sol. Cells* **92**, 1305–1310, 2008.

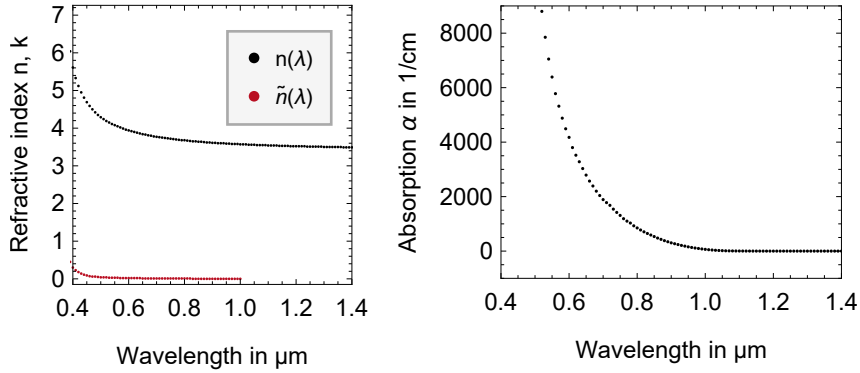

Figure 2.5.: Wavelength dependent real part $n(\lambda)$ and imaginary part $\tilde{n}(\lambda)$ of the refractive index of crystalline silicon (left). The attenuation coefficient α of silicon illustrates the band gap at $1.1\,\mu\mathrm{m}$ (right). In dependence on the data of ref. [46].

the crystal, weak excitation or structural phase transitions up to the removal of material from the crystal can occur. The crystalline structure can be contained or altered. A solid to liquid conversion or the creation of plasma with conditions of extreme pressure and temperature can be observed, embedded inside a solid and undisturbed silicon lattice.

At first, only electrons are excited by the electromagnetic wave. The crystal structure stays cold and a strong non-equilibrium is created almost instantly. Until the system reaches a balanced equilibrium again, several stages of relaxation from femtoseconds to microseconds are passed, depending strongly on the initial laser pulse parameters (and material properties). This path to equilibrium, with focus on silicon, is described in the work of *Sundaram and Mazur*.[38]

Figure 2.6 illustrates four major consecutive regimes of relaxation after the excitation through a femtosecond laser pulse. For photon energies above the band gap of silicon, the dominant absorption mechanism is single photon absorption. Additionally, impact ionisation can occur. Thereby, a high number of carriers (electrons and holes) are generated. For the first 10 fs to 100 fs during the laser pulse coherent oscillation effects can be observed. These oscillations dephase rapidly in time until the carriers can be considered free (carrier excitation).

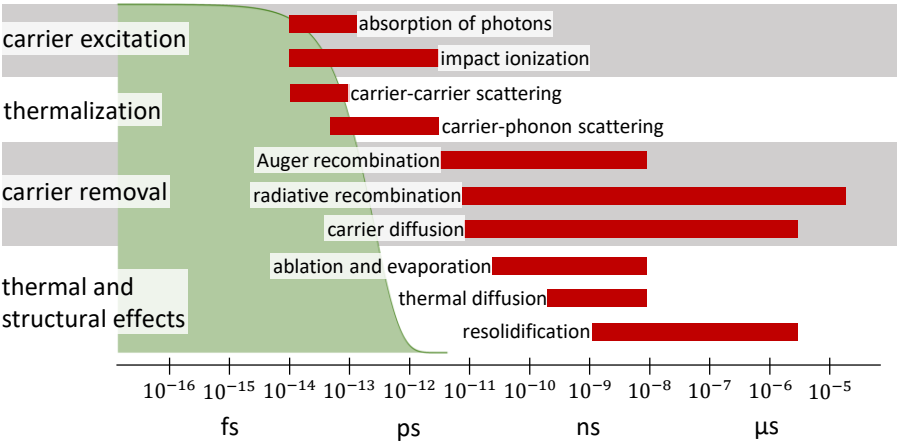

Figure 2.6.: A solid that is excited by a sub-ps laser pulse (green) undergoes four major regimes of relaxation. Consecutive, first carriers are excited through absorption and ionisation. At the same time thermalisation by scattering takes place. Following, carriers are eventually removed. Thus, thermal and structural effects can be observed. Please note, that the excitation time by such a short laser pulse is orders of magnitudes shorter than thermal effects. Thereby, atoms can be removed from a cold lattice before equilibrium conditions are reached. In dependence on ref. [38].

During and after excitation carriers are redistributed inside the band structure of the lattice by carrier-carrier and carrier-phonon scattering. For carrier-carrier scattering energy is not transferred to the lattice. With the emission of phonons, the carriers slowly incorporate energy to the crystal over many scattering processes per carrier and the timespan of several picoseconds. After that, the lattice and the carriers show an equilibrium temperature, even though an excess of free carriers is still existent (thermalisation).
The equilibrium temperature is typically reached within picoseconds. The removal of free carriers takes longer by orders of magnitude. They are removed by a combination of radiative processes (like luminescence) and non-radiative processes (like Auger recombination or carrier diffusion) and thereby redistributed also to regions outside the initial interaction volume (carrier removal). If the equilibrium temperature is above the melting or boiling point of silicon, liquidation or vaporisation occur. Thereby, the energy is converted to

kinetic energy and atoms can leave the bulk material. This process is called ablation. The equilibrium temperature of the crystal recovers to ambient conditions within microseconds. Concluding, reversible and irreversible changes are induced by the laser energy (thermal and structural effects).
For ultra-short pulses, the bond of ions to the lattice can be enervated without heating if a high number of valence electrons is excited. Thereby, atoms can be removed from a cold lattice before reaching equilibrium conditions. At high intensities, significant ionisation occurs and a plasma is generated, as described in the following section.

2.3.3 Plasma formation

Unlike the three traditional states of matter, an ideal plasma consists of free charged particles. Metaphorically speaking, the plasma state is a gaseous mixture of free electrons and partially positive to fully ionised atoms.[47,48]
The generation of free electrons inside a plasma requires an electrostatic force that is comparable to the binding energy of the electron to the nucleus. For a hydrogen atom this electric field strength E_{bind} is[47]

$$E_{\text{bind}} = \frac{e}{4\pi\epsilon_0 a_B^2} \approx 5 \cdot 10^9 \,\frac{\text{V}}{\text{m}}, \tag{2.21}$$

with Bohr radius $a_B = {}^{4\pi\epsilon_0\hbar^2}/_{m_e e^2} \approx 5 \cdot 10^{-11}\,\text{m}$, reduced Planck constant $\hbar$, electron mass m_e and charge e. Hence, to ionise a hydrogen atom using a laser a minimum intensity of

$$I = \tfrac{1}{2}\epsilon_0 c\,|E|^2 \approx 3.5 \cdot 10^{16}\,\frac{\text{W}}{\text{cm}^2} \tag{2.22}$$

is required. However, ionisation can also be observed at lower intensities generated by different processes.
An excited electron that is still part of the atomic configuration shows a certain relaxation time between receiving energy by the laser field and losing the energy by emission of a photon.

[47] A. Piel. Plasma Physics: An Introduction to Laboratory, Space, and Fusion Plasmas. 2nd ed. Springer, 2017.

[48] P. Mulser and D. Bauer. High Power Laser-Matter Interaction. 2nd ed. Springer, 2010. DOI: 10.1007/978-3-540-46065-.

If another photon is absorbed in this short timespan, the electron can gain additional energy. If the total energy exceeds the ionisation threshold E_{ionise}, the electron can escape. This process is called *multi-photon ionisation*. The electron can even gain excess kinetic energy by this process, which is referred to as *above-threshold ionisation*.
At higher intensities the electric potential of the atom can be modified by the electromagnetic laser field. The potential can be altered, such that the electron can tunnel through the potential barrier. This process is called *tunnel ionisation*. At higher field strength of the driving radiation, the barrier can be fully suppressed and allows the electron to freely escape. This is known as *barrier suppression ionisation*.
If a significant number of electrons is ionised, a plasma can be formed. In contrast to an ideal gas, the carriers inside a plasma do not move freely but interact by electric and magnetic forces. Thereby, the plasma shows collective behaviour as a response to external perturbations. In contrast to the interaction of two single charges where the strength of the Coulomb force scales with $1/r^2$, within a plasma additional damping and screening effects need to be considered. As a result, the interaction strength of a charge inside a plasma scales exponentially with[47]

$$\varphi(r) = \frac{Q}{4\pi\epsilon_0 r}\exp\left[-\frac{r}{\lambda_{\text{Debye}}}\right], \quad \text{with} \quad \lambda_{\text{Debye}} = \sqrt{\frac{\epsilon_0 k_B T_e}{n_e e^2}}. \tag{2.23}$$

The characteristic Debye shielding length λ_{Debye} is the depth at which the electric potential of a charge falls off by $1/e$. With sufficient distance, the plasma can be considered uncharged. Remarkably, the plasma is characterised by a mean temperature T_e for the electrons. A plasma is considered ideal if it shows collective behaviour and consequently the collective electrostatic collisions are dominant compared to single particle collisions.
For an intense laser pulse interacting with a solid target, a plasma is formed on the laser incident front side. For ultra-high intensities this plasma is generated, before the main laser pulse arrives. Therefore, the interaction of electromagnetic radiation with this so-called pre-plasma is important. The expansion or compression of the plasma is critical, as the main pulse will interact with a plasma density gradient, rather than an undisturbed solid. This is especially true for the scope of this work, where the plasma formation and expansion is altered dramatically by a microstructured target front.

For an ultra-short laser pulse during the interaction a strong non-equilibrium in temperature (T_e, T_i) and density (n_e, n_i) between electrons and ions is generated, as the mass of the electrons is orders of magnitude lower than that of even the lightest ions. Furthermore, during the short pulse ions can be considered as quasi-stationary, as described above.
An electromagnetic wave travelling through a plasma will act on the electrons generating a feedback onto the propagating wave and dramatically alter the dispersion relation. An elaborate derivation of this dispersion relation from Faraday's law can be found in the work of *Mulser and Bauer*.[48] As a result, the dispersion relation reads

$$\omega^2 - \omega_p^2 = k^2 c^2 \quad \text{with} \quad \omega_p^2 = \frac{n_e e^2}{\gamma m_e \epsilon_0}. \tag{2.24}$$

Thereby, the electron mass is considered relativistic with Lorentz factor $1/\gamma^2 = 1-(v^2/c^2)$, where v is the velocity of the particle. The characteristic plasma frequency ω_p depends only on the electron number density n_e. A critical density n_c is defined, where $\omega_0^2 - \omega_p^2 = 0 = k^2 c^2$ and the electromagnetic wave cannot further propagate:

$$n_c \cdot e^2 = \gamma m_e \epsilon_0 \omega_0^2, \tag{2.25}$$

with laser frequency ω_0. The electromagnetic wave will decay exponentially with a gradient known as skin depth δ and is absorbed by the plasma. For high intensities ($10^{18}\,\mathrm{W/cm^2}$) the velocity of the electrons have to be considered relativistic and electrons are pushed in the direction of the laser.

2.3.4 Laser-driven acceleration of particles

In a plasma interacting with a laser field electrons will experience a force while the ions can be considered stationary on short time scales. Absorption of the laser energy to the plasma is typically divided into collisional and collisionless absorption. For collisional absorption or inverse bremsstrahlung, electrons in a plasma oscillate at relative low intensity laser fields ($10^{12} \ldots 10^{15}\,\mathrm{W/cm^2}$).[11] The electron gains energy from the laser field and collides with ions that are present in the plasma. This absorption mechanism is dominant for long scale lengths and low temperatures. Thereby, the collision frequency with ions will decrease as the kinetic energy of electrons increases.

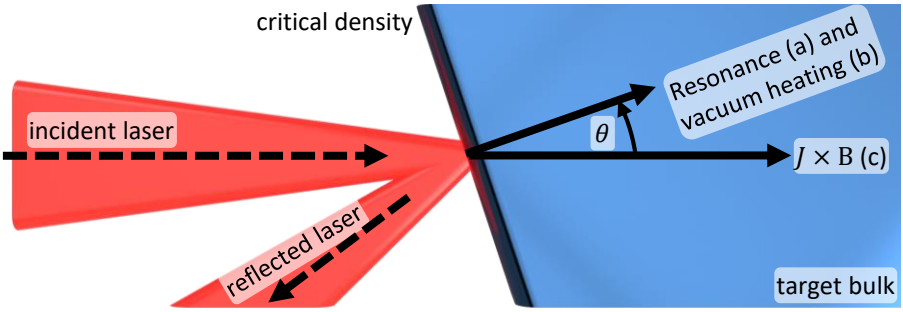

Figure 2.7.: The three main absorption mechanisms for electromagnetic radiation incident under an angle θ into a plasma region are illustrated. *Resonance heating* drives a resonant wave of electrons into the target from the critical density if an initial plasma scale length is present (a). With *vacuum heating* electrons are pulled from the target surface to the surrounding vacuum and accelerated back into the target during one full cycle of laser oscillation (b). For high laser intensities $J \times B$ *heating* drives relativistic electrons past the critical density in the forward direction of the electromagnetic wave (c). For *resonance* and *vacuum heating* electrons are accelerated perpendicular to the target surface.

Figure 2.7 illustrates the three basic collisionless absorption mechanisms (*resonance heating* (a), *vacuum heating* (b) and $J \times B$ *heating* (c)) relevant to this work, in relation to the incident and reflected laser pulse and orientation of the target.
For a collisionless process called *resonance absorption* (a) an initial plasma scale length must be present and the p-polarised laser is incident at an angle to the target surface. As the laser propagates into the plasma the electron density increases. At the critical density due to this gradient laser and plasma frequency are matched and a resonant wave of energetic electrons is driven into the target. For shorter scale lengths electrons can be pulled from the plasma surface to the vacuum in one half cycle of the laser oscillation and are accelerated into the target on the second half. Thereby, the laser has to be polarised perpendicular to the target surface. This process is called *vacuum heating* (b).[49]
For high intensities and relativistic electron velocities the magnetic field of the driving electromagnetic wave becomes relevant. The electrons are forced to

[49] W. L. Kruer and K. Estabrook. *Phys. Fluids* **28**, 430–432, 1985.

move past the critical density (in the direction of the laser). This process is called $J \times B$ *heating* (c) and independent on the laser polarisation.[49] In contrast to resonance absorption and vacuum heating the electrons are accelerated in the direction of the laser axis and not perpendicular to the target surface.
With high energetic electrons propagating through the target intense currents up to several 10^6 A over a small circular spot of 10 µm are abounded.[14] The highest current exists in the electron beam centre. This energetic flow of carriers must be neutralised locally by a return current. Otherwise, powerful magnetic fields are induced that stop the electrons in contrast to the observation of electrons leaving on the target backside. A fraction of the carriers is even passing the target bulk coherently to the incident electromagnetic wave. The neutralising current draws electrons from the surrounding plasma region and consists of a higher number of low energetic electrons. The target is heated, in particular by these low energetic carriers.
The energy of the electrons travelling through the target obviously depends on a number of factors and results in a time averaged random distribution. Considering electrons in a non-relativistic way, the distribution can be approximated by a Maxwell-Boltzmann distribution with a single electron temperature T_e[50]

$$f(E_e) = N_e \cdot \sqrt{\frac{4E_e}{\pi (k_B T_e)^3}} \cdot \exp\left[-\frac{E_e}{k_B T_e}\right], \tag{2.26}$$

with Boltzmann constant k_B, electron energy E_e, mean temperature T_e and total number of electrons N_e. For laser intensities greater than approximately $10^{18}\,\mathrm{W/cm^2}$ this distribution has to be modified to account for relativistic effects. The resulting distribution follows the so-called Maxwell-Jüttner distribution[51]

$$f(\gamma) = N_e \cdot \frac{v}{c} \cdot \frac{\gamma^2}{\alpha_e K_2(1/\alpha_e)} \cdot \exp\left[-\frac{\gamma}{\alpha_e}\right], \quad \text{with} \quad \alpha_e = \frac{k_B T_e}{m_e c^2}, \tag{2.27}$$

and the Bessel function of the second kind K_2. The number of electrons N_e depends on the electron temperature T_e and the amount of laser energy absorbed by the target. Note, that an increased amount of laser energy does not automatically yield an enhanced electron energy.

[50] B. Bezzerides, S. J. Gitomer, and D. W. Forslund. *Phys. Rev. Lett.* **44**, 651–654, 1980.
[51] F. Jüttner. *Annalen der Physik* **339**, 856–882, 1911.

Furthermore, by the propagation of energetic ions through the target x-ray radiation is generated. Above all, the bremsstrahlung spectrum depends on the flux and temperature of the electrons and thereby enables a prediction for the initial interaction strength of the laser with the target.

In addition, high energy ions are observed for the interaction of an intense laser field with a solid target. The reason for that is again the travel of energetic electrons through the target bulk. When the electron beam reaches the sharp transition between the target backside and the surrounding vacuum, a strong charge unbalance is created. Thereby, a sheath field of electrons is induced on the backside of the target. The extent of this electron sheath is typically on the order of the electron Debye length $\lambda_e = \sqrt{\epsilon_0 k_B T_e / n_e e^2}$[14] with electron density n_e.

The strong electric and magnetic fields involved capture a part of the electrons and ionise atoms on the target backside which are accelerated perpendicular to the target backside (electron sheath). Depending on the form of the electron sheath, the emitted ion beam shows a strong collimation and low emittance. This process is called *target normal sheath acceleration* (TNSA). The outermost layer of ions on the target backside is exposed to the strongest electric field gradients. And as typically a proton rich contamination layer of several atomic layers thickness is existent on the target backside, protons gain the most energy and are accelerated first. In addition, they shield the field from ions in successive layers of the target backside.[52] Even so, the population of heavier ions is accelerated effectively, once the proton number has dropped significantly.

It is worth mentioning, that in addition to the acceleration of ions from the target backside through TNSA, other acceleration mechanisms and directions are possible, like the acceleration of ions from the target front. Successively limiting the target thickness (and mass), acceleration mechanisms like *radiation pressure acceleration* (RPA), *collisionless shock acceleration* (CSA) and *breakout afterburner* (BOA) dominate.[14] For the scope of this work however, where comparably thick targets are employed only backside and frontside emission on the basis of the TNSA mechanism are important.

Concluding, the following three processes are important for the acceleration of energetic ions:

1. Coupling of intense laser energy into the electrons of the target bulk (laser absorption).

[52] G. Hoffmeister et al. *Phys. Rev. Spec. Top. - Accel. Beams* **16**, 041304, 2013.

2. Laser-driven expansion of plasma and generation of high field gradients.

3. Acceleration of ions.

Thereby, the TNSA process can be significantly controlled and optimised by changing the laser pulse parameters, material or shape of the irradiated target. Within this work the acceleration process is altered dramatically by structuring the front surface incident to the laser. The generation of these microstructures and fundamental achievements within this field is described in the following section.

2.4 Scientific work within the field

The following sections demonstrate accomplishments in the field of targetry for laser-plasma experiments and the laser-driven fabrication of microstructures on silicon. The publications and work shown is an important motivation for the work presented in the framework of this thesis.

2.4.1 Targets for laser-plasma experiments

Decades after the first proposal for a plasma-based acceleration mechanism for ions in 1957 by *V. Veksler*[53] advanced and intense radiation sources became available with the demonstration of the titanium:sapphire laser,[41] Kerr lens mode-locking[34,54] and chirped pulse amplification (CPA).[43] Therewith, ultra-short laser pulses and intense peak powers became available (see section 2.2). In the year 2000, three independent publications (*Snavely et al.*,[55] *Clark et al.*,[56] *Maksumchuk et al.*[57]) demonstrated the acceleration of protons to multiple MeV using a laser-driven source (see section 2.3.4). Further improvements were demonstrated with laser-driven x-ray lasers,[58] high harmonic generation and attosecond laser pulses,[37] laser-accelerated electrons[59] and ions.

[53] V. I. Veksler. *Sov. J. At. Energy* **2**, 525–528, 1957.
[54] N. Sarukura, Y. Ishida, and H. Nakano. *Opt. Lett.* **16**, 153–155, 1991.
[55] R. A. Snavely et al. *Phys. Rev. Lett.* **85**, 2945–2948, 2000.
[56] E. L. Clark et al. *Phys. Rev. Lett.* **85**, 1654–1657, 2000.
[57] A. Maksimchuk et al. *Phys. Rev. Lett.* **84**, 4108–4111, 2000.
[58] H. Daido. *Reports Prog. Phys.* **65**, 1513, 2002.
[59] E. Esarey, C. B. Schroeder, and W. P. Leemans. *Rev. Mod. Phys.* **81**, 1229–1285, 2009.

The fast development and research in the field of laser-driven acceleration is demonstrated in a number of excellent review publications on ion acceleration,[10,13,14] optics in the relativistic regime[12] and target fabrication.[15]

As described in section 2.3.4, the following three processes are important:

1) coupling of intense laser energy into the electrons of the target (absorption),
2) laser-driven expansion of plasma and generation of high field gradients and
3) the acceleration of ions.

A permanent drive for further progress in laser-driven acceleration is achieving higher ion energies, improve conversion efficiency of laser energy to ions, reduce divergence of the ion beam, control the energy spectrum and achieve consistent results and overall reliability. Keep in mind that plasma-based acceleration of particles is highly intricate and depends strongly on the experimental conditions and numerous parameters. While high peak power laser systems are permanently improved gaining higher repetition rates, better stability and generating cleaner and shorter pulses spatially and temporally, the core of controlling the interaction is and will be the target design.

Developing and fabricating optimised targets is an ongoing drive for further improvement and understanding of the acceleration mechanism. Targets most commonly used are solid flat foils. In addition, gaseous, liquid, cryogenic, hemispherical, hemicylindrical and more complex combinations have been demonstrated.[15,60]

Developing a target with a nano- or micro-structured surface on the laser incident side has been shown to boost the absorption of laser light[61–64] and to enhance the generation of relativistic electrons,[17,65] the acceleration of ions[16] and the production of bremsstrahlung.[66,67] In comparison, for polished flat targets a large portion of the laser light during the interaction is reflected from the critical density layer of the created plasma on the target surface.

With high-repetitive laser-systems and experiments in mind, a reduced complexity and high repeatability is strongly desirable. With user facilities of

60 V. Malka et al. *Nat. Phys.* **4**, 447–453, 2008.
61 H. Habara et al. *Phys. Plasmas* **23**, 063105, 2016.
62 K. A. Ivanov et al. *Laser Phys. Lett.* **12**, 046005, 2015.
63 L. Cao et al. *Phys. Plasmas* **18**, 054501, 2011.
64 M. C. Levy et al. *Nat. Commun.* **5**, 4149, 2014.
65 S. Jiang et al. *Phys. Rev. E - Stat. Nonlinear, Soft Matter Phys.* **89**, 013106, 2014.
66 S. Jiang et al. *Eur. Phys. J. D* **68**, 283, 2014.
67 G. Kulcsar et al. *Phys. Rev. Lett.* **84**, 5149–5152, 2000.

several Hz to kHz repetition rate, a controllable and characterisable batch fabrication method of a simple target design is unpreventable.
The essence of this work is the development of a simple, fast and affordable fabrication method for micro-structured targets that generate an enhanced and reliable source of ions, electrons and x-ray radiation. Related work for the generation of these micro-structures is presented in the following section.

2.4.2 Fabrication of microstructures

The work of *Her et al.* in 1998 reported the observation of sharp conical spikes after repeatedly irradiating a silicon surface with intense femtosecond laser pulses.[25]
The resulting modifications of a crystalline silicon surface illustrated in this seminal publication are shown in figure 2.8. Employing a sulphur containing gaseous atmosphere during irradiation the resulting structure (a) is sharper and more directed in comparison to processing in vacuum (b). The process of fabricating these surface structures is straightforward. A silicon substrate is placed inside a sealed chamber (filled with sulphur hexafluoride at 800 mbar (a) or evacuated to 0.1 mbar vacuum (b)). Femtosecond laser pulses with a wavelength of 800 nm and pulse energy of 500 µJ are focussed to a 200 µm diameter spot ($1/e^2$) on the silicon surface using a 0.1 m focal length lens. The substrate is then exposed to 500 laser pulses and the structure evolves.[25]
The height and distance of the conical spikes is defined by the laser fluence on the surface. A Gaussian intensity distribution was existent on the substrate for the structures presented in figure 2.8. The size and separation of the needles in sulphur hexafluoride and vacuum follow this intensity distribution clearly. At lower intensities the spikes are smaller in height and distance. At the highest fluence of energy, the needles are also highest and most separated.
Even so observation of laser-induced periodic surface structures (LIPSS) were described since the 1970's[24,68,69] (shortly after the first laser was built[33]), the formation of sharp needles is a technological innovation with important properties. The laser-driven modifications of the silicon surface topography changes the optical properties remarkably.[26] In particular, the absorptance (the calculated, quantitative measure of the amount of absorption) of light is increased dramatically, decreasing reflection and scattering from the surface.

[68] M. Birnbaum. *J. Appl. Phys.* **36**, 3688–3689, 1965.
[69] H. M. Van Driel, J. E. Sipe, and J. F. Young. *Phys. Rev. Lett.* **49**, 1955–1958, 1982.

Figure 2.9 shows absorptance measurements taken with an UV-Vis spectrophotometer with an integrating sphere detector, as published by *Sheehy et al.*:[26] Here, the influence of different processing gases is demonstrated for (a) H_2S. (b) SF_6, (c) SiH_4 and (d) H_2 in comparison to unstructured crystalline silicon (e). Silicon has a band gap of approximately 1.1 µm.[70] The absorptance measurement (figure 2.9) shows a notable increase for the spectral range covered from 0.25 µm to 2.5 µm due to various reasons.

For wavelengths below the band gap the absorptance is primarily enhanced through the increased interacting surface area and the number of multiple reflections due to the high aspect ratio.[70,71] For sulphur containing gases a further boost is observed because of the very sharp tips of the cones (compare to the electron micrographs in figure 2.8).

For wavelengths above the band gap a strong dependence of the absorptance value to the process substance employed is visible. This demonstrates a strongly altered band structure of the silicon substrate. More precisely, high concentrations of elements from the ambient gas and surface oxide layer on the silicon substrate are incorporated into the surface.[70] Especially halogens create volatile compounds with silicon and show an increased chemical reaction in the presence of intense laser pulses. Especially sulphur impurities on the walls of the cones play a role in the particularly high absorptance for (a) and (b).

Furthermore, the photo current generated with the micro-structured surfaces is significantly enhanced. In particular, the absorption of wavelengths above band gap is a promising indication for a number of applications.[6,9] The list of proven and possible applications is wide.[72] Thereby, the modified optical properties are of high value as well as the geometric topography. With *SiOnyx LLC* the first company is producing micro-structured image sensors with increased sensitivity and thermal imaging cameras.[73] The boosted light absorption of structured silicon is a great promise for solar applications. In fact, photovoltaic cells with enhanced efficiency have been demonstrated, using laser structured silicon.[7,72] Even so, micro-structured silicon can also be produced using techniques like electrochemical etching, stain etching, metal-assisted chemical etching or reactive ion etching,[72] the implementation of a laser treatment process is more straightforward for this thesis.

[70] R. Younkin et al. *J. Appl. Phys.* **93**, 2626–2629, 2003.
[71] T. H. Her et al. *Appl. Phys. A Mater. Sci. Process.* **70**, 383–385, 2000.
[72] X. Liu et al. *Energy Environ. Sci.* **7**, 3223–3263, 2014.
[73] M. U. Pralle et al. *Proc. SPIE* **8704**, 8704 –8704 –7, 2013.

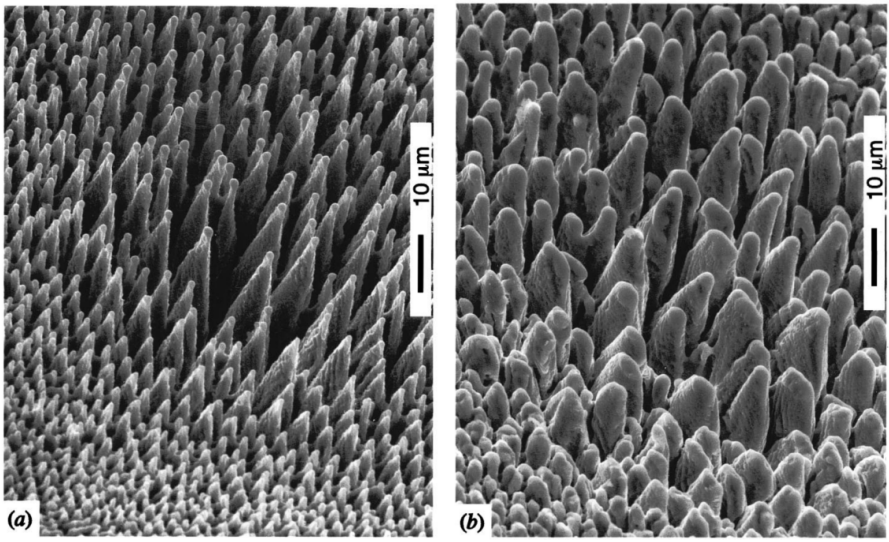

Figure 2.8.: Comparison of laser-induced microstructures fabricated in sulphur hexafluoride (a) and vacuum (b). By focussing 500 femtosecond laser pulses with a spatial Gaussian intensity profile on a silicon substrate, these structures evolve through ultrafast ablation. The varying height and separation of the evolving structural features depend on the energy fluence for both cases. The higher intensities per area generate larger separation and a deeper structural height. The influence of an ambient gas is obvious between (a) and (b). Employing a gaseous sulphur hexafluoride atmosphere, sharp conical needles evolve in comparison to blunt inhomogeneous features in vacuum. Reproduced from ref. [25] (figure 2), with the permission of *E. Mazur* and *AIP Publishing.*

Femtosecond processed silicon combines the structuring process with modification of the optical properties, as described above. The latter are of particular interest using the structures in laser-driven applications, as outlined in the following chapters. In addition, sharp conical silicon spikes offer an increased surface area and more bulk material in comparison to e.g. thin silicon wires produced with metal-assisted chemical etching.
Within this thesis, micro-structured silicon is employed to the field of laser-driven particle acceleration. The work presented in this section is basis to the development and implementation of a structuring setup using femtosecond laser pulses in a sulphur hexafluoride ambient. Following, the experimental implementation is presented in chapter 3. Afterwards, Part II shows the application of micro-structured targets produced with this setup in a high power laser plasma experiment.

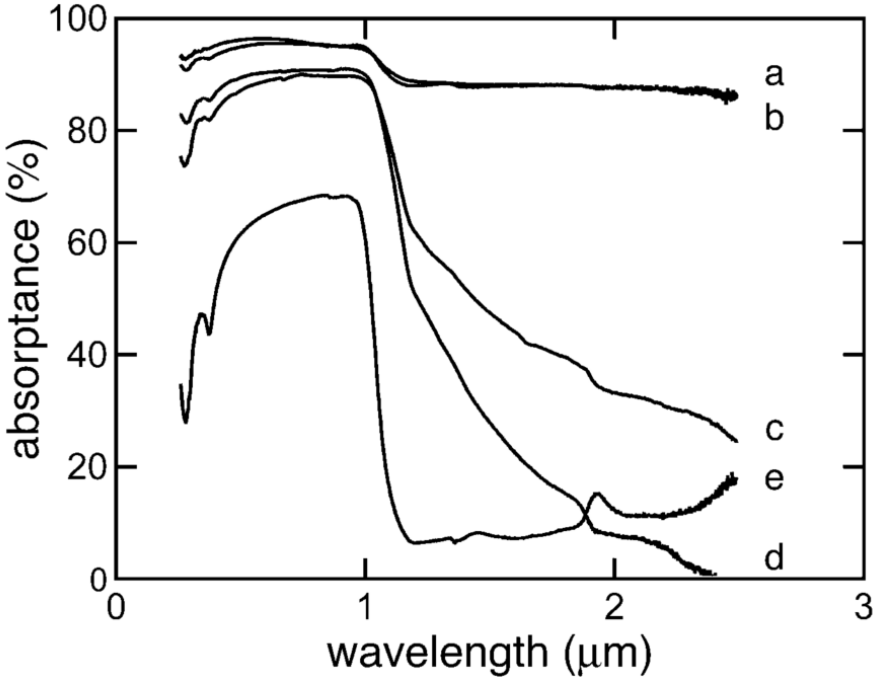

Figure 2.9.: The gaseous process medium has a strong impact on the amount of absorption of the structured surface. The increased absorptance is shown in comparison to unstructured silicon (e) for the different process gases H_2S (a), SF_6 (b), SiH_4 (c) and H_2 (d). For wavelengths below the bandgap of silicon (approximately $1.1\,\mu m$) a general increase in absorptance is observed due to the geometric trapping of light. For wavelengths above the bandgap, in contrast, the absorbed amount is strongly depending on the medium employed. For sulphur containing gases an increase to up to $90\,\%$ is observed. This is explained through high concentrations of sulphur incorporated into the surface of the silicon needles. Thereby, the band structure is significantly altered and the absorptance increases. Reprinted with permission from ref. [26] (figure 2). Copyright ©2018 American Chemical Society.

3 Experimental implementation

A novel processing and production setup using ultra-short laser pulses was planned, established and characterised within the scope of this work and is an addition and improvement to equipment and techniques existent for the manufacturing of targets in the *Detektor- und Targetlabor* of the *Institut für Kernphysik*. This chapter describes the key elements of the system necessary to generate micro-structured silicon. The description focusses primarily on appended or adapted systems and methods developed within this thesis. It is divided into three parts: identification of required as well as ideal parameter ranges for the experimental setup, adoption of the laser system to enable and monitor these parameters and finally the implementation of processing setups for different approaches and materials.

3.1 Required components and parameters

As described in section 2.4, a number of publications focus on the laser-driven generation of nano- and micro-structured surfaces within a range of materials, processing media and possible applications. The scientific work achieved in this field facilitates the thorough identification of parameters for a preferably ideal and versatile processing setup. The summary presented here focusses on micrometre-scale structures on mono-crystalline silicon with the intention to produce targets for high-intense laser-plasma experiments, as described in part II of this thesis. First, the necessary components are shown. In the following paragraphs, the needed parameter ranges are explained.
Central requirement for the structuring setup is the interaction of ultra-short laser pulses with the surface of a thin silicon substrate in an enclosed container. Different solid, liquid and gaseous media should be used at different pressures. This demands particular precaution when planning the processing chamber. An idealised schematic overview of the chamber is shown in figure 3.1 to illustrate the requirements for implementation of the structuring.
The silicon substrate is attached to a holder, which is intended to establish a repeatable position in the system and at the same time allows for a simpli-

Table 3.1.: A number of precisely tuned laser parameters is necessary for the successful laser-driven generation of microstructures. The table summarises the critical properties and ranges derived from section 2.4. The central wavelength λ_P is common for titanium:sapphire based systems that generate sub-ps laser pulses. Ideally, pulse length Δt_P, number of pulses N_P and fluence $\mathscr{F}$ are fixed to be within the ranges shown. The overall size of the structure is defined by the beam diameter $2w_{\text{surface}}$ and the structuring technique employed (fixed position or scanning).

central wavelength	λ_P	$\sim 800\,\text{nm}$
number of pulses	N_P	$100 \ldots 1000$
pulse length	Δt_P	$50 \ldots 500\,\text{fs}$
beam waist on surface	$2w_{\text{surface}}$	$50 \ldots 500\,\mu\text{m}$
energy fluence on surface	$\mathscr{F}$	$0.1 \ldots 1\,\text{J/cm}^2$

fied handling for characterisation and further processing. The chamber can be sealed and connected to a gas, vacuum and filtering system. Thereby, gaseous atmospheres below ambient pressure can be used. Additionally, liquid media in combination with a fluid level sensor can be utilised. The materials used for the processing chamber and components should endure the chemical and pressure stress.

From above, the laser pulses are focussed into the chamber. Thereby, the optional top sealing cover is transparent and anti-reflective for the laser wavelength employed. With a given processing chamber, the fine adjustment and characterisation of laser parameters is crucial for a successful generation of surface structures. The inset of Figure 3.1 illustrates substantial properties of the laser radiation.

A total number N_P of pulses is focussed onto the silicon surface. Individual pulses are characterised by their temporal length τ_P and shape $I_P(t)$, central wavelength λ_P, energy surface fluence $\mathscr{F}$ and polarisation $\vec{E}_P$. Furthermore, the intensity distribution $I_P(x, y)$ on the illuminated surface area is important. The amount of laser parameters in combination with the processing medium primarily dictates the shape, size and homogeneity of the resulting surface structure. Hence, the value and range of these parameters is of particular interest together with precisely maintaining and characterising them.

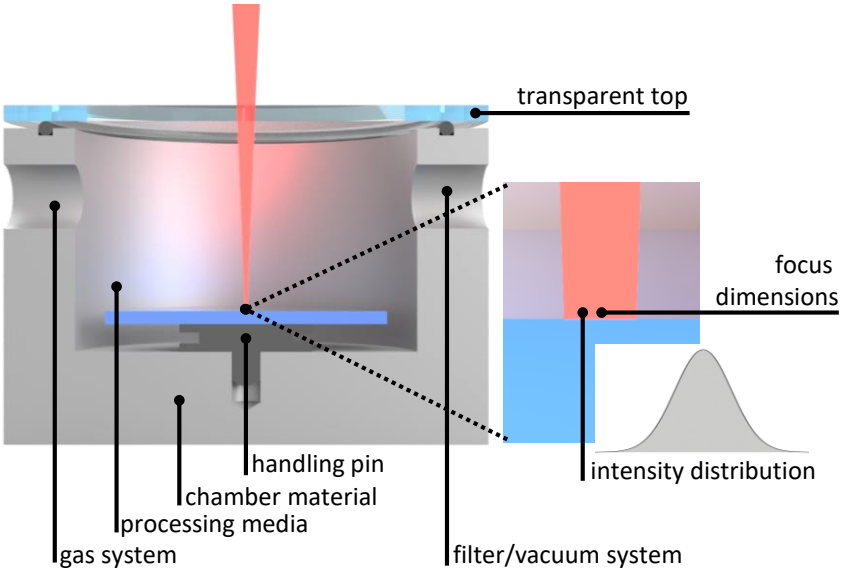

Figure 3.1.: Schematic illustration of an ideal fabrication and processing setup. The focussed laser radiation enters the chamber through a window from the top. The container can be sealed, evacuated and filled with a liquid or gaseous processing substance. The chamber is connected to a gas, vacuum and filtering system. For alignment and easy processing, the silicon substrate is attached to a standardised handling pin that is compatible to the scanning electron microscopes used. The intensity distribution of the focussed laser light on the silicon surface is a crucial parameter for success and repeatability of the fabrication process. For fine adjustment the container is attached to a motorised positioning system.

Table 3.1 summarises sensible parameter ranges and properties, as derived from section 2.4, suitable to generate micrometre sized needle structures.

A central wavelength λ_P of 800 nm is an established standard for the generation of femtosecond laser pulses and proved to be working for the microstructuring process. In addition, frequency doubled 400 nm radiation is conceivable. Typically, the silicon surface is irradiated by a number of 500 to 600 pulses to obtain the final structure dimensions. A bigger range is necessary for parameter studies and ideally single or very few laser pulses can be used. As described in section 2.4, the pulse length needs to be shorter than the relaxation time of the silicon crystal. Typically, pulse lengths around 100 fs are applied. Regarding the outline dimensions of the surface for applications in laser-driven experiments a homogeneous structured circular region of up to 500 µm in diameter ($2w_{\text{surface}}$) is expedient. The homogeneity thereby is critical and in particular influenced by the uniformity of the lateral laser intensity distribution $I_P(x, y)$ on the silicon surface. A sharp rectangular distribution (top-hat) is desirable, creating a more complex optical setup. A straightforward approach is the application of a uniform Gaussian intensity distribution. Usually a laser energy fluence of 0.5 to 0.8 $\mathrm{J cm^{-2}}$ is employed.

In summary, the generation, maintenance and characterisation of laser pulse parameters is essential for the successful implementation of a laser-driven surface structuring. The laser system, which was extended and adapted for this purpose during the thesis presented here, is described in detail in the following section. Subsequent, functional arrangements for the processing setup are presented.

3.2 Laser system

The following section describes the comprehensive extension and adaption of the laser system as a source for the surface structuring setup. At the start of this thesis in the *Detektor- und Targetlabor* of the *Institut für Kernphysik*, a femtosecond laser system for the purpose of precise material machining (e.g. cutting) existed that is used and adapted for the fabrication setup.

Figure 3.2 illustrates a schematic overview of the laser system from the laser source to the two processing setups. The individual elements are described in more detail in the following subsections. In this illustration, components are coloured as green (developed and constructed within this thesis), blue (exis-

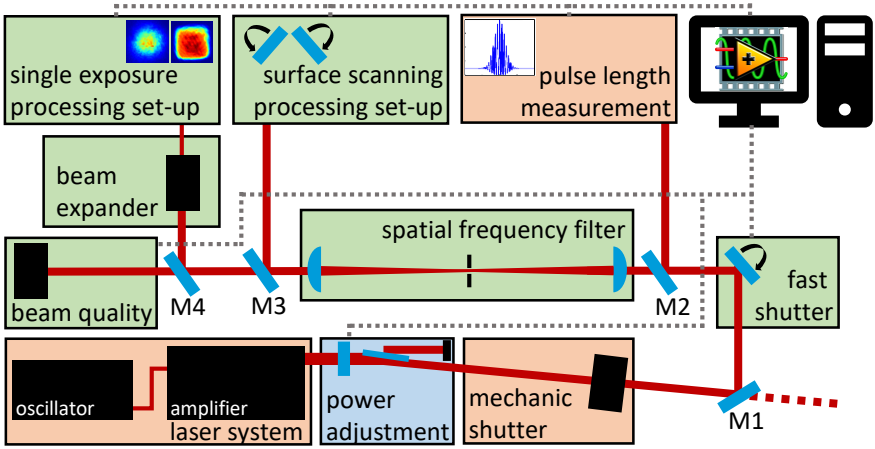

Figure 3.2.: Schematic overview of the laser system set up and used in this work. The two staged laser source consists of an ultrafast oscillator and amplifier. A motorised stepless power adjustment controls the laser pulse energy. The combination of a mechanical and galvanometric shutter allows for fast switching of the laser source. An optional autocorrelator is used to measure the pulse length. A spatial frequency filter generates a homogeneous beam profile that can be monitored. Two individual setups for the fabrication of microstructures allow for either surface scanning or single exposure of the silicon substrate with a precisely tuned intensity distribution of the laser pulse.

tent, but adapted within this thesis) or orange (existent, no major adaption within this work).

After leaving the two-staged source (section 3.2.1), the radiation is directed through a power adjustment system (section 3.2.2). Therein, the average power (pulse energy) can be adjusted continuously between approximately 25 mW (5 µJ) and 1000 mW (200 µJ). This system is automated within this thesis to be precisely controlled by a computer as afore only manual operation was possible.

After the power adjustment, a mechanical shutter can block the laser light controlled manually or by a digital signal. With mirror M1, the pulses are then directed into the beam line of the processing system. The mirror is mounted on a magnetic base and can be removed to use the laser within other setups in the laboratory and easily repositioned when the structuring setup is used. As the

opening and closing time of the mechanical shutter is comparably slow, a fast alternative shutter (section 3.2.3) was constructed within this work, relying on a motorised rotating mirror (galvanometer) in combination with an aperture. The normally removed mirror M2 can direct the light into the autocorrelator setup (section 3.2.4) in order to determine the average laser pulse length τ_P present in the system.
With a spatial frequency filter developed (section 3.2.6), perturbations in the phase front of the laser pulse are reduced. This filter system consists of a Kepler[45] telescope with an aperture in the focal plane. With the right aperture diameter a lateral Gaussian intensity profile with higher quality is generated, while keeping energy losses in the system to a minimum.
Different techniques for the characterisation of the beam intensity profile (section 3.2.5) were implemented within the scope of this work. The homogeneity and dimensions of the intensity distribution have a critical influence on the quality of structured surfaces. Thus, several orders of magnitude in dimension and intensity can be covered to evaluate the profile of the collimated and the focussed beam.
Mirror M3 is inserted to use the developed scanning setup (section 3.2.7). Therein, a galvanometric xy scanner with adaptable focussing lens rasterises the silicon surface to generate structures of larger dimensions. Mirror M4 is used for the second acquired processing setup to employ single exposure with custom intensity profiles. Here a Gaussian or rectangular distribution is applied.

3.2.1 Ultrafast laser source

In this work, a two-staged laser source is utilised, consisting of a primary titanium:sapphire laser (subsequently called oscillator) which feeds a secondary titanium:sapphire regenerative amplifier (subsequently called amplifier). Figure 3.3 illustrates a simplified schematic of both connected devices. For the general working principal of a titanium:sapphire laser refer to section 2.2.1.
The mode-locked oscillator is a model *Griffin-3*[74] manufactured by *KMLabs Inc*. The optical pump (PUMP1) is a continuous wave diode-pumped solid-state laser (DPSS) with a central wavelength of 532 nm (TEM_{00}) and power of 4 W.

[74] Griffin - Ultrafast Ti:sapphire oscillator series. KMLabs Inc. URL: https://kmlabs.com/wp-content/uploads/2017/02/km_labs_Griffin_datasheet_180125.pdf (accessed 01 April 2018).

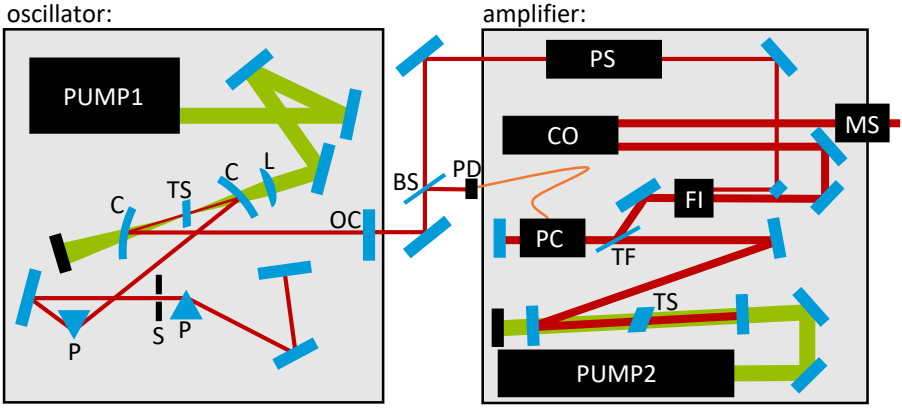

Figure 3.3.: Schematic overview of the two-staged ultrafast laser source. The oscillator (left), type *Griffin-3*, generates laser pulses with a length of $50\,\mathrm{fs}$ to $100\,\mathrm{fs}$. A titanium:sapphire crystal is optically pumped with a DPSS laser (PUMP1) and lens (L) and placed in between to concave mirrors (C). The resonator is based on the technique of passive mode-locking utilising the Kerr lens effect. An aperture (S) lets high intense pulses pass while blocking cw radiation. A constant phase relation between the longitudinal modes is achieved with a dispersive prism pair (P). The pulsed radiation leaves the oscillator through a partially reflective mirror (OC).
The laser pulses are synced to the operation of the amplifier (right), type *Integra-C.X.-1.0-T*, with a photodiode (PD) and beam sampler (BS). Relying on the technique of *chirped pulse amplification* the laser pulses are stretched in the temporal domain (PS) and coupled into the amplifier resonator. Therefore, a Pockels cell (PC), thinfilm polariser (TF) and Faraday insulator is used also to direct the pulses out of the amplifier. The regenerative amplifier is again based on a multipass titanium:sapphire crystal pumped by a DPSS laser. After amplifying and decoupling the pulses from the resonator, a grating compressor (CO) is used. A mechanical shutter (MS) blocks the radiation when needed.

The titanium:sapphire crystal (TS) is positioned between two curved mirrors (C) and excited by the focussed pump radiation (lens L) within a complex folded linear cavity. To compensate for dispersive pulse broadening, a prism pair (P) is used to compress the laser pulse within the resonator. Passive mode-locking in the cavity is achieved with a tuning slit (S) utilising the Kerr effect. Thus, in the resonator, pulsed oscillation builds up and leaves through a partially transparent output coupler (OC). The oscillator has a repetition rate of 86 MHz, emitting a central wavelength of 790 nm (±10 nm bandwidth, TEM_{00}) and a pulse length of 50 fs to 100 fs with an average power of 0.3 W. After the oscillator, the radiation is passed into the amplifier. As timing signal, a small fraction of energy is directed on a photodiode by an optical beam splitter element (BS). This signal is needed by the amplifier.
The amplifier is a model *Integra-C.X.-1.0-T*,[75] manufactured by *Quantronix Corp*. The principle of *chirped pulse amplification* (CPA), as described in section 2.2.2, is used in combination with a regenerative amplifier. First, the pulses arriving from the oscillator are stretched in the time domain with a pulse stretcher (PS) to decrease the peak intensity. A Pockels cell (PC), thin film polariser (TF) and Faraday isolator (FI) are used to insert a single chirped pulse into the resonator, where it makes 10 to 20 roundtrips for amplification and is again extracted by the Pockels cell system. The folded linear cavity is constructed analogue to the oscillator. Here, a Q-switched DPSS laser (PUMP2) is used as a pump with a central wavelength of 527 nm and pulse length of 150 ns with an average power of 30 W. After extraction, the pulse is compressed in the pulse compressor (CO) and leaves the amplifier, controlled by a motorised shutter (MS). The amplified pulses have a central wavelength of 795 nm (±10 nm Bandwidth) with a pulse length of approximately 100 fs and a repetition rate of 5 kHz. With an average power of approximately 1 W, the maximum pulse energy is 200 µJ. The beam quality (TEM_{00}) is specified by the manufacturer to satisfy $M^2 < 1.3$.

3.2.2 Stepless adjustment of laser power

After the laser source, the power can be adjusted with a half-wave plate in combination with a thin film polariser. Figure 3.4 shows a schematic of the operation principle of the power adjustment.

[75] Ti:sapphire - Ultrafast amplifiers. Quantronix Corp. URL: http://www.quantron.com/files/dl/Integra-C%20v8.pdf (accessed 01 April 2018).

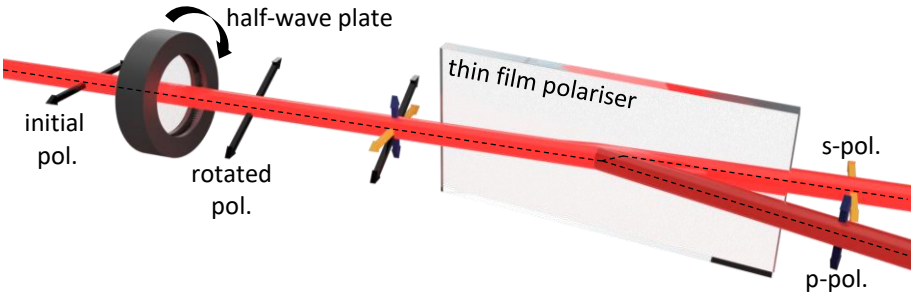

Figure 3.4.: Schematic setup for the stepless power adjustment using a thin film polariser in Brewster configuration. Here, parallel polarised components (p-like) of the electric field are transmitted and perpendicular components (s-like) are reflected. The radiation leaving the amplifier is perpendicular polarised. Using a half-wave plate, this initial polarisation can be rotated and the reflected p-like component is directed to the experiment. Within the scope of this work the half-wave plate is motorised and controlled by a computer programme.

The linear polarisation of the laser pulse is rotated as a function of the angular position of the $\lambda/2$ plate. The thin film polariser in Brewster configuration reflects s-like (perpendicular) polarisation while transmitting p-like (parallel) components with respect to the polariser. By rotating the wave plate, the energy ratio between reflected and transmitted radiation can be controlled. The transmitted portion is blocked within a laser beam dump, reflected radiation used in the experiment.

As the average power has to be adjusted very precisely for the structuring process, rotation of the half-wave plate is motorised during this work and controlled by a computer programme. Beforehand, the adjustment was only possible manually, rotating the holder by hand. A new mount for the optic, driven by stepper motor with worm drive gear arrangement has been developed. The system is controlled by a proprietary designed *LabVIEW™* computer programme.

The calibration of the power adjustment system is shown in Figure 3.5. Thereby, the half-wave plate is rotated stepwise in between 0° and 180° while measuring the average laser power $\bar{\mathcal{P}}$ over a period of 10 s per angular position θ with a calorimetric power meter. The resulting graph follows a model of the form

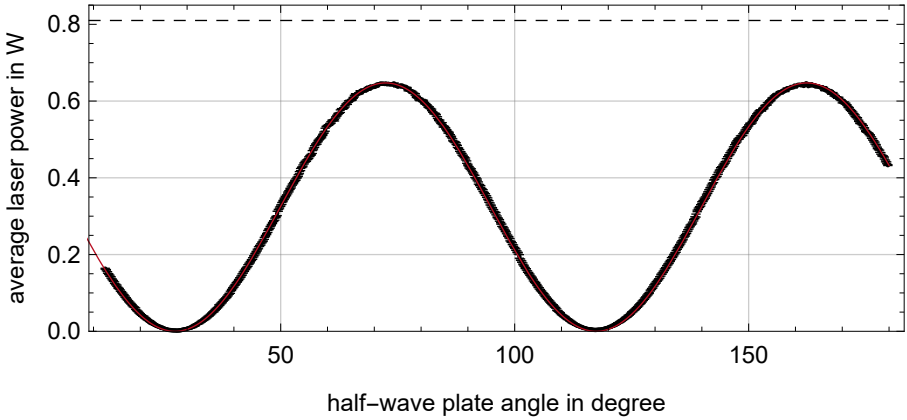

Figure 3.5.: Calibration of the stepless power adjustment. The half-wave plate (compare to figure 3.4) is rotated stepwise between $0°$ and $180°$ measuring the average laser power (black). The input laser power is $810\,\mathrm{mW}$. The associated $cos^2(\theta)$ dependency is shown in red yielding a maximum reflected output power of $650\,\mathrm{mW}$. With this a fixed relation of half-wave plate angle θ and power output for the automated system is achieved.

$$\tilde{\mathscr{P}} = 0.64(7) \cdot \cos^2(2\theta + 35.1(8)°) \tag{3.1}$$

that is shown in red in figure 3.5. With this calibration function, the power can be adjusted automatically using a dedicated computer programme. With an input laser power of 810 mW the maximum output achievable is approximately 650 mW resulting in an extraction efficiency of 80 % in reflection.

3.2.3 Fast galvanometric shutter

The mechanical shutter already existent in the system for opening and closing the laser line is not suited for the processing setup for structuring. A minimum opening time of approximately 25 ms equals a number of roughly 125 laser pulses, while the repeatability due to mechanical movement and vibrations is low.
A fast reliable galvanometric shutter was planned and constructed to serve as a primary opening and closing system for structuring setup. Figure 3.6 illustrates

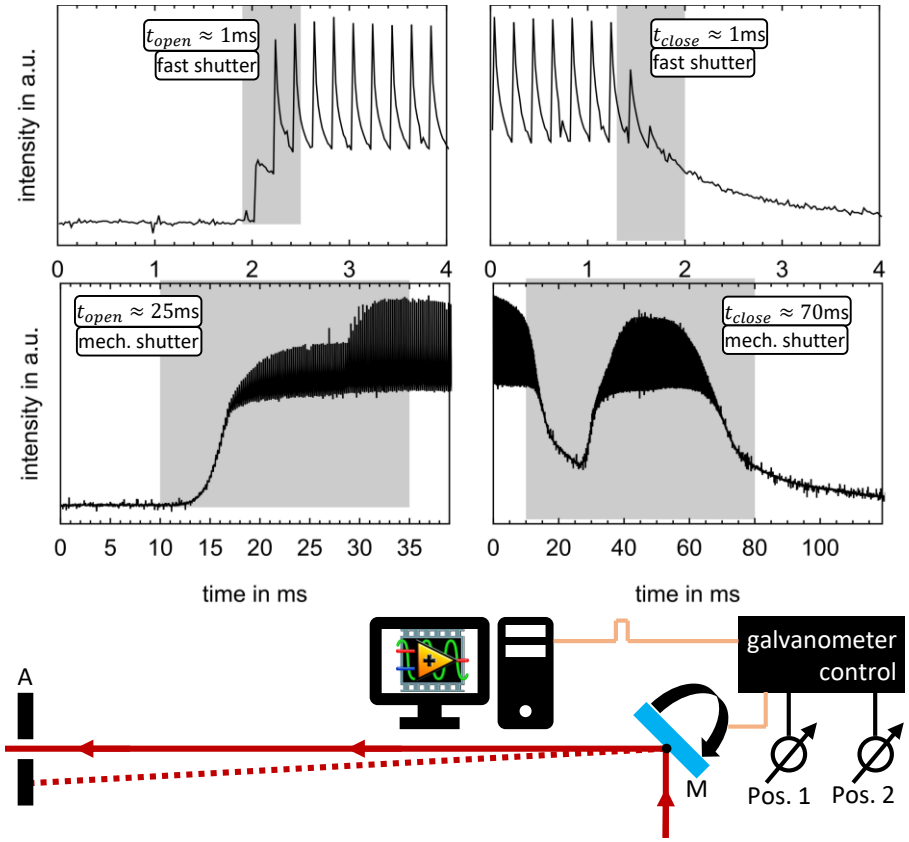

Figure 3.6.: The fast laser shutter developed within this work is shown as a schematic illustration (bottom row). Controlled by a computer programme, the galvanometric mirror switches between two angular positions that can be set with a potentiometer each. Placing an aperture in the optical path the system either forwards the laser pulses to the structuring setup or blocks the radiation. The opening ($\approx 25\,\mathrm{ms}$) and closing time ($\approx 70\,\mathrm{ms}$) by the conventional shutter available is too slow for the application within this work (middle row). In addition, this shutter does not open and close reliably. The opening and closing time measured with the fast galvanometric shutter (both $\approx 1\,\mathrm{ms}$), in contrast, shows almost single pulse resolution (top row).

the straightforward technical implementation. In addition, the measurement of opening and closing time is shown.
The incident radiation is deflected by a high reflective mirror mounted on a galvanometer type S10,[76] manufactured by *SCANLAB AG*. The mirror mount is designed in a way that the axis of rotation accords with the reflective front of the mirror. The galvanometer is controlled by an amplifier card, type SSV10 manufactured by the same supplier. The angular position of the mirror is controlled by an analog signal (voltage between −15 V and +15 V). For ease of application, a digital to analog converter was developed, that accepts a binary HIGH or LOW allocated to angular position 1 and 2 by the computer interface. The two absolute mirror positions can be controlled with a potentiometer each. Thus, the mirror switches the position of the laser beam on an aperture controlled by software between these two positions.
As shown in the top row of figure 3.6, the fast shutter demonstrates a reliable opening and closing time of approximately 1 ms maximum. Therefore, also very few laser pulses can be used in the experiment.
A valuable alternative to the mechanical rotation of the galvanometer mirror would be an additional Pockels cell. With this, even single pulses could be used in the experiment. However, within this work the financial and technical expense is not necessary.

3.2.4 Pulse length measurement

Measuring the length of ultra-short laser pulses present in the system is critical for the parameter studies and reproducibility therein. The pulse length can be characterised with an interferometric autocorrelation setup, existent in the laboratory. The laser pulse is split onto two separated paths and interfered with itself inside a non-linear crystal. The schematic setup is presented in figure 3.7. The incident pulsed radiation passes two iris apertures for alignment and is separated by a beam splitter (BS). This setup follows the working principle of a Michelson interferometer, generating two optical paths with manipulatable length difference using a motorised reflector (R) in one path. Two rays are overlapped inside a non-linear crystal (BBO). Therein, an intensity dependent frequency-doubled signal is generated, which is measured by a bandpass filtered camera. This signal is strongest, if the separated pulses arrive in the

[76] Handbuch SAM 10800 und 108003 S10 analog SSV10. SCANLAB AG. 2018-04-01 URL: http://www.scanlab.de/en/downloads/data-sheets.

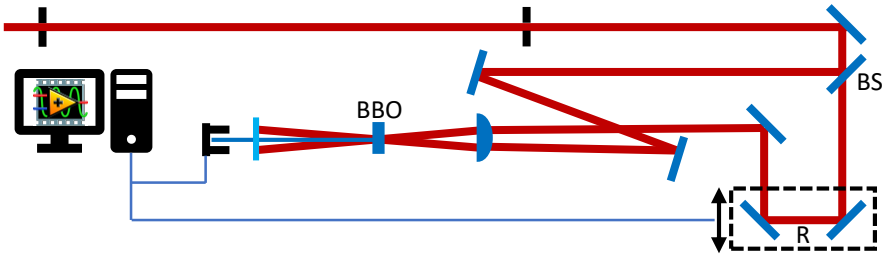

Figure 3.7.: Schematic illustration of the optical autocorrelation setup used within this work. The incident laser pulse is split into two paths using a beam splitter (BS) and focussed into a nonlinear crystal (BBO). Within the BBO an intensity dependent signal is generated. Changing the length of one path with a motorised retro reflector (R) an autocorrelation trace is obtained. Thereby, the length and temporal shape of the laser pulse is obtained.

crystal simultaneously. This signal scales with $|I(t)|^2$ for the generated harmonic of second order.[77] By moving the motorised retro reflector over this position, the intensity autocorrelation signal as a function of the time delay is generated.
For an ultra-short pulse length in comparison to the temporal detector resolution it writes[27,28]

$$I(\tau) = \int_{-\infty}^{+\infty} \left|(E(t) - E(t-\tau))^2\right|^2 dt. \tag{3.2}$$

Figure 3.8 shows the autocorrelation trace measured with the system described above as a function of delay in fs. The delay stage is moved stepwise in increments of 6.6 fs here. The autocorrelation trace obtained is considered Gaussian in good agreement with a model of the form

$$I_{\mathrm{AC}}(t) \propto \exp\left[2\ln(2)\frac{t^2}{\Delta t_{\mathrm{AC}}^2}\right] \tag{3.3}$$

[77] R. Boyd. Nonlinear Optics. 3rd ed. Academic Press, 2008. DOI: 10.1016/B978-0-12-369470-6.00011-3.

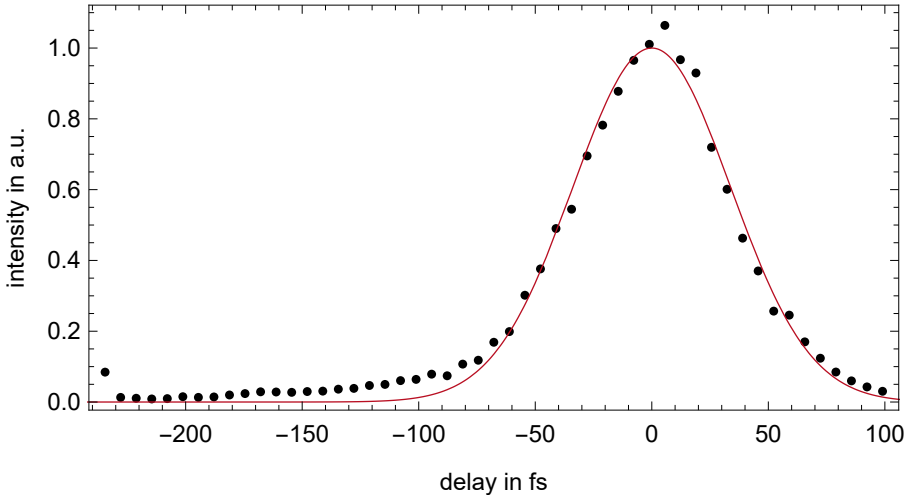

Figure 3.8.: Autocorrelation trace of the laser pulses used within this work. The measurement shows a Gaussian temporal intensity distribution (black). The according real pulse length (FWHM) is 56 fs obtained from the regression curve shown (red). Please note, that the measured pulse length is longer by a factor of $\sqrt{2}$ compared to the real pulse length.

with FWHM width Δt_{AC} measured by the autocorrelator. The real pulse length Δt is shorter by a factor of $\sqrt{2}$. Here, a value of $\Delta t_{\mathrm{AC}} = 80\,\mathrm{fs}$ and $\Delta t = 56\,\mathrm{fs}$ is obtained. Throughout this work, the pulse length is kept constant.

3.2.5 Beam profile measurement

The spatial intensity distribution of the laser field is dictating the shape and size of the surface structure. Characterisation of the beam profile along the optical path in the system is important. Within this work, collimated as well as focussed radiation is to be measured covering diameters from 10 µm to 10 mm and thereby several orders of magnitude in intensity. Typically, *complementary metal-oxide semiconductor* (CMOS) or *charge-coupled devices* (CCD) cameras are used to collect the position-resolved light intensity.

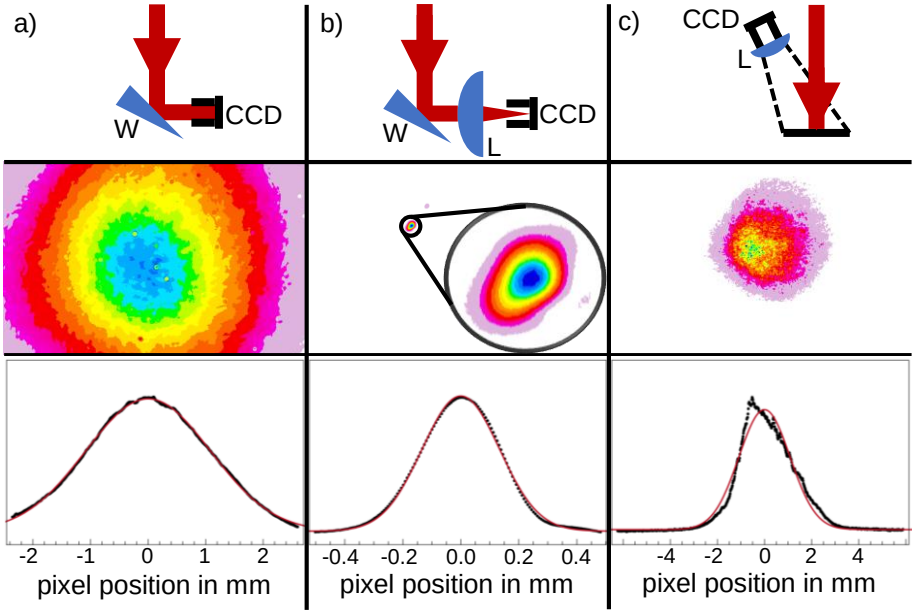

Figure 3.9.: Three beam profile measurement systems a) - c) used within this thesis. The schematic setup for the three techniques is illustrated (top row). For case a) a small fraction of light is directed directly onto the CCD sensor using an optical wedge. For b) an additional lens is used to investigate the beam profile in focus. An indirect approach is used with c) where the laser is blocked by a screen and the scattered light collected by the camera with an objective. For the last case, no wedge is used but an additional pixel position calibration is necessary. Images of the laser beam acquired for the three cases (middle row). With the averaged horizontal pixel intensities (bottom row) the beam radius w_S on camera sensor can be approximated.

Employing sensitive imaging devices to measure high-intense laser pulses requires particular caution to prevent damage to the camera.[78] The three setups used here are illustrated in the top row of figure 3.9.

For direct collimated a) and focussed illumination b), a portion of the main beam is separated with an optical glass wedge (W). Thus, front and back surface reflection are segregated. With two parallel surfaces, interference artefacts can occur on the camera sensor (CCD). Imaging a scattering screen c) through a camera objective (L), the radiation can be directly directed on the screen. With the last setup an additional calibration has to be performed, transferring the image pixels to a position value on the screen.

For all three setups a global-shutter CMOS camera, model UI-1220LE-M-GL[79] manufactured by *IDS Imaging Development Systems GmbH* is used. This camera offers a resolution of 752 × 480 pixels with a size of 6 µm each. The active region of the sensor accounts to 4.152 mm × 2.880 mm with a diagonal of 5.035 mm.

With a developed dedicated *LabVIEW*™ computer programme the camera settings can be controlled and the width and homogeneity of the laser beam is obtained. Within the software the central position of the laser beam is identified by averaging pixel columns and rows separately.

Following, the resulting horizontal lateral intensity profile is approximated with a model of the form

$$I(x) = I_0 e^{-2\frac{(x-x0)^2}{w_s^2}} - I_{\mathrm{BG}}. \tag{3.4}$$

In accordance with section 2.1, I_0 is the intensity at centre x_0 of the beam. The subtracted background intensity is denoted as I_{BG} and the $1/e^2$ beam diameter at the position of camera sensor as w_s.

The horizontal averaged intensity distribution is also shown in figure 3.9 (bottom row) with the corresponding image of the beam for the three measurement methods (a) to (c) (middle row).

[78] B. Schwarz et al. *Opt. Eng.* **56**, 034108, 2017.

[79] UI-1220LE-M-GL (AB.0010.1.25600.23). IDS Imaging Development Systems GmbH. URL: https://de.ids-imaging.com/IDS/datasheet_pdf.php?sku=AB.0010.1.25600.23 (accessed 01 April 2018).

3.2.6 Spatial frequency filter

As presented in section 3.2.5, the lateral intensity profile of the laser pulses leaving the amplifier is not purely Gaussian (TEM_{00}). In particular, for employing a rectangular beam profile with a diffractive optical element, as described in section 3.2.8, an intensity profile as homogeneous as possible is necessary. Attempts for a complete realignment of the oscillator and amplifier did not improve the beam profile.

For this reason, a spatial frequency filter was developed and set up together with *L. D. Geulig* in the scope of her Bachelor thesis.[80] The basic working principle of a spatial frequency filter a) together with the technical implementation b) is shown in figure 3.10.

Within a Kepler telescope (L1, L2) an aperture (A) is positioned at the position of minimal beam waist. The diameter of the aperture is chosen in such a way that a Gaussian beam (TEM_{00}) can pass the pinhole, while higher order modes are rejected.[81] Here an aperture diameter of $d = f\lambda/w_0$ is chosen, transmitting 99,3% of the total beam energy in the Gaussian mode, while blocking spatial wavelengths smaller than $2w_0$.[82]

Especially with high-intense femtosecond laser pulses the geometry and damage threshold of the aperture material is critical. In addition, plasma formation in the focus needs to be suppressed. Thus, for a technical implementation a tungsten aperture is positioned inside an evacuated tube that is connected to a vacuum system. Thereby, the number of particles in the focal region is reduced. The tube is sealed by two anti-reflection coated windows (W) on O-ring gaskets.

The aperture is made from tungsten, for which a damage threshold of $0.5\,\mathrm{J cm^{-2}}$ when applying a pulse length of 120 fs is reported.[83] The pinhole is held in an aluminium ring that serves as a sealing ring at the same time, as shown in the inset of figure 3.10.

The Kepler telescope consists of a $f_1 = 750\,\mathrm{mm}$ (L1) and a $f_2 = 500\,\mathrm{mm}$ (L2) planoconvex anti-reflection coated lens. Alignment of the telescope itself and

[80] L. D. Geulig. Diffraktive optische Strahlformung zur homogenen Strukturierung von Oberflächen mittels ultrakurzer Laserpulse. Bachelor Thesis. Technische Universität Darmstadt, 2018.

[81] P. M. Celliers et al. *Appl. Opt.* **37**, 2371, 1998.

[82] Technical Note: Spatial Filters. Newport Corporation. URL: https://www.newport.com/n/spatial-filters (accessed 01 April 2018).

[83] H. Zhang et al. *Phys. Rev. B* **94**, 224103, 2016.

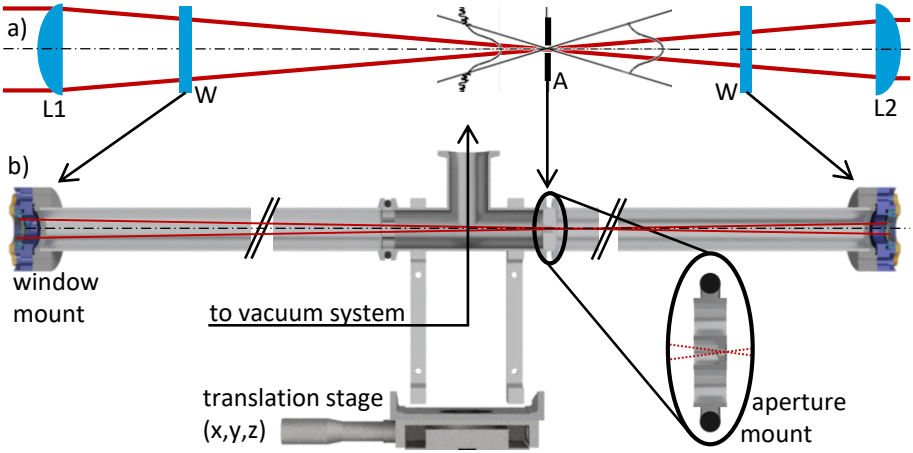

Figure 3.10.: Illustration of the spatial frequency filter designed and constructed within this work. The basic working principle of the aperture (A) blocking higher modes inside the focus of a Kepler telescope (L1, L2) is illustrated a). The technical implementation has a total length of $800\,\mathrm{mm}$ and consists of a $28\,\mathrm{mm}$ outer diameter tube made from stainless steel b). The tube is connected to a vacuum system (pump, valves, manometers) and O-Ring gasket sealed by two antireflection coated windows (W). For ease of alignment, the system as a whole is mounted on a x,y,z-translation stage. The tungsten aperture (A) is fixed to a precise aluminium ring. The spatial frequency filter was developed together with *L. D. Geulig* in the scope of her Bachelor thesis (ref. [80]).

in relation to the position of aperture is critical. Thus, the lenses are mounted independently from the evacuated aperture. The tube is fixed to a translation stage with three linear degrees of freedom.

First, the telescope is adjusted to generate an undisturbed collimated beam. Due to the focal length choice of $f_2/f_1 = 2/3$, the incident beam width is intentionally reduced by that factor. After adjustment, the aperture can be positioned in such a way that it lies in the focal plane and produces a concentric beam profile.

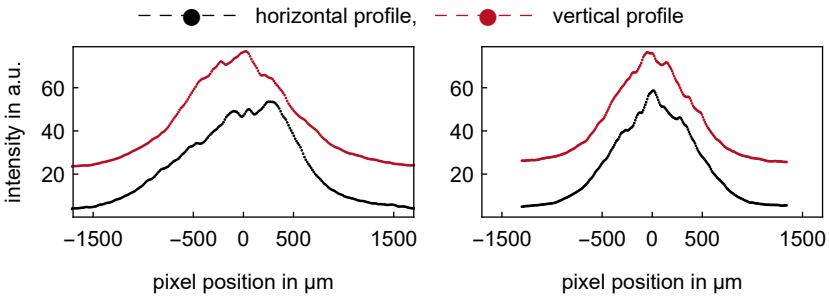

Figure 3.11.: Beam profile without (left) and with spatial frequency filter deployed (right). The horizontal (black) and vertical (red) averaged intensity distribution is shown. Using the filter, a homogeneous profile is observed. Please note, that fluctuations around the maximum are due to the scattering screen of the beam profiling camera.

Exemplary, figure 3.11 shows the raw intensity profile after the amplifier (left) in comparison to the profile after spatial filter (right) with a 230 µm tungsten aperture of 10 µm thickness. An average laser power of 100 mW was employed. Using the spatial frequency filter, the beam profile shows an increased symmetry and homogeneity.

3.2.7 Surface scanning setup

The surface scanning setup (compare to figure 3.2) is intended to generate surface structures over a bigger region than the laser focus. For this purpose a

fast two-dimensional galvanometric mirror scanner is developed together with *R. Leonhardt* in the framework of his Bachelor thesis.[84]
The schematic setup is depicted in a three-dimensional illustration in figure 3.12.
Two mirror galvanometers, type S10,[76] manufactured by *SCANLAB AG* are equipped with high-reflective coated mirrors. A reduced mass for the scanning mirrors is desirable, to gain an optimised dynamic of the system. The first mirror measures 14 mm × 18 mm, the second mirror 40 mm × 25 mm (length×width). The second surface is larger, to account for deflection by the first mirror.
The axis of rotation of both mirrors is perpendicular to each other and to the target surface. Before the deflection mirrors, a motorised focussing lens is positioned. As a first approximation for small deflection angles, the laser focus is therefore positioned onto the surface in a Cartesian coordinate system, as illustrated in figure 3.12. The angular position θ_x of the second mirror defines the x-coordinate and ϕ_y of the first mirror the y-coordinate. The z-coordinate is identical to the position z of the focussing lens.
As with the fast shutter in section 3.2.3, the Galvanometer position for both mirrors is controlled by two amplifier cards type SSV10,[76] manufactured by *SCANLAB AG*. An analogue input signal (U_x, U_y) between −15 V and +15 V is thereby translated to an angular position $\theta_x(U_x)$, $\phi_y\left(U_y\right)$.
Figure 3.13 shows the linear angular response to the voltage signal for both galvanometric mirrors. From this, the response function for a given distance of 29 mm between the two mirrors is found to be[84]

$$\theta_x(U_x) \propto 2.32(7)^\circ \times \frac{U_x}{\mathrm{V}} \quad \text{and} \quad \phi_y\left(U_y\right) \propto 2.27(6)^\circ \times \frac{U_y}{\mathrm{V}}. \tag{3.5}$$

So far, only the angular deflection is considered. To calculate a position value (x, y) on the surface from a given $(\theta_x(U_x), \phi_y\left(U_y\right))$, the absolute distance d from the second mirror to the surface needs to be considered[84]

$$(x, y) = \left(\tan\left(\theta_x(U_x)\right)(d + 29\,\mathrm{mm}), \tan\left(\phi_y\left(U_y\right)\right)(29\,\mathrm{mm})\right). \tag{3.6}$$

The distance d is determined, in particular, by the focal length f of the lens employed.

[84] R. Leonhardt. Aufbau und Charakterisierung eines zweidimensionalen Galvanometersystems. Bachelor Thesis. Technische Universität Darmstadt, 2016.

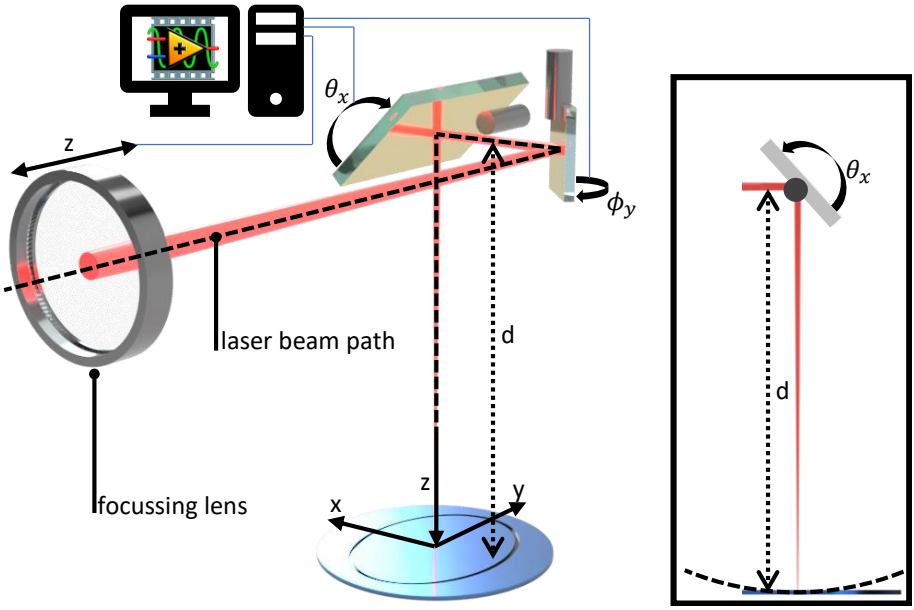

Figure 3.12.: Schematic setup of the galvanometric xy-scanner with adaptable optic developed within this work. The laser enters the system through a linearly motorised focussing lens. The optical path over the two galvanometric mirrors is indicated by the dashed line together with the working coordinate system on the sample surface. The first mirror deviates the beam by an angle ϕ_y, the second mirror by an angle θ_x. Thereby, the laser focus can be moved fast and precise over the silicon surface. Without moving the focussing lens a deviation from a focal plane is shown in the inset. A constant angular movement of the mirror does not contribute equally to the position on the surface due to the distance between the two galavanometer axes, as indicated by the ellipse on the silicon wafer. The whole system is controlled by a *LabVIEW™* programme and was developed together with *R. Leonhardt* in the scope of his Bachelor thesis (ref. [84]).

As indicated in the inset of figure 3.12, the laser focus is deflected onto an elliptical shell. The deviation from a focal plane is shown in the inset of figure 3.12. Points of constant deviation constitute an ellipse, as indicated by contour lines. Due to the difference in distance to the surface between the two mirrors, the deviation differs in x and y, as illustrated by the ellipse on the silicon surface. The $f = 250\,\mathrm{mm}$ planoconvex lens, typically used, shows a Rayleigh length of approximately 10 mm. For the structuring process of targets, typically with structured surfaces $< 1\,\mathrm{mm} \times 1\,\mathrm{mm}$ in size, the deviation is negligible. In particular, this means that no movement of the focussing lens is necessary for normal operation.

For control of the surface scanning system an extensive *LabVIEW*™ computer programme is developed. To simplify the generation of movement patterns an interface was programmed that allows the use of G programming language (G-code or RS-274).[85] This standardised format allows the simple and straightforward implementation of complex movement patterns for the generation of customisable surface structures. Further information about the implementation can be found in ref. [84].

The optimisation of surface scanning techniques achieved within this work together with *T. Ebert* (ref. [32]) is depicted in figure 3.14 (a-c). With a continuous pattern it is not necessary to use the laser shutter and a consistent movement of the laser focus over the silicon surface is possible. The spot is thereby moved line by line with a distance Δd between the lines. This distance is optimised for the focal dimensions employed. A straightforward approach is the movement in a zig-zag design as shown in (a) with a changing distance between the lines. Better results can be obtained by moving in parallel lines with a constant Δd and overshooting by a distance o with a rapid move of higher velocity (b). Rotating by an angle $\Delta\alpha$ and rescanning the surface can increase the surface homogeneity as illustrated in (c).

Summarising, the galvanometric mirror system for surface scanning is a powerful addition to the structuring setup and used for the fabrication of a huge number of targets in part II. Following, a single exposure setup is demonstrated, that is intended to generate structures without moving the laser focus.

[85] *Interchangeable Variable Block Data Format for Positioning, Contouring, and Contouring/-Positioning Numerically Controlled Machines.* Standard 2001 Eye Street, NW, Washington, D.C.: Electronic Industries Association., 1979.

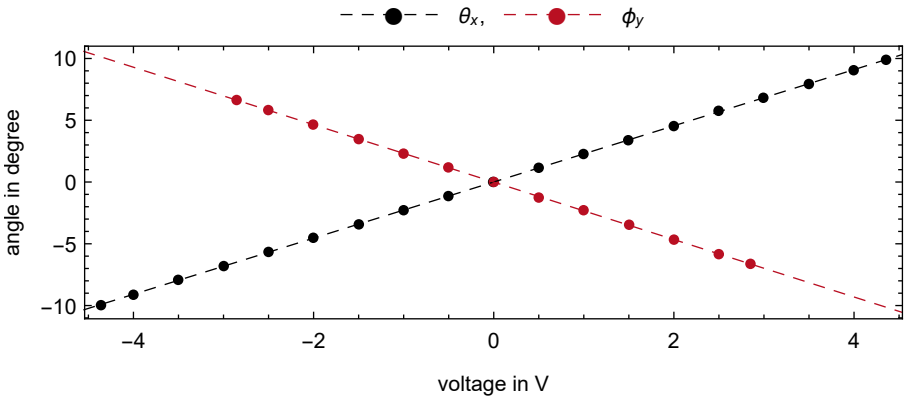

Figure 3.13.: Voltage to angle calibration of the galvanometric scanner system developed within this work. The measurement of angle and applied voltage shows a highly linear dependency for the deflection angles θ_x (black) and ϕ_y (red). The according linear regression to the data points is shown (dashed lines). With this the calibration functions are found. Adapted from ref. [84] (figure 7) with kind permission from *R. Leonhardt*.

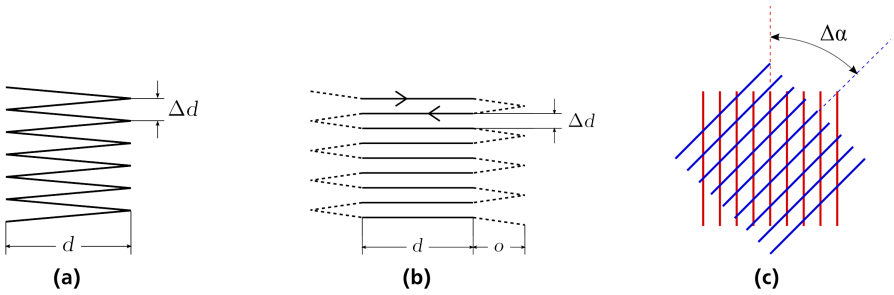

Figure 3.14.: Different scanning techniques for the structuring process using the galvanometric mirror system. A continuous movement trajectory without using the laser shutter is favourable. Straightforward is the implementation of a zig-zag line (a) even so the line distance Δd is changing along the path. Better results are obtained with parallel movement of the laser focus with a rapid overshoot (b). Rotating the scan pattern and restructuring can increase the surface homogeneity (c). Reprinted version from ref. [32] (figure 3.8) with kind permission from *T. Ebert*.

3.2.8 Single exposure setup

The single exposure setup (compare to 3.2) is faster compared to the scanning xy alternative described in the previous section. This system is solely intended to generate small structured regions without moving the laser over the surface. The outer dimension of the structured area is defined by the focus dimensions. The intensity distribution in focus can be custom shaped, employing a diffractive optical element or similar techniques. The general setup, developed within this work, is illustrated in figure 3.15.
A variable beam expander type 87-564,[86] manufactured by *Edmund Optics Ltd.* is used to precisely tune the beam diameter. It offers a continuously variable magnification of $1x$ to $2x$, transforming a collimated input beam to a collimated output beam. The expander can be used to magnify or demagnify, depending on the mounting direction in relation to the input beam. After a folding mirror, the laser radiation passes the beam shaping and focussing system. It consists of a beam shaper lens, type GTH-3.6-1.75, manufactured by *TOPAG Lasertechnik GmbH* and a planoconvex lens. The beam shaper lens transforms a Gaussian (TEM_{00}) input beam into a square top-hat profile at the focus position of the lens. Thereby an input beam diameter of (3.6 ± 0.15)mm ($1/e^2$) is required to produce a square spot with a homogeneity of ±5% relative to average intensity within the profile. The size of top-hat is approximately $5x$ to $10x$ of the diffraction limited Gaussian spot ($1/e^2$).
A proof of principle for the beam shaper lens is shown in figure 3.15. Utilising a helium-neon laser with a concentric and homogeneous intensity profile, the beam expander is used to generate the beam width required by the top-hat lens. The resulting focus profile after the beam shaper with a $f = 250\,\text{mm}$ planoconvex lens is shown together with the input profile. The resulting top-hat shows a width of 400 µm. For comparison, the expected diffraction limited Gaussian spot size is 70 µm for the lens used, in good agreement with the specification of the beam shaper.
The top-hat profile in focus with the titanium:sapphire laser (section 3.2.1) using the same expander-shaper-lens combination, depicted in figure 3.16, shows a comparable width of 400 µm and a non-uniform horizontal intensity profile. For this image, the spatial frequency filter was not used, deliberately.

[86] Techspec: variable beam expander instructions. Edmund Optics Ltd. URL: https://www.edmundoptics.de/document/download/395858 (accessed 01 April 2018).

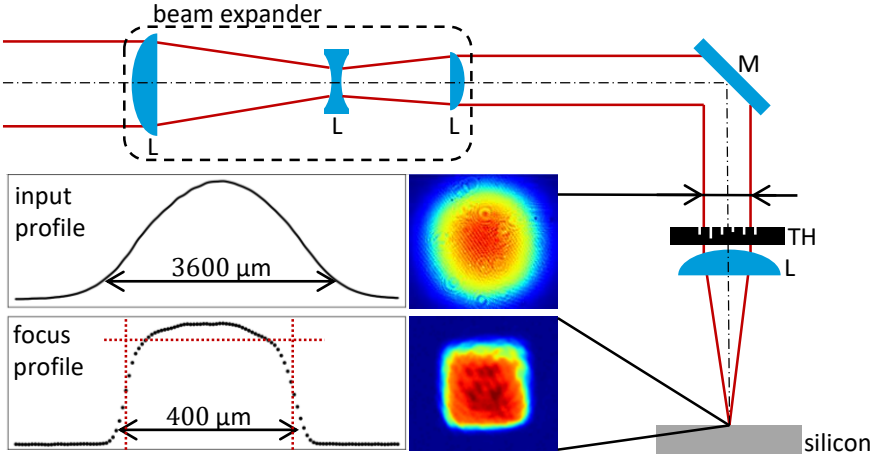

Figure 3.15.: Schematic illustration of the single exposure structuring setup developed within this work. Again, the radiation is focussed onto the silicon surface using a planoconvex lens. With a diffractive beamshaper (TH) a Gaussian distributed input beam is transferred to a top-hat intensity profile in focus. Therefore, the input beam has to be exactly $3.6\,\mathrm{mm}$ in diameter. This is achieved by introducing an inverted variable magnification beam expander into the optical path (consisting of three lenses with variable distances in between). For a proof of principle, the highly circular beam of a helium neon laser was used.

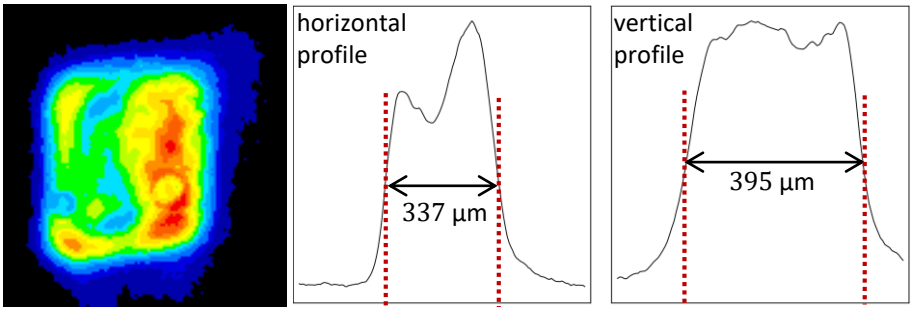

Figure 3.16.: The top-hat profile of the single exposure setup with the titanium:sapphire laser system shows a disturbed horizontal transverse section. In contrast, the vertical profile agrees with achieved distribution and width ($\approx 400\,\mu\mathrm{m}$) using the helium neon laser (figure 3.15). Deliberately, this image was taken without using the spatial frequency filter.

3.3 Processing chambers

As described in section 3.1, the processing chamber is intended to work with different media in solid, liquid and gaseous states. For this purpose, a basic chamber setup was developed with add-ons for the different ambient media. The development is supported by *T. Ebert* in the scope of her Master thesis.[32] For all cases, the laser beam enters the chamber through the top (z direction). The sample surface is oriented normally to the incident radiation (coplanar with xy plane). The silicon substrate is typically 7 mm × 7 mm with a centre thickness of 25 µm and attached to an aluminium pin stub specimen mount with a diameter of 12.7 mm (a standard for electron microscopes) for easier handling. Beyond that, substrates with dimensions of up to 50.8 mm in diameter can be used in the chambers.
The three setups for structuring in air, fluids and gases are shown in figure 3.17. For the structuring process in air no additions are necessary. The chamber topside is open. For liquid processing media, the top is also open but contains a capacitor to measure the fluid level. This sensor is described in more detail in section 3.3.1. The target chamber for structuring in gaseous atmospheres is more complex. It is sealed by an anti-reflection coated window and connected to a gas supply, vacuum and filtering system, which is described in section 3.3.2. Even so the gases used within this work are non-toxic, the interaction with laser radiation of high intensities produces hazardous decomposition products. Therefore, the filtering system is required and the volume of the chamber is limited to an inevitable minimum.
The chamber is mounted on a motorised two-dimensional translation stage with a lateral repeatability of 2.5 µm. It consists of two linear stages type VT-80 62309x0, manufactured by *Physik Instrumente (PI) GmbH & Co. KG*. The position can be controlled via computer, using a *LabVIEW™* programme developed within this thesis. Thereby, the sample can be precisely positioned in relation to the laser focus and galvanometric scanning system.

3.3.1 Fluid level sensor

For repeatable conditions with the structuring setup for fluid processing media a reliable sensor for the fluid level is required. As indicated in figure 3.17, a parallel plate capacitor was developed to work with the chamber. From a capacity measurement with this device, a consistent fluid level can be realised.

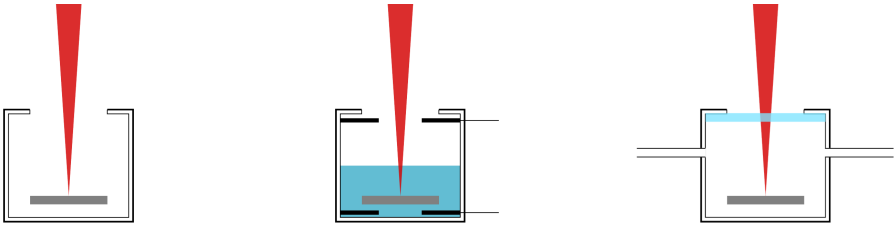

(a) Air. **(b)** Fluids. **(c)** Gases.

Figure 3.17.: Interaction chambers for structuring in air (a), fluids (b) and gases (c). The structuring setup in air allows for a simplified setup with open top (a). For the structuring in fluid media a filling level sensor is added (b). A sealed environment is necessary for the structuring process in gaseous ambient media (c). For the latter the chamber is connected to a gas supply, vacuum and filtering system. Reprinted version from ref. [32] (figure 3.3) with kind permission from *T. Ebert*.

In general, the capacitance with plate area A, distance d between plates and dielectric permittivity ϵ_R of the medium writes $C = \epsilon_0 \epsilon_R A/d$,[87] with vacuum permittivity ϵ_0. Here, the capacitor is filled with the fluid of height d_f, as well as a layer of air with height $d - d_f$. Therefore, the connected capacitance of fluid C_f and air C_a with $\epsilon_{\text{air}} \approx 1$ is[87]

$$\frac{1}{C} = \frac{1}{\epsilon_0 A}\left(\frac{d_f}{\epsilon_f} + d - d_f\right) \propto d_f\left(\frac{1}{\epsilon_f} - 1\right), \tag{3.7}$$

with a fixed distance d between plates. The total capacitance is increasing with rising fluid level d_f. Thereby, for a steady fluid level the capacitance should stay constant.
The capacitance is measured with an *Arduino Uno* microcontroller.[88] The software is an adapted version of the work done by J. Nethercott.[89]

[87] W. Demtröder. Experimentalphysik 2 (Elektrizität und Optik). Springer, 2013. DOI: 10.1007/978-3-642-29944-5.

[88] Arduino Uno. Arduino AG. URL: https://www.farnell.com/datasheets/1682209.pdf (accessed 01 April 2018).

[89] J. Nethercott Capacitance measurement with the Arduino Uno. URL: http://wordpress.codewrite.co.uk/pic/2014/01/21/cap-meter-with-arduino-uno/ (accessed 01 April 2018).

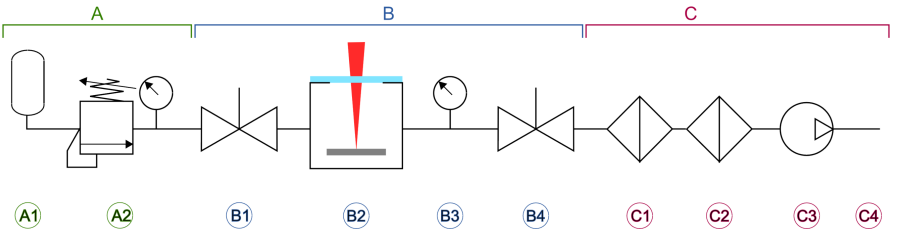

Figure 3.18.: Gas supply (A) and filter system (C) developed within this work and connected to the fabrication setup (C). A custom pressure sensor (B3) is directly connected to the interaction chamber (B2). The latter is sealed with two blocking valves (B1, B4). The system can be filled with gas using a container (A1) connected to a precise control manometer (A2). Toxic substances in the atmosphere are reduced using an activated carbon filter (C1) and ultra-small particle filter (C2). A vacuum pump (C3) evacuates the system through an external outlet (C4). Not shown is an additional fume hood around the setup. Reprinted version from ref. [32] (figure 3.6) with kind permission from *T. Ebert*.

3.3.2 Gas supply system

The gas supply system is intended to fill the target chamber with a precisely known amount of gas. Typically, sulphur hexafluoride (SF_6) is used. After the structuring process, the chamber is evacuated and the gas filtered to remove small amounts of toxic residues due to the interaction with the gas in the laser focus.

The system consists of three parts (A, B, C), illustrated in figure 3.18. Part A includes the gas container (A1) and a control manometer (A2) to fill the system with gas. Part B holds the target chamber (B2) in between two blocking valves (B1, B4) that are closed during structuring. The pressure inside the chamber is monitored with a pressure sensor (B3). Part C cleans the gas from toxic decomposition products after the structuring process with an activated carbon filter (C1) and an ultra-small particle filter (C2). The system is connected to a vacuum pump (C3) and passed through an external outlet (C4). In addition, a fume hood is placed around the setup to prevent inhalation. The whole system is designed to work below ambient pressure.

The pressure sensor used, is based on a calibrated miniature variometer module type MS5803-01BA.[90] by *TE Connectivity Corporation* This sensor is fixed to a stainless steel tube and readout by an Arduino[88] with software developed within this work. It is resistant to the decomposition products of SF_6 and accurate to within ±2.5 mbar.

3.4 Characterisation

The visual evaluation of micro-structures with highly light absorbing properties is challenging. The high aspect ratio of needles in combination with a low back reflection is limiting the quality of optical techniques, in particular. Also, the process should not destroy the surface structure, as the targets are intended to be used in an experiment later.
In this section, the different approaches for the characterisation employed in this work are presented. This includes basic camera imaging, optical light microscopes, profiling microscopes and scanning electron microscopes. With higher technical effort, the image quality of the structures can be increased. At the same time, most of these techniques cannot be used without removing the sample from the processing setup.
During structuring, cameras with a macro lens are used to position the laser spot on the sample surface and see the progress of the structuring process. The images acquired are not suited to estimate height, separation and homogeneity of the silicon needles. Only the consistency between production of a number of samples can be assessed thereby.
With an optical microscope the bounding shape of the structured area can be checked with a higher magnification. Even so the underlying needle structure cannot be resolved. It is used mainly for preparation of the samples and attaching to the sample holder.
The three-dimensional optical profiling microscope type PLu neox,[91] manufactured by *Sensofar Metrology* used in the laboratory has a resolution that, in theory, is sufficient to view the microstructures. Here, the confocal measuring mode is used, as it shows the best results.

[90] MS5803-01BA Miniature Variometer Module. TE Connectivity Corporation. URL: http://www.te.com/deu-de/product-CAT-BLPS0038.html?q=MS5803-01BA&source=header (accessed 01 April 2018).

[91] Sensofar PLu neox. Sensofar Metrology. URL: https://www.sensofar.com/metrology/ (accessed 01 April 2018).

Thereby, the field of view by the objective lens is illuminated uniformly. The backscattered light is then focussed on a small aperture which links a xy-point on the sample to a position on the detector. Points outside the focal plane are diminished when passing the aperture. Moving the sample along the optical axis an intensity of xy-points is recorded. From z positions with the highest intensity a three-dimensional model can be computed.[87,92]

A three-dimensional reconstruction for silicon needles with high aspect ratio is not possible employing the optical profiling microscope. The amount of backscattered light from the cone walls is orders of magnitude below that of tips and valleys. But, in contrast to traditional optical microscopy, as described above, the separation and needle height can be determined.

A complete characterisation of the surface structure is possible, using a scanning electron microscope. Within this work a model 1200 B *LEITZ REM* was set up in the *Target & Detektorlabor* laboratory. This model relies on a heated tungsten filament as an electron source. Electrons are accelerated by high voltage. In addition, a higher resolution scanning electron microscope XL30 FEG by *Philips* was accessible in the department of material science of the *Technische Universität Darmstadt*. This model employs a field emission type electron gun with a higher brightness and reduced source size in comparison to the thermal field emitter used in the laboratory model and thereby enables a higher resolution.

Electrons emitted by the source in both models are accelerated by a high voltage and focussed onto the sample. Along the electron path the virtual source size is further demagnified and aberrations are reduced by a combination of coils. The setup, including the sample, is evacuated within a vacuum chamber. The sample is mounted to a precise translation and rotation stage and needs to be conducting for better contrast. In general, the electron signal from the interaction of the sample surface layer with the focussed electron beam is detected with a scintillator and photomultiplier combination. Here, mostly the secondary electron (SE) signal is used. A deeper insight in the working principle of a scanning electron microscope, which would go beyond the scope of this work, can be found in the book of *Hawkes and Spence*.[93]

A comparison between the optical profiling microscope (PLu neox) and a scanning electron microscope (Philips XL30 FEG) for the same surface sample is

[92] A. Fine et al. *Trends Neurosci.* **11**, 346–351, 1988.

[93] P. W. Hawkes, J. C. H. Spence, and R. Reichelt. Scanning Electron Microscopy. Springer, 2007. 133–272 DOI: 10.1007/978-0-387-49762-4_3.

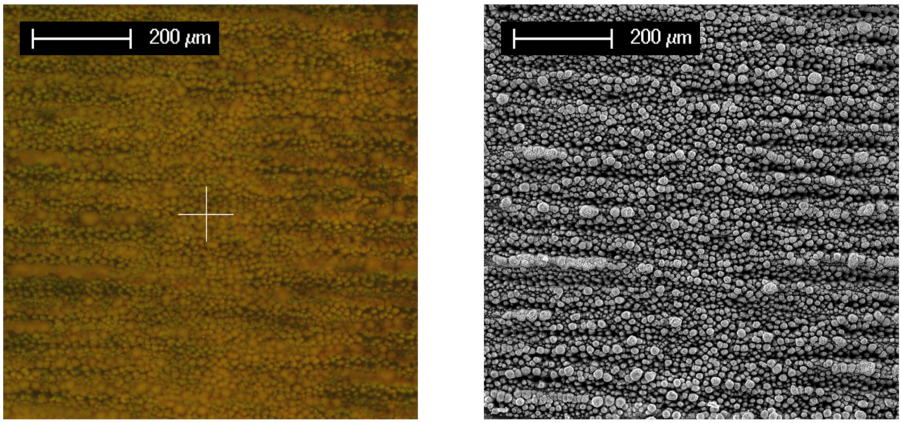

Figure 3.19.: A comparison of the same surface sample between optical profiling microscopy (PLu neox, left) and scanning electron microscopy (Philips XL30 FEG, right). Conventional optical microscopy cannot resolve steep walls and valley, which trap the light. A micrograph with high contrast can be achieved deploying scanning electron microscopy. Reprinted version from ref. [32] (figure 5.2) with kind permission from *T. Ebert*.

shown in figure 3.19. The increased image quality by using the electron microscope is clear.
Additional attempts to reconstruct a three-dimensional model from a number of tilted scanning electron pictures using optical close-range photogrammetry and stereo imaging can be seen in the Master thesis of *Tina Ebert*[32] together with advanced techniques for the processing of images.

4 Influence of parameters

The shape, height and homogeneity of surface structures are influenced by a number of parameters. A great variety of structure types is possible. The production of surface structured samples with high homogeneity is therefore directly related to the choice of the right consistent and reproducible parameter set, employing the comprehensive processing setup presented in chapter 3.
Here, the influence of most important laser characteristics and processing substances to the surface structure are summarised. The key information and techniques gathered within this chapter are afterwards transferred to the production and characterisation of targets for a high power experimental campaign presented in part II of this thesis.
The characteristics of laser-induced micro-structured silicon surfaces presented within this work, follow the results of constructive and fruitful work in the laboratory together with my Master student *Tina Ebert*.[32]
First, the influence of ambient processing media on the general shape of the surface structure is presented. Following, the influence of pulse number and laser energy fluence to the height of structures is described. Thereby, the focus lies on micro-structures fabricated using a sulphur hexafluoride ambient. To finish, the influence of intensity distribution and surface scanning pattern to the homogeneity of the structure is illustrated.

4.1 General shape of the microstructure

General geometric appearance of the micro-structures is above all influenced by the processing medium applied. The ablation threshold of the solid, chemical reaction processes and transmission of laser energy to the silicon are dependent on the ambient employed. The following section can only give a trend for a narrow selection of media.
Figure 4.1 shows scanning electron microscope pictures of structures produced in air at atmospheric pressure (a-c), liquid isopropyl alcohol (d-f) and sulphur hexafluoride (SF_6) at a pressure of 800 mbar (g-i).

At comparable magnification ratios a top view (a, d, g), 45° tilted view (b, e, h) and side view (c, f, i) of the surface is captured. Silicon processed in air produces rounded blunt needles, covered with debris. The height of these structural features varies strongly around an average of 15 µm (see (c)). The mean spacing accounts to 10 µm (a). Small needles are nested within bigger bumps.
Applying liquid isopropyl alcohol to the laser process, geometric knolls evolve. They show a molten nano-structured surface and a separating rift of constant width. The base is not round but bevelled with a varying number of facets. An average height of approximately 5 µm with a mean lateral tip distance of 3 µm is visible.
Employing a gaseous sulphur hexafluoride atmosphere sharp needles with a high aspect ratio appear. The needle bases are strongly elliptical due to polarisation dependence of Fresnel-reflection.[94] The polarisation of the laser pulse is oriented parallel with respect to the smaller width of the needles. The absorption of p-polarised light on the needle walls is larger than that of s-polarised[71] in agreement with this observation. Concentric cones would be possible applying an elliptical polarisation in the experiment.
The surface structure shows a consistent height and separation of the needle tips. The mean spike height is approximately 10 µm with an average separation of 5 µm (horizontal in (g)) and 7 µm (vertical in (g)). Surface of the needle is slightly textured with rounded tips. From side view (i), the steep slope and thereby high aspect ratio of the needles is apparent. Here, the full cone angle is approximately 20°.
The choice of processing media offers a great variety of different shapes, subtexture and dimensions of laser-induced surface structures. Beyond that, the possible range of substrate materials opens up new vistas that go far beyond the scope of this work. The condensed results presented here are intended to generate the scientific and experimental basis for the production of target for the campaign described in part II of this thesis. In the experiment structured silicon targets employing a sulphur hexafluoride ambient medium during the structuring process are researched. The following sections focus on this small portion of the manufacturing capabilities. Additional information and approaches can be found in the thesis of *Tina Ebert*[32] and the extensive work of *Sheehy et al.*:[26]

[94] J. T. Zhu et al. *Appl. Surf. Sci.* **252**, 2752–2756, 2006.

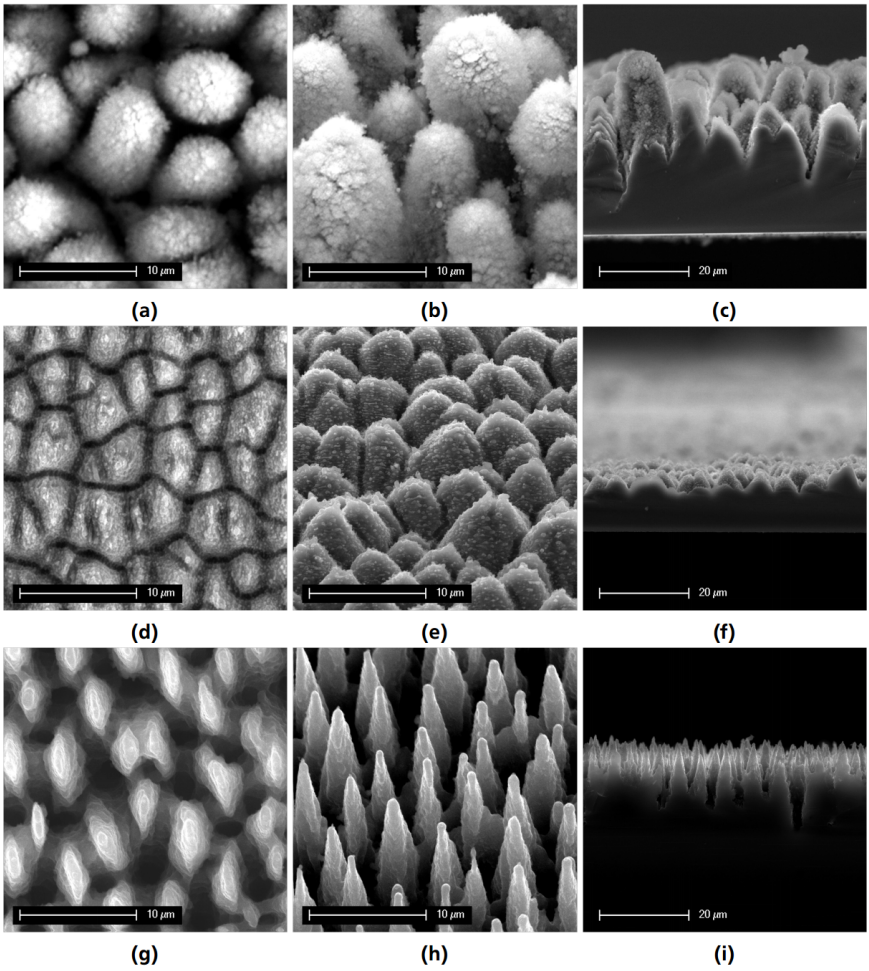

Figure 4.1.: The influence of three different ambient media on the microstructured surface is shown. Fabrication in air at atmospheric pressure creates blunt needles that are covered with decomposition products (a-c). Isopropyl alcohol leads to geometric knolls with a nanostructured surface (d-f). Structuring in gaseous sulphur hexafluoride creates sharp needles with a high aspect ratio (g-i). The first column (a, d, g) shows a top view. Micrographs of the sample tilted by $45°$ are shown in the second column (b, e, h). A side view is depicted in the third column (c, f, i). Reprinted version from ref. [32] (figure 4.3) with kind permission from *T. Ebert*.

4.2 Height and separation of silicon needles

For a given process substance, like sulphur hexafluoride used here, the height and separation of the silicon needles is determined by the laser parameters applied. Dominant is thereby the laser fluence $\mathscr{F} = {}^{E_P}/_{A}$ with pulse energy E_P and characteristic spot size A. Here, $\mathscr{F}$ is given in ${}^{\mathrm{kJ}}/_{\mathrm{m}^2}$. In addition, it is necessary to apply a sufficient number of pulses N_P per surface area to generate a fully developed structure. Using the surface scanning , N_P can be set by the choice of scanning velocity v with

$$N_P = f_R \cdot \frac{2 \cdot w_P}{v}, \tag{4.1}$$

with spot diameter $2 \cdot w_P$ and repetition rate $f_R = 5\,\mathrm{kHz}$ of the laser system.
Figure 4.2 shows the resulting needle height as a function of laser fluence (red) in comparison to the work of *Her et al.*[71] (black). Error bars show the standard deviation. Here, a scanning velocity of $v = 1\,{}^{\mathrm{mm}}/_{\mathrm{s}}$ and spot diameter of $2 \cdot w_P = 87\,\mu\mathrm{m}$ is chosen, resulting in a number of pulses of $N_P \approx 350$. The processing atmosphere is sulphur hexafluoride at an ambient pressure of 800 mbar. The employed fluence values between $4.0\,{}^{\mathrm{kJ}}/_{\mathrm{m}^2}$ and $9.2\,{}^{\mathrm{kJ}}/_{\mathrm{m}^2}$ show an average needle height, that agrees with the general trend of the literature values.[71] The dashed line represents a regression curve for the fluence ($\mathscr{F}$) dependency of the height h in the form

$$h(\mathscr{F}) \approx \left(4.(4) + 0.001(5) \cdot \exp\left[{}^{\mathscr{F}}/\left(\frac{\mathrm{kJ}}{\mathrm{m}^2}\right)\right]\right)\,\mu\mathrm{m} \tag{4.2}$$

to the data of *Her et. Al.*[71] With a coefficient of determination $R^2 \approx 0.99$, this relation eases the choice of parameters for a target needle height.
Figure 4.3 shows the average height of the needles produced with the developed processing setup (red) as a function of the mean separation between them. Error bars indicate the standard deviation of height and width. Here, the fixed relation between size h and distance d for a given processing medium becomes apparent. For comparison, again the results of *Her et al.*[71] (black) are shown and these agree with the structures produced here. The correlation of height h and separation distance d follows a power law dependency

$$h(d) \approx 0.1(8) \cdot d^{2.(4)}, \tag{4.3}$$

shown as dashed line in figure 4.3. With equation 4.2 and 4.3 the parameter choice for the production of targets in sulphur hexafluoride is dramatically simplified.

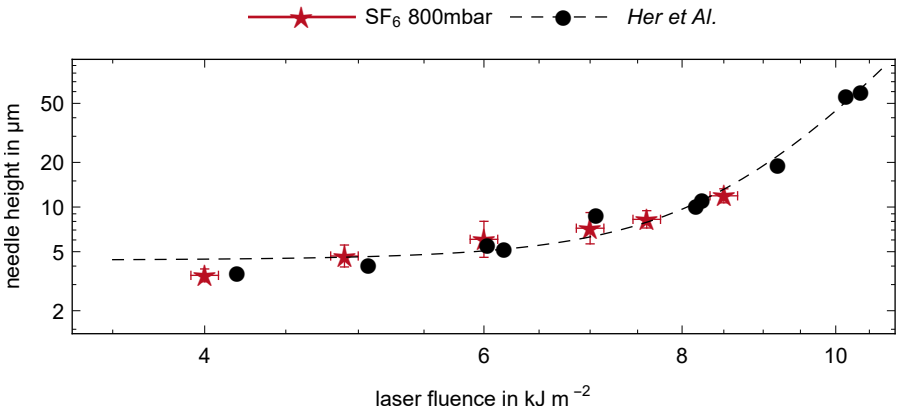

Figure 4.2.: The needle height in µm as a function of laser fluence in $^{kJ}/_{m^2}$ is shown. Data points obtained in this work (red) are shown in comparison to literature values from the work of *Her et al.*[71] (black) in good agreement with a regression curve (dashed). This model can be used to predict the obtainable needle height for a given parameter set. Error bars indicate the standard deviation.

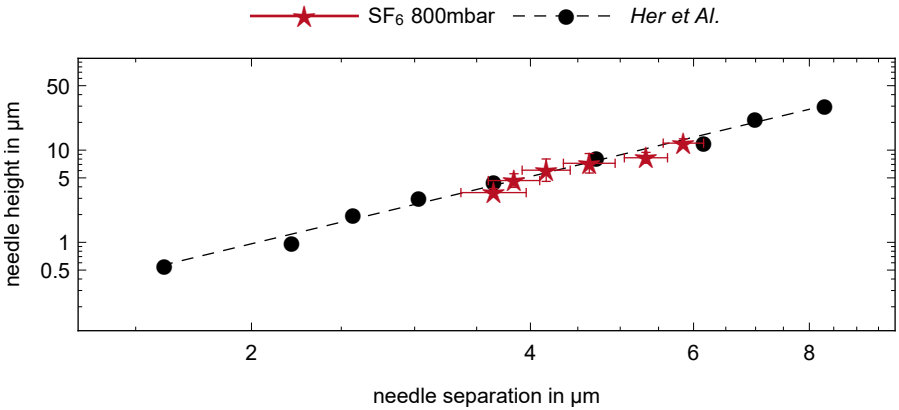

Figure 4.3.: The needle height in µm as a function of needle separation in µm is presented. Results of this work (red) are shown together with literature values from *Her et al.*[71] (black). Error bars indicate the standard deviation. A power law model shows a predictable ratio of needle height and separation (dashed).

Part II.

High power experimental campaign

5 Planning and preparation

The production and characterisation of microstructures with highly light absorbing properties has been briefly discussed in part I. To evaluate the impact of these structures to high power laser and plasma physics, a comprehensive experiment has been realised as part of this thesis at the *Central Laser Facility* located at the *STFC Rutherford Appleton Laboratory*, UK. *Target Area Petawatt* and the high power *Vulcan* laser system offer ideal conditions to explore the characteristics of novel and innovative targets. Here, we investigate the influence of the microstructured surfaces presented before on the laser energy absorbed into the target and transferred to electrons, ions and electromagnetic radiation.

This chapter is intended to accurately describe how the experiment is designed, prepared, operated and analysed in a non-committed way. A thorough discussion of the versatile and manifold data acquired will be presented in chapter 7. The following section gives a general overview of the extensive experimental setup. Following, the production of targets is presented. After that, the individual components and diagnostics and their alignment are discussed together with a brief description of how data is acquired, stored and processed with these diagnostics.

5.1 Quantities to be measured

To evaluate the influence of a structured target front to the intense interaction with a short laser pulse, the experimental setup is chosen to account for a complete as possible picture of the transfer of incident laser energy. This means in order to gain a substantive comparison of structured to flat targets a great many of different detection channels has to be established to monitor the central interaction. This includes properties of incident, reflected, transmitted and scattered laser light to obtain a measure for energy absorbed by the target. In addition, the excitation and degeneration of the target and therefore emitted high energetic particles and electromagnetic radiation from the target

front and back have to be monitored. These four fundamental measurands of the central interaction with the target are depicted in figure 5.1.
For a successful experiment, the following considerations have to be made.

1. **Laser system:** In order to concentrate on the effects of the surface structure to all detection channels, the incident laser pulse has to be optimised and monitored. Especially fluctuations in the temporal intensity profile and pre-pulses exceeding the plasma threshold have to be avoided by all means, in order to leave the surface structure unaltered.

2. **Reflected and scattered light:** The incident high energetic laser pulse impinges under an angle to surface normal onto the target. Thus, reflected light is not travelling back into the laser system (which would be problematic) but directed with a known orientation by the target angle. For this reflected light, not only the intensity of reflected light is important, but also the spatial intensity profile and wavelength distribution (e.g. higher harmonics, that give rise to the strength of the interaction and expansion of plasma). Scattered light is send out arbitrarily to the full covered angle of the target front surface. An absolute measurement of scattered light is necessary in order to calculate the amount of absorbed laser energy, but not feasible if other diagnostics need to be applied (like the measurement of reflected energy).

3. **High energetic electrons and ions:** Above a certain threshold of laser intensity on target the formation of plasma and interaction with the driving light field becomes important as a source for high energetic electrons and ions (compare to theoretical foundations, e.g. TNSA). Therefore the emission of electrons, protons and heavier ions from the target backside (and frontside) is visible. The prominent direction of emission is the target normal back side, target normal front side and incident laser axis. Here the spatial distribution, absolute number and energy distribution (spectrum) of electrons, protons and ions is of particular interest.

4. **Characteristic x-ray radiation:** The proceeding expansion of plasma and penetration of charged particles through the target is a source of secondary high energetic electromagnetic radiation emitted (e.g. x-ray and gamma radiation). Looking at characteristic lines in the spectrum the interaction strength can be determined.

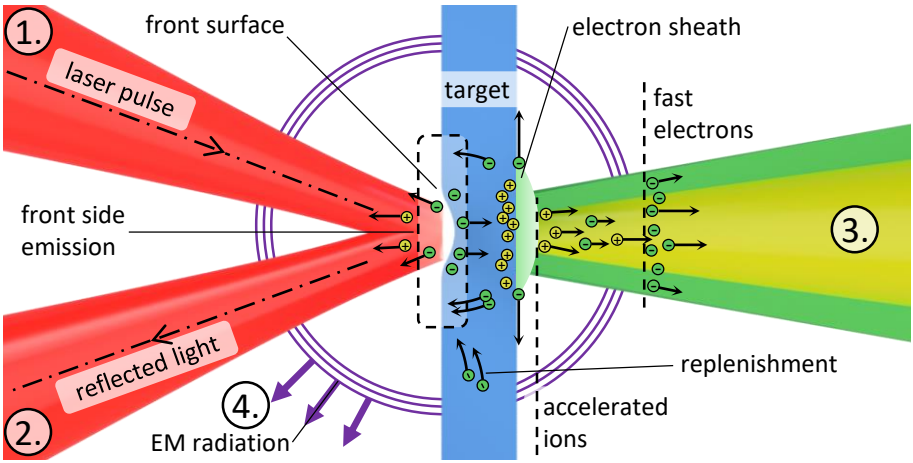

Figure 5.1.: Schematic illustration of a high-intense laser pulse interacting with a solid silicon target. To investigate the influence of a structured front surface to the interaction, a complete as possible picture needs to be recovered by the diagnostic setup. This includes the properties of the incident radiation from the laser system (1.) and the reflection and scattering from the target surface (2.). Ideally, the generation and acceleration of electrons and ions from front and backside is monitored (3.), as well as the emission of electromagnetic radiation over a broad spectral region and solid angle (4.). Within this work the basic acceleration mechanism for ions observed is called *target normal sheath acceleration* (TNSA). Electrons (-) are forced further into the solid target by different absorption mechanisms (see section 2.3.4). Fast electrons are emitted and an electron sheath is created on the target backside (and front side). Additionally, electrons replenish from the surrounding material. Consequently, strong electric and magnetic fields are generated throughout the target and ions (+) are accelerated away from the surfaces. Key for a successful experimental campaign is the proper layout of laser parameters, targets and diagnostics as demonstrated below.

As the different diagnostics are not capable to cover the full solid angle of the interaction, considerations have to be taken into account where to position the individual devices (in section 6 the experimental setup is covered in more detail). In addition to the fabrication of different target types and a brief description of the *Vulcan* Laser system, the following sections show a discussion of necessary laser parameters for structured targets and how to achieve them.

5.2 Production of structured targets

As described above, the main goal of the experiment is to investigate the influence of the microstructured surfaces presented in part I on fundamental quantities of the high-intense laser matter interaction.
Four main target types were fabricated and used in the experimental campaign including the laser-generated microstructures, following called needle structure. These targets are illustrated in figure 5.2.
As a structureless reference target solid silicon membranes with a thickness of 25 µm embedded into a thicker frame of 600 µm are used. The membranes with a quadratic shape of 6.3 mm by 6.3 mm are attached to aluminium posts for alignment and mounting inside the target chamber. The second target type with the needle structure on the front side are laser fabricated from the same membranes for continuity. The structured region is formed on a circular area with a diameter of 1.0 mm. The average needle height achieved is 15 µm with a remaining substrate thickness of approximately 10 µm. The target backside, facing away from the incident laser, is untouched and polished by the manufacturer.
Two additional structure types (groove and pillar) are produced by the target fabrication group of the *Central Laser Facility* using a technique called *deep reactive ion etching* (DRIE). The shape of the etched structure is defined by a mask which is applied to the surface before processing using a thin film of photoresist. Here, circular pillars with a diameter of 3 µm, center distance of 5 µm and a height of 15 µm on a 10 µm base are produced. In addition, grooves with a solid width of 2 µm and spacing of 3 µm are fabricated. Height and base thickness are identical to the pillar targets. The structured area covers a rectangular area of 500 µm by 500 µm. In comparison, the membrane of flat and needle targets covers an rectangular area of 3500 µm by 3500 µm.
The size and separation of all three structures (needle, pillar, groove) is chosen such that density is identical with a comparable feature size.

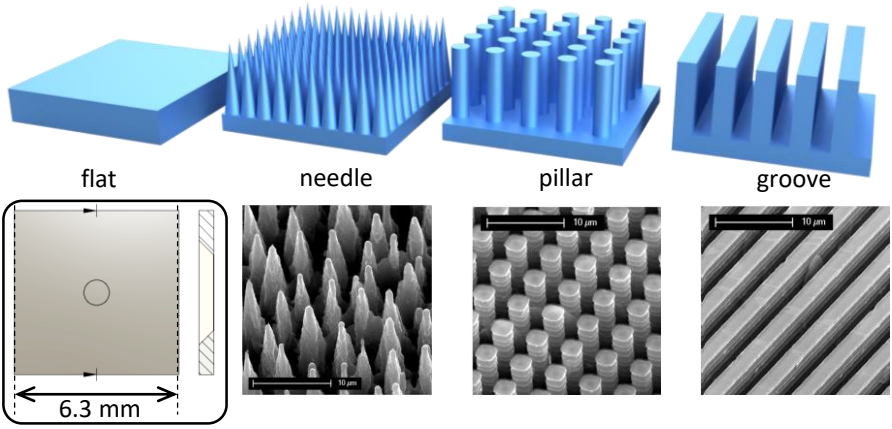

Figure 5.2.: The four main types of target structures fabricated for the experimental campaign. The top row shows a schematic illustration of the four target types, the bottom row electron micrographs of the structures. As a reference target silicon membranes with a central thickness of $25\,\mu\mathrm{m}$ embedded into a thicker frame of $600\,\mu\mathrm{m}$ are used (flat). Microstructures are added to a $1\,\mathrm{mm}$ diameter region onto a number of membranes (compare to the inset). Following, this structural shape is called needle in comparison to the groove and pillar targets illustrated on the right. These structures are fabricated by the target fabrication group of the *Central Laser Facility* using *deep reactive ion etching* (DRIE).

5.3 Laser contrast and intensity

The contrast of a laser system is the ratio of pre-pulse intensities to peak intensity of the main pulse. To observe the influence of a surface structure interacting with the highest intensity of the laser pulse, the temporal intensity contrast of the laser system is critical. A substantial flux of energy before the main pulse will dramatically alter or destroy the target structure and leaves a preheated and therefore completely different target type. It is necessary to avoid the generation and expansion of a pre-plasma before the peak of the pulse reaches the target. Following a brief description of the *Vulcan* laser system is given, before the laser contrast is identified and optimised.

5.3.1 The *Vulcan* laser system

The *Vulcan*[95] laser system is part of the *Central Laser Facility* (CLF) at the *STFC Rutherford Appleton Laboratory*, UK. It relies on the technique of *optical parametric chirped pulse amplification* (OPCPA). Within the main amplification stages it uses flash lamp pumped Nd:YAG lasers with a central wavelength of 1053 nm. Initially, a titanium:sapphire oscillator generates pulses with a length of 120 fs that are stretched to 4.5 ns. In a first pre-amplifier stage the pulses are intensified to approximately 10 mJ before being sent to the main amplification stages. After the final stage which uses ex-NOVA laser 208 amplifiers (rod amplifier and disc chain) the pulses have an energy of 650 J prior to compression.

Throughout the system, adaptive optics are used to optimise the wave-front quality. Additional spatial filters smooth out the beam by eliminating high frequency components. The exit beam has a diameter of 60 cm and is directed into *Target Area Petawatt* (TAP) where it is compressed by two diffraction gratings with a diameter of 94 cm to a length of roughly 1 ps. The final pulse energy delivered to the target chamber is approximately 450 J where it is focussed to a 10 µm diameter spot by an off-axis parabola. That is equivalent to peak intensities of $10^{21}\,\mathrm{W/cm^2}$ for the given spot size.

[95] I. Musgrave et al. *High Power Laser Sci. Eng.* **3**, e26, 2015.

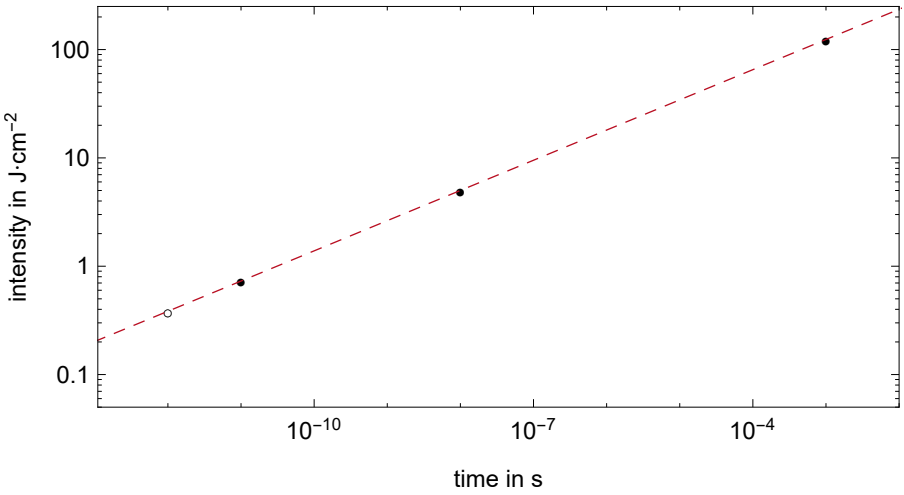

Figure 5.3.: Laser-induced damage threshold of silicon (LIDT) following the work of *Wang et al.*[96] (black). With a power law fit (red) the LIDT of silicon for a pulse length of 1 ps is derived (circle). This model only gives an upper limit for the threshold as for ultra-short laser pulses additional damage mechanisms are observed.

5.3.2 Laser contrast

From Ref. [96] the laser-induced damage thresholds (LIDT) of millisecond, nanosecond and picosecond pulse durations for mono-crystalline silicon is shown in figure 5.3. For a given pulse length of 1 ps the damage threshold for a pulse length of 1 ps is estimated by a power law fit to the data for 10 ps, 10 ns and 1 ms:

$$\mathrm{LIDT}(\tau_P) = e^{6.75}\tau_P^{0.28} \tag{5.1}$$

with pulse length τ_P (full width at half maximum). From that a damage threshold of $0.37\,\mathrm{J/cm^2}$ is derived.
Figure 5.4 shows a temporal intensity scan of the *Vulcan* petawatt laser system provided by the *Vulcan* staff. It was recorded in December 2015. Also shown is the laser intensity for a given best focus diameter ($2w_0$) of 5 µm (black) together with the estimated laser-induced damage threshold of silicon (yellow).

The maximum laser intensity accounts to $3 \cdot 10^{21}\,\mathrm{W/cm^2}$ with a maximum prepulse intensity of $1.3 \cdot 10^{14}\,\mathrm{W/cm^2}$. Even in the idealised picture shown here, this is two orders of magnitude above the damage threshold of silicon. The laser contrast accounts to $5 \cdot 10^{-8}$. This contrast needs to be increased by several orders of magnitudes in order to focus on the effects of an unaltered surface structure. The system designed for this purpose is presented in the following section and increases the contrast to the additional trace shown (red).

5.3.3 Double plasma mirrors setup

To increase the laser contrast on target plasma mirrors are used. A plasma mirror is an optical substrate with an anti-reflective coating to maximise transmission. This surface is placed close to the laser focus, such that the laser intensity reaches about $10^{15}\,\mathrm{W/cm^2}$ and above. Before a laser pulse arrives, the plasma mirror is reflecting approximately 0.3 %. When the intensity reaches the ionisation threshold of the anti-reflection coating at about $10^{12}\,\mathrm{W/cm^2}$ the reflectivity of the plasma mirror increases with the laser intensity until it reaches a plateau at intensities around $10^{15}\,\mathrm{W/cm^2}$.[97] The maximum reflectivity is typically around 70 %. Therefore, the laser contrast can be increased by up to three orders of magnitude by usage of a single plasma mirror. The calculation of the reflected laser intensity R after a single plasma mirror follows the model[97]

$$R(P_{\mathrm{in}}) = \begin{cases} 0.3\,\% & P_{\mathrm{in}} \leq 1 \cdot 10^{13}\,\mathrm{W/cm^2} \\ 0.3 \cdots 70\,\% & 1 \cdot 10^{13}\,\mathrm{W/cm^2} < P_{\mathrm{in}} < 5 \cdot 10^{14}\,\mathrm{W/cm^2}, \\ 70\,\% & P_{\mathrm{in}} \geq 5 \cdot 10^{14}\,\mathrm{W/cm^2} \end{cases} \tag{5.2}$$

with the incident intensity P_{in} is the intensity on the plasma mirror surface. The intermediate section follows a linear increase. The contrast can be further increased by additional plasma mirrors, as long as the peak intensity on the mirror surface is sufficient and the decrease in transmitted available laser energy is acceptable.
For this experiment a double plasma mirror setup is designed to increase the laser contrast by several orders of magnitude. The general path of the laser pulse over the two plasma mirrors to the target is depicted in figure 5.5.

[97] V. Bagnoud and F. Wagner. *High Power Laser Sci. Eng.* **4**, e39, 2016.

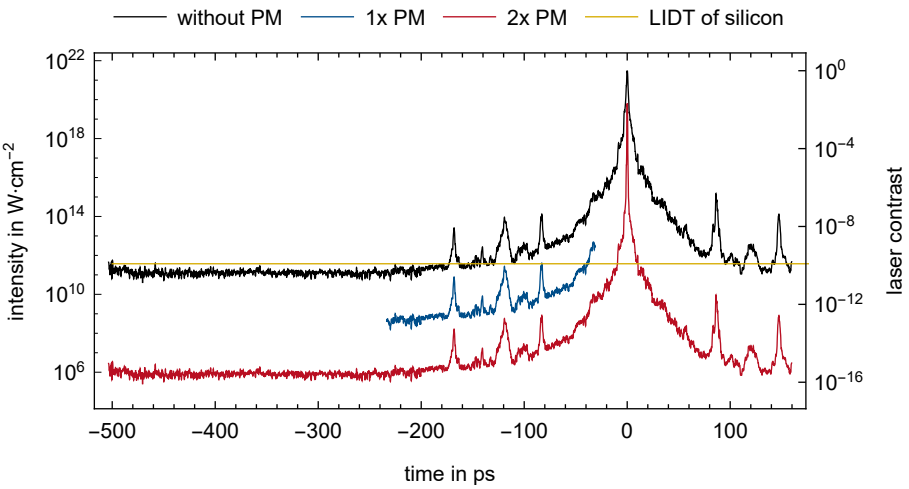

Figure 5.4.: Laser intensity and contrast of the *Vulcan* laser system. The third order autocorrelation signal of the laser system (black) shows intense pre-pulses several tens of picoseconds before the main pulse arrives. Considering the laser-induced damage threshold for silicon (yellow) the front surface of the target will be altered significantly before interacting with the slope of the main pulse. To prevent the pre-pulses from destroying the structure of the target, a double plasma mirror setup was developed that reduces these intensities (red). A single plasma mirror (blue) is not enough to decrease pre-pulse intensities well below the damage threshold of silicon.

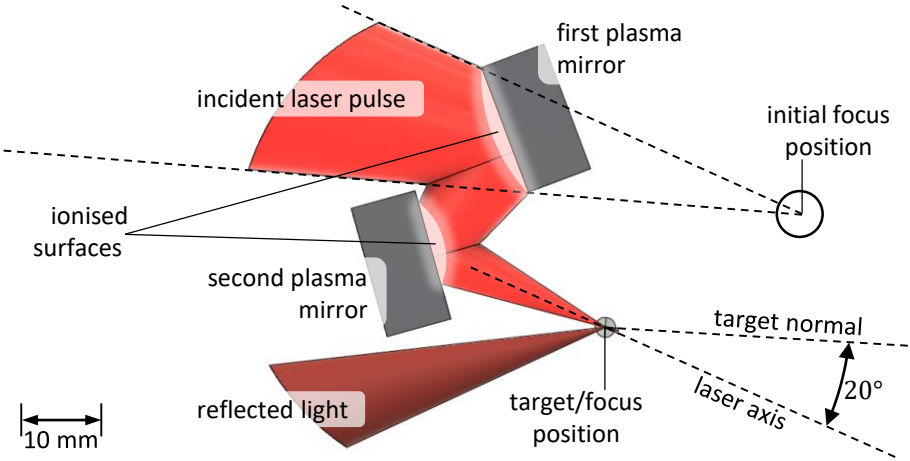

Figure 5.5.: Scaled illustration of the double plasma mirror setup for the experimental campaign. The first and second plasma mirror are placed such that the optical path of the focussed radiation is not blocked. Taking the reflected light from the target front surface into account, the orientation and positions of mirrors and target are optimised. The angle of incident of the laser axis to target normal is $20°$. The initial focus position in the target chamber shifts substantially when introducing the double plasma mirror setup. The minimum distance between the mirror surfaces is $13\,\mathrm{mm}$ and $22\,\mathrm{mm}$ between the focus position and the second plasma mirror.

The position and orientation of the two plasma mirrors is optimised in order to increase the peak intensity on the mirrors without the edges of the second mirror intersecting with the input and reflected beam, while keeping the incident angle of the laser light to target normal as small as possible.
Figure 5.4 shows the calculated contrast for the double plasma mirror setup (red) in comparison to the standard setup without plasma mirrors (black). In addition, the laser-induced damage threshold of silicon is indicated (yellow). A single plasma mirror (blue) is not able to decrease the intensity on target sufficiently below the laser-induced damage threshold of silicon. Concluding, the double plasma mirror setup shown is used in the experimental campaign. As the optical surface of the plasma mirrors is destroyed after a single laser shot due to ionisation breakdown, the mirrors have to be moved and realigned after every shot and replaced after a series of four shots.

Table 5.1.: Efficiency of the laser system and double plasma mirror setup. Due to final compression and focussing, the energy of the laser pulse in the target chamber is not equivalent to the estimated energy. In addition, based on the working principle of the double plasma mirror system the energy is further decreased. Therefore, a calibration with and without the plasma mirrors relative to the estimated energy is performed. Two measurements with varying energy yield a compression efficiency of $(70 \pm 3)\,\%$. Including the double plasma mirror setup an absolute efficiency of 26.5% (37.6% to the energy after compression) is observed.

	estimated energy	**energy on calorimeter**	**absolute efficiency**	**relative efficiency**
without	35.3 J	25.4 J		
plasma mirrors	283.1 J	194.8 J	70%	100%
with plasma mirrors	450.4 J	119.4 J	26.5%	37.6%

5.3.4 Efficiency of the laser system

The efficiency of the double plasma mirror setup is determined with several measurements of laser power in order to retrieve a close value for the intensity on target. Therefore, a calorimeter is placed in the beam path such that the beam diameter is as large as possible and as small as necessary to decrease power density. First, the laser power is measured without the plasma mirror setup and compared to the values with the setup. Table 5.1 summarises the efficiency for these two configurations.
As a reference for users, the operators of the *Vulcan* laser system measure the energy before entering the pulse compressor for each shot (estimated energy). A measurement in the target chamber without plasma mirrors gives the energy after the pulse compressor and additional optics (e.g. the entrance mirror and focussing parabola) and thereby an efficiency for all those components. From the estimated energy and the measured efficiency with and without plasma mirrors a real energy estimate on target can be calculated. From two measurements without plasma mirrors an efficiency of 70.4 % is derived. From the measurements with plasma mirrors an absolute efficiency of 26.5 % is calculated. That means a total energy transmission of 37.6 % (61.4 % per plasma mirror) is available by the double plasma mirror setup.

6 Experimental setup and acquisition of data

The layout and implementation of a successful setup for the experimental campaign is influenced by a huge number of factors. First of all, the available laser system, target chamber and double plasma mirror system enable only a certain angle around the target to be covered by diagnostics and other necessary equipment to measure the quantities described in section 5.1. In addition, all diagnostics require a certain distance and orientation in relation to the target without intersecting each other.

Table 6.1.: Overview of detection channels used in the experiment. The diagnostics are categorised into four main categories (light, x-ray, electrons and ions). Emphasised measurands indicate a qualitative and thence relative measurement between shots, as a quantitative measurement was not possible.

channel	**diagnostic**	**measurand**
light	1a) laser energy	delivered energy
	1b) scattering screen (ω)	reflected energy
	1c) scattering screen (2ω)	*interaction strength*
	1d) fibre spectrometer	*spectrum*
	1e) scattered light (off-axis)	*scattered light*
x-ray	2a) crystal spectrometer	*spectrum*
	2b) scintillator cameras	*spatial distribution*
electrons	3a) wraparound IP stack	spatial distribution
	3b) electron spectrometer	*energy spectrum*
ions	4a) radiochromic films	spatial and spectral distribution
	4b) Thomson Parabola	*energy spectrum and species*

Table 6.1 summarises the equipment for the four main diagnostic channels light, x-ray, electrons and ions. Emphasised measurands indicate a qualitative (relative) instead of a preferable quantitative measurement.
Due to the number of diagnostics special care has to be taken where to position and how to align these individual pieces of equipment. For most spectral measurements a big distance to the target is desirable in order to probe a collimated as possible beam. Opposed to this, the absolute number and spatial distribution of divergent particles are best to be measured close to the target. In addition, light and spectral x-ray measurements need a line of sight to the target front, whereas ion and electron diagnostics have to be placed facing the target backside.
Figure 6.1 shows the position of the individual diagnostics in relation to the target and incident laser pulse. For this schematic illustration all mounting and translation assemblies are not shown which lead to a complex experimental structure. Facing the front (laser incident) surface of the target diagnostics for reflected energy (1b, 1c) and x-ray spectrum (2a) are placed. Close to the target back side, the total number and distribution of electrons and ions is measured with a wraparound image plate stack (3a) above and radiochromic film stack (4a) below the plane of laser interaction. That way, the ion spectrum for target normal (4b) can be recorded together with the electron spectrum (3b). As they are not substantial for the primary discussion of the experiment, fibre spectrometers (1d), off-axis scattering screen (1e), X-ray scintillator cameras (2b) and additional ion spectrometers on the target front and backside are not shown. Even so they are considered for the complete picture, a comprehensive discussion of all details would go beyond the scope of this work.
Before a laser shot is taken, the diagnostics have to be prepared. For the described setup of diagnostics this means the vacuum chamber has to be vented to enable access and the plasma mirrors, radiochromic films and image plates can be exchanged. In order to increase the number of shots for this experimental campaign all equipment is prepared to take four shots per pump-down. This dramatically reduces the turnaround time.
The following sections present the individual primary diagnostics in more detail with a focus on the working principle and proper handling and processing of data. A thorough analysis and discussion of the extensive dataset acquired is included in chapter 7.

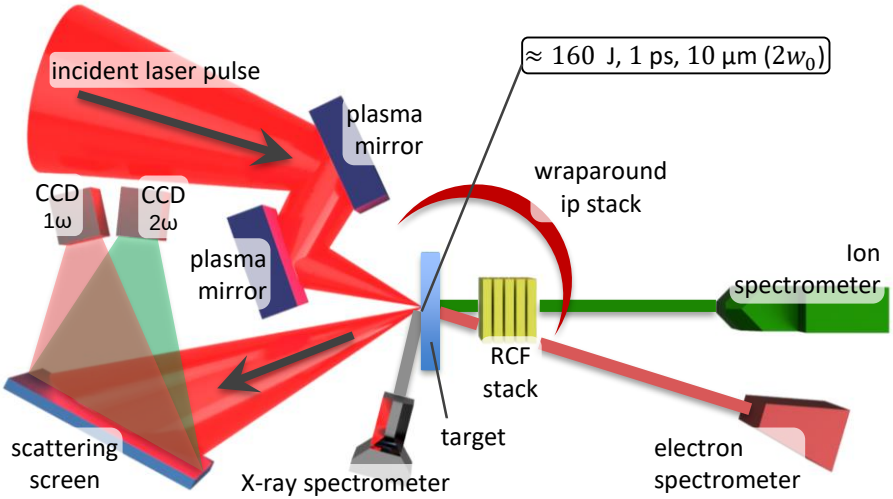

Figure 6.1.: Simplified schematic setup used for the campaign at the *Central Laser Facility* investigating the influence of structured targets to laser-plasma experiments. The arrangement of diagnostics and equipment around the central interaction is critical. Facing the laser incident target surface the scattering screen for reflected light (ω and 2ω) and X-ray spectrometer are placed without intersecting with the double plasma mirror setup. The image plate (IP) and radiochromic film (RCF) stack are positioned close to the target backside. Ion and electron spectrometer are positioned with a maximised distance to central interaction to probe highly collimated particle beams. As a rule of thumb diagnostics for an absolute particle count are placed as close as possible, whereas equipment gaining spectral information is placed as far as possible from the interaction region. The illustration does not show all diagnostics and equipment used within the experimental campaign.

6.1 Image plates

Within the diagnostics in this experimental campaign Fujifilm image plates (IPs)[98–100] are used for the detection of charged particles and x-ray radiation in the x-ray,[100] ion[101] and electron spectrometers.[102] These flexible image sensors offer a high dynamic range with high resolution while being re-usable. The types of IPs used in this experiment are BAS-MS (*multipurpose standard*), BAS-SR (*super resolution*) and BAS-TR (*tritium*). The thickness composition of these types is slightly different whereas the general combination of layers is identical. The active layer is protected by a thin layer of Mylar and coated to a polyester support film with a magnetic base layer. The active layer consists of photo-stimulable phosphor of barium fluorobromide containing a trace amount of bivalent europium (Eu) as a luminescence centre ($BaFBr:Eu^{2+}$). If energy is absorbed by the active layer, electrons are excited to a meta-stable state in Eu. After excitation, these electrons stay in this state until they are exposed to red laser light and excited to a higher level, that rapidly decays. Thereby blue light is emitted. This process is known as *photo-stimulated luminescence* (PSL).

After the image plates are exposed to the interaction in the experiment and removed from the chamber, the PSL signal can be used to extract spatial and intensity information of the particle or radiation beam that was absorbed by the IP. For that task a red laser is rasterised over the IP inside the scanner and the blue light produced by luminescence is collected via a waveguide on a photomultiplier tube (PMT). The result is a digital picture with grayscale intensity values.

The grayscale value is limited by the dynamic range of the IP scanner. This can lead to saturation of the scanned image if the incident signal is too strong. Nevertheless, the absolute value of the signal can be retrieved by scanning the image plate multiple times. This will lower the number of excited electrons and therefore reduces the PSL signal. To gain absolute PSL readings an evaluation of the decay must be extrapolated from an unsaturated scan. Figure 6.2 shows the relative PSL signal versus scan number obtained with the image plate scanners during the experimental campaign.

[98] B. Hidding et al. *Rev. Sci. Instrum.* **78**, 083301, 2007.
[99] B. R. Maddox et al. *Rev. Sci. Instrum.* **82**, 023111, 2011.
[100] A. L. Meadowcroft, C. D. Bentley, and E. N. Stott. *Rev. Sci. Instrum.* **79**, 113102, 2008.
[101] C. G. Freeman et al. *Rev. Sci. Instrum.* **82**, 073301, 2011.
[102] K. A. Tanaka et al. *Rev. Sci. Instrum.* **76**, 013507, 2005.

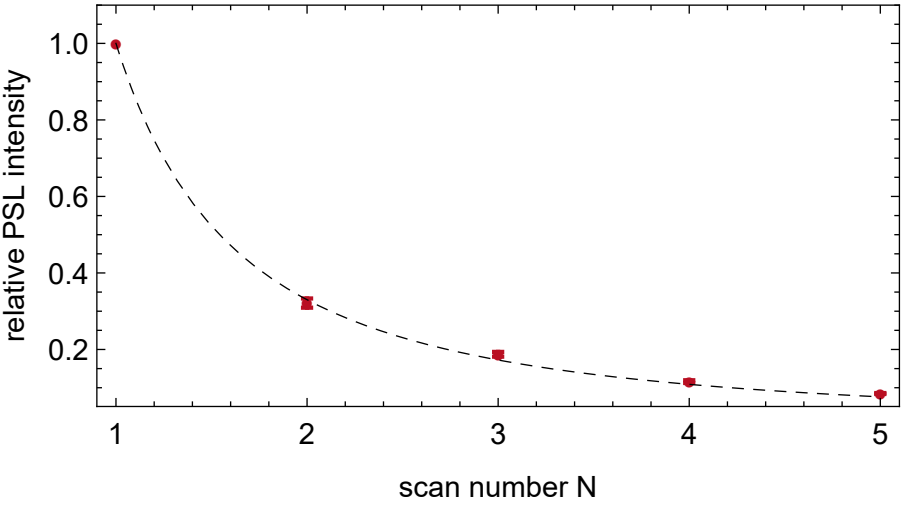

Figure 6.2.: The relative photo-stimulated luminescence (PSL) signal versus scan number N follows a power law fit. With this, the typically saturated image plate readings can be converted to absolute values.

The decay of the signal with consecutive scan number N (red) follows a power law fit of the form $N^{1.6}$ (dashed). To convert the image to PSL units, the following formular is used[103]

$$\mathrm{PSL}(G) = \left(\frac{G}{2^{16}-1}\right)^2 \left(\frac{\mathrm{RES}}{100}\right)^2 h(V)\, 10^{L/2} N^{1.6}, \tag{6.1}$$

with pixel value G, scan resolution RES in μm, scanner dependent sensitivity function $h(V)$, dynamic range latitude L and scan number N. For the extraction of particle numbers from the PSL signal further processing taking the sensitivity of the films and a thorough calibration needs to be taken into account.[104]

6.2 Radiochromic films

The active layer of radiochromic films (RCF) changes colour proportional to the absorbed energy dose of energetic particles or electromagnetic radiation. Here

[103] G. J. Williams et al. *Rev. Sci. Instrum.* **85**, 11E604, 2014.
[104] T. Bonnet et al. *Rev. Sci. Instrum.* **84**, 103510, 2013.

the colourisation of combined RCF provides spatial and spectral information of the accelerated ions from target. After irradiation an exposed RCF is digitised using a medium format scanner (*Nikon Super Coolscan 9000 ED*) into 16-bit red, green and blue (RGB) channels. Each colour shows a different opacity relationship. In this thesis *GafChromic*®RCF of the types HD-V2[105] and EBT-3[106] by the manufacturer *Ashland Global Speciality Inc.* were used. HD-V2 consists of a 8 µm active layer with a dynamic dose range from 10 Gy to 1000 Gy and a 97 µm supporting transparent substrate. EBT-3 consists of a 28 µm active layer with a dynamic dose range from 0.1 Gy to 20 Gy embedded in between two matte supporting layers with a thickness of 125 µm each.

For protons and ions the energy deposition in materials is well understood. In the energy range of MeV to GeV ($0.04 < \beta \cdot \gamma = (v/c) \cdot 1/\sqrt{1-(v/c)^2} < 500$) the stopping power is described using the Bethe-Bloch relationship[107]

$$\frac{dE}{dx} = \rho z_{\text{ion}}^2 \frac{Z}{A} \left(\frac{4\pi (\hbar c)^2 \alpha^2}{m_p m_e c^2} \right) \cdot \left(\frac{1}{\beta^2} \log \left(\frac{2 m_e c^2 \beta^2 \gamma^2}{I} \right) - 1 \right). \tag{6.2}$$

With the charge number z_{ion} of the stopping ion, mass number A and charge number Z of the irradiated material, Sommerfeld's fine structure constant α, proton and electron mass m_p and m_e and Lorentz factor γ. Thereby, the mass density $\rho \propto m_p(A/Z)n_e$ is proportional to the electron density n_e. The mean ionisation energy of the electrons is proportional to $I \propto Z\alpha^2 m_e c^2$. For small energies ($\beta\gamma < 0.04$) the Bethe-Bloch relationship is no longer valid, as the slow ions strip electrons from the atomic shell of the absorber and thereby reduce the effective value of z_{ion}. For high energetic ions ($\beta\gamma > 500$) bremsstrahlung needs to be considered.

Equation 6.2 shows no linear dependency on the velocity ($\beta = \frac{v}{c}$) of the ions. The stopping is initially continuous, increasing rapidly with the further loss of velocity. This leads to the ion loosing most of its kinetic energy at a certain depth until it is stopped. Thereby an interaction with the Coulomb field of the absorber nuclei dominates and leads to an increased deposition of energy in the absorber material. This behaviour leads to a characteristic feature of ion stopping in materials: the so-called Bragg peak.

[105] Gafchromic HDV2. Ashland Global Speciality Inc. URL: http://www.gafchromic.com/documents/gafchromic-hdv2.pdf (accessed 01 April 2018).

[107] J. L. Basdevant, J. Rich, and M. Spiro. Fundamentals In Nuclear Physics. 2nd ed. Springer, 2005.

To gain spatial and spectral information of ions escaping the target in the experiment, the RCFs are layered with filter materials to utilise the characteristic Bragg peak behaviour. Hence, the active layer of an RCF at a certain depth in the stack is only sensitive to protons above a certain threshold energy. In addition, the RCF is ideally large enough to sense the angular profile of the ion beam. With this approach it is comparably easy to extract the maximum proton energy, once the threshold energies of the stack design are simulated using a Monte Carlo approach. In addition, the proton spectra can be identified by knowing the response curve for each layer of the stack. The final layer of the RCF stack with a visible signal signalises the maximum proton energy which is well known. With an iterative approach the layer before is sensitive to ions with a smaller threshold energy as well as ions penetrating deeper. These have to be subtracted from the absolute signal and so on.
Furthermore, for the proper extraction of a particle spectrum the scanning of radiochromic films has to be calibrated for all colour channels of the scanner. A comprehensive documentation of the RGB-calibration for the analysis used in the scope of this work can be found in the bachelor thesis of *A. Schreiber*.[108]
Measuring the spatial and spectral distribution of electrons and ions simultaneously is possible using an angular wraparound stack[109]. Even so different configurations have been used throughout the experiment, the general setup is straight forward. The stack consists of alternating layers of image plates and filter materials and is wrapped concentrically curved around the target, which provides angular information about the emission. To detect ions, RC films and additional filter materials are added on the inner surface. Proton contamination of the image plates has to be avoided in order to protect the image plates and resolve a clean electron spectrum.

6.3 Scattering screen

On the scattering screens, light reflected and scattered from the target is collected and imaged by cameras. Figure 6.1 at the beginning of this chapter includes a schematic illustration of the setup.
In order to quantify the amount of energy absorbed by the target, the transmission, reflection and scattering of the incident laser pulse has to be char-

[108] A. Schreiber. RGB-Farbkalibrierung von radiochromatischen Filmen. Bachelor Thesis. Technische Universität Darmstadt, 2012.
[109] R. J. Gray et al. *Appl. Phys. Lett.* **99**, 171502, 2011.

acterised. The amount of transmitted light is negligible. Light directly reflected from target is collected on a ground glass screen with a total size of 450 mm × 450 mm. This screen is monitored by two wavelength bandpass filtered cameras: one camera for the fundamental wavelength of 1053 nm, the other camera for the frequency doubled wavelength of 526.5 nm.

In addition, two optical fibre spectrometers analyse the spectral distribution of the reflection. The scattered light is collected on an additional scattering screen with an additional camera, shielded from the directly reflected light by a tube and enclosure.

An absolute measurement of reflected light requires a calibration of the scattering screen. This is only possible for the fundamental wavelength camera, as for a calibration the energy on the scattering screen needs to be known. Therefore, a mirror was placed after the position of the target in order to reflect the energy during a low intensity shot on to the scattering screen without target. Doing so, a known amount of light due to the plasma mirror calibration is collected on the scattering screen and serves as a reference for the brightness value measured by the camera. Neglecting the scattered light on the main scattering screen, the amount of reflected light is equivalent to the sum over all pixel values and can be converted to an absolute percentage value of the incident light and a relative value for the frequency doubled radiation. A valid comparison is only achieved by taking the attenuation of the neutral density filter and gain value of the camera into account.

Figure 6.3 shows exemplary data from the main scattering screen diagnostic (ω and 2ω) obtained from a shot on a flat silicon target.

The two cameras for the main scattering screen give no spectral information for the reflected and scattered light. Hence, two fibre spectrometers are collecting a broad spectrum (172 nm to 1100 nm) from the scattering screen with a resolution of 16 bit. The spectrometers are set up with different attenuations in order to avoid saturation of the 2ω line while being able to resolve the fundamental ω at the same time.

The off-axis scattering screen is intended to generate a reference signal for the amount of scattered light by the target. The camera and screen have to be carefully shielded from the incident and reflected light as the signal is orders of magnitude below in intensity. For this diagnostic only a relative comparison between the shots for a fixed position in the chamber is possible.

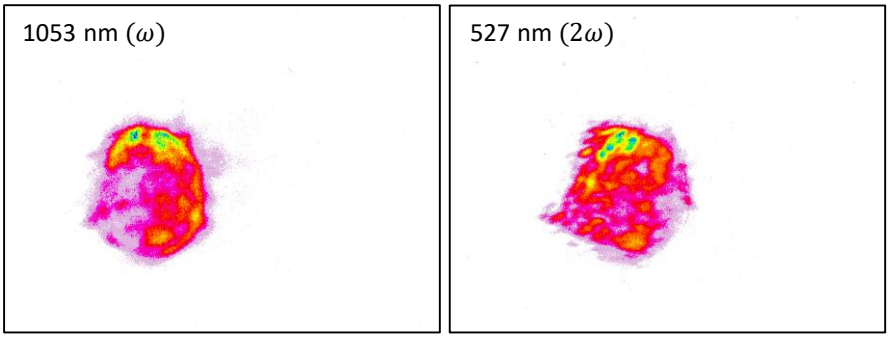

Figure 6.3.: Exemplary scattering screen images taken with the diagnostics for ω (left) and 2ω (right). The fundamental reflection from a flat target (left) shows a concentric beam. The emission of frequency doubled light (right) is an indicator for the strength of the initial interaction and shows a homogeneous profile.

6.4 Conical X-ray spectrometer

With spectroscopy of characteristic x-ray lines the stage of ionisation of the silicon target and thereby the strength of the interaction can be determined. Usually, the intensity of these lines is weak and superposed by bremsstrahlung. An extremely low signal-to-noise ratio is expected. Therefore, a spectrometer with a conical crystal is used within this experiment, which offers an increased collection efficiency of photons onto a smaller region on the detector, compared to a flat crystal, as described by *Martinolli et al*.[110] This setup increases spatial focussing and offers a reasonable spectral range while being compact.
The schematic setup is illustrated in figure 6.4 and based on the work initially proposed by *T. A. Hall*.[111]
The surface of a highly oriented pyrolytic graphite (HOPG) is curved to form a cone (dashed lines). Thereby, electromagnetic radiation from a fixed point in relation to the crystal (source) is focussed and spectrally resolved on a line on the image plate used (image plane). The alignment of the conical spectrometer is critical. Ideally the target front surface lies in the source focus of the conical crystal. The line of sight is chosen by an entrance aperture. In addition, the setup needs to be shielded from charged particles. Therefore, a strong deflection magnet is placed in front of the spectrograph and thick lead blocks are shielding the setup.
To retrieve the x-ray spectrum from a scanned image plate the dispersion model for the conical crystal spectrometer was modelled. It is nearly linear for the covered spectral range between 1.60 keV and 1.88 keV.
An exemplary X-ray spectrum obtained using the conical crystal spectrometer is shown in figure 6.5. Within the spectral range three dominant regions (1-3) are identified. The He_α (1), Li-like (2) and Ly_α (3) lines of silicon emerge from strong transitions in the plasma region on the target.

[110] E. Martinolli et al. *Rev. Sci. Instrum.* **75**, 2024–2028, 2004.
[111] T. A. Hall. *J. Phys. E Sci. Instrum.* **17**, 110, 1984.

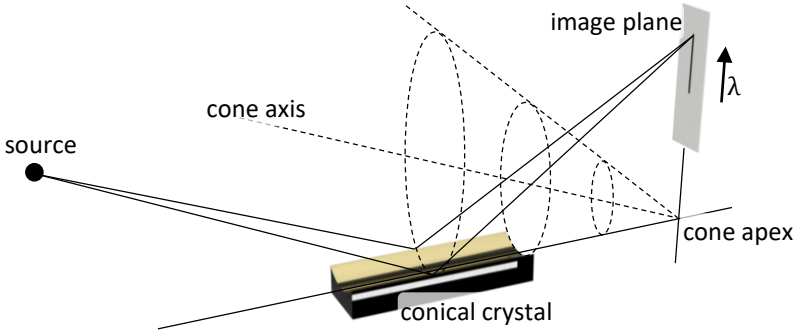

Figure 6.4.: Working principle of a conical crystal x-ray spectrometer. The highly oriented pyrolytic graphite (HOPG) crystal is shaped to form a cone with illustrated apex and central axis. Thereby, incident X-ray radiation from the source is focussed into a sharp line on the image plane. Here, image plates are used to collect spectral information of the photon energies in the range from $1.60\,\mathrm{keV}$ to $1.88\,\mathrm{keV}$.

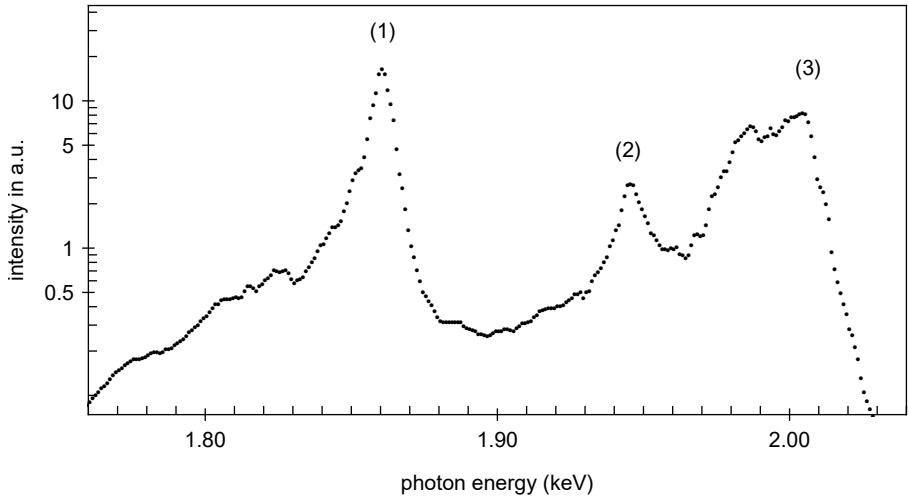

Figure 6.5.: Exemplary X-ray spectrum measured with the conical spectrometer in the spectral range from $1.60\,\mathrm{keV}$ to $1.88\,\mathrm{keV}$. Three characteristic lines of silicon can be identified: He_α (1), Li-like (2) and Ly_α (3). These transitions are an indicator for the strength and temperature of the initial interaction.

6.5 Electron spectrometer

To resolve the energy spectrum of electrons escaping the target, a magnetic electron spectrometer is used. As depicted schematically in figure 6.7, this device consists of a cylindrical electromagnet that deflects electrons depending on their energy onto an image plate.

Electrons enter the spectrometer through an aperture. The alignment is such, that ideally a straight line between the point of interaction, pinhole, centre of the magnet and zero point on the image plate exists. Thereby, the spectrometer probes a highly collimated portion of the divergent electrons emitted from target.

In theory, the zero position on the image plate represents electrons without displacement (and thereby infinite energy). This position is needed to convert the spectrum from pixel position to electron energy. It is identified by the deposition of (undeflected) x-ray radiation from the interaction point and indicated by the red arrow in figure 6.7 and figure 6.6. The centre of this feature matches the line of sight from the entrance pinhole to the interaction point. The exact position of the zero position is determined by the position between the rising and falling edge within the scan.

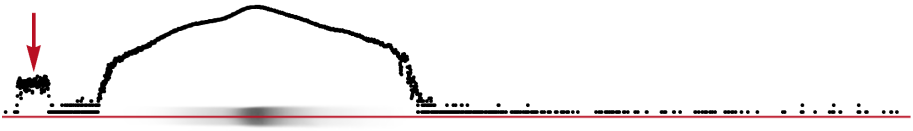

Figure 6.6.: Processed raw electron spectrum scan. First, the position and orientation of the centre line of the spectrum is identified (red line). The pixel values along this line are shown on a logarithmic scale (black). Next, the zero position (no deflection by the magnet) is identified (red arrow). After that, the spectrum is converted from pixel value and position to electron number and energy.

A scanned image plate is shown in figure 6.6 together with the logarithmic profile of the spectrum along its center line (red arrow). Using the *Segmentation Analysis* Function of Wolfram Mathematica© the orientation and center of this line is identified and the shown profile of the spectrum is obtained.

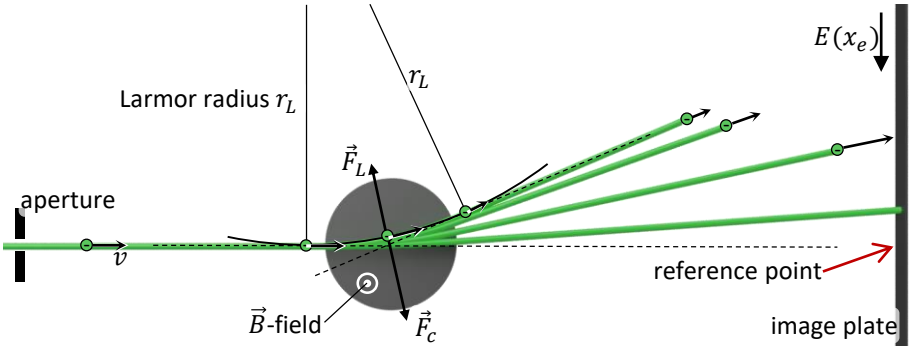

Figure 6.7.: Schematic of the electron spectrometer deployed. A cylindrical magnet of radius R deflects electrons in relation to the kinetic electrons onto a strip of image plate. The charged particles enter the diagnostic through an aperture to probe a collimated beam. Electromagnetic radiation is not affected by the magnetic field and illuminates a reference point on the image plate. The deflection of electrons is mathematically described by the Lamor radius r_L as a result from the balance of centripetal force $\vec{F}_c$ and Lorentz force $\vec{F}_L$. Within this experiment the electrons have to be considered relativistically. Electrons with the highest velocity see minimum deflection from the reference point.

The idealised displacement for an electron passing a cylindrical magnet follows from the relativistic description of the Larmor radius, derived from the balance of centripetal force F_c and the magnitude of the Lorentz force F_L, by[47]

$$r_L = \frac{\gamma_0 m_e v}{eB} = \frac{p_e}{eB} = \frac{\sqrt{\frac{E^2}{c^2} - (m_e c)^2}}{eB}, \tag{6.3}$$

with relativistic Lorentz factor γ_0, electron mass m_e and velocity v, elementary electric charge e and magnetic field B. The Larmor radius is thus dependent on the relativistic electron momentum p_e or kinetic energy E, respectively . The spatial displacement x_e of the electron on the image plate with distance L to the magnet is defined by the angle θ with

$$\tan(\theta) = \frac{x_e}{L} \quad \text{and} \quad \tan\left(\frac{\theta}{2}\right) = \frac{R}{r_L}, \tag{6.4}$$

and thereby linked to the Larmor radius r_L and radius of the deflection magnet R.
In summary, the energy dependent displacement $E(x_e)$ of the electrons on the image plate is given by

$$E(x_e) = c \cdot \sqrt{\left(\frac{eBR}{\tan\left[\frac{1}{2} \cdot \arctan\left[\frac{x_e}{L}\right]\right]}\right)^2 + (m_e c)^2}. \tag{6.5}$$

This theoretical description is assuming a homogeneous magnetic field that is only present in between the cylindrical magnet plates. The real radial decline of the magnetic field is shown in figure 6.8 (top). A numerical CST simulation (red) of electrons passing the declining magnetic field is shown in 6.8 (bottom) in comparison to the theoretical model (black) described above. The simulation is approximated by a non-linear model (dashed)

$$x_e(E) = \frac{4.70856}{x_e} \frac{\text{MeV}}{\text{mm}}. \tag{6.6}$$

This equation is used to convert the image plate scans to electron energies.

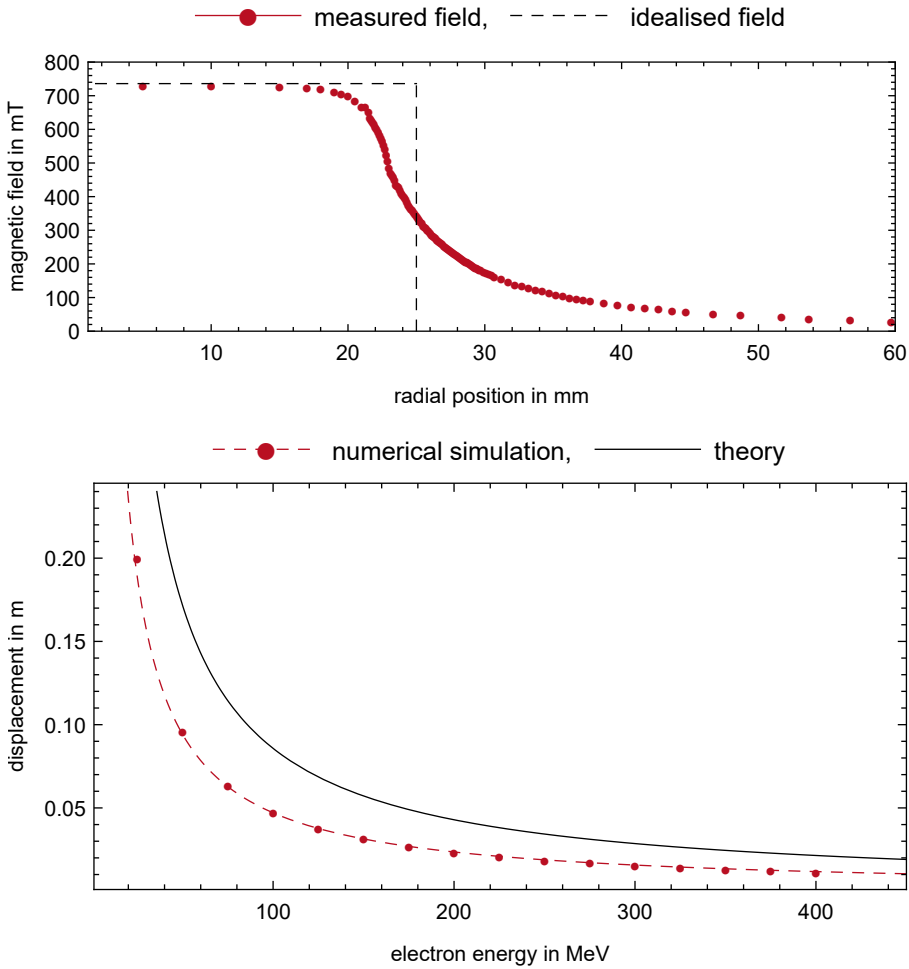

Figure 6.8.: The electromagnet inside the electron spectrometer (top) shows a continuous decay of the magnetic field strength (red) in comparison to the idealised field of a cylindrical magnet (dashed). Thereby, the displacement of electrons as a function of their kinetic energy (bottom) cannot be calculated analytically (black). A numerical *CST* simulation yields the real displacement of electrons (red) taking the measured magnetic field into account.

6.6 Thomson ion spectrometer

In addition to the energy dependent deflection of the electron spectrometer described above, a Thomson ion spectrometer (named after *J. J. Thomson*,[112] who demonstrated this technique in 1911) shows a dependency on the charge to mass ratio q/m of an ionised particle entering the diagnostic. Therefore, it is used for the spectral characterisation of ions within this experiment.
The general setup for a Thomson ion spectrometer is illustrated in figure 6.9. The working principle of ion separation is achieved by a combination of magnetic and electric fields. Ions crossing electric field lines perpendicular to their direction of movement are deflected along the field lines. Ions crossing a magnetic field are diverted perpendicular both to the magnetic field lines and the direction of motion. The amount of deflection for both fields is thereby dependent on the velocity of the charged particle. The deflection due to both fields on the screen is perpendicular to each other. To probe mostly collimated ions, an entrance aperture (pinhole) is used. With a parallel orientation of the magnetic and electric fields, collimated ions with a certain charge-to-mass ratio are hence deflected onto an image plate detector.
The mathematical description of the displacement enables a deeper insight on the working principle of a Thomson ion spectrometer. The displacement (x, y) from zero point of ions with relativistic velocity v_z and charge to mass ratio q/m on the image plate reads[113]

$$x = \frac{qE_0L_E}{\gamma m v_z^2}\left(\frac{L_E}{2} + D_E\right) \propto \frac{q}{m}\frac{1}{\gamma v_z^2}, \tag{6.7}$$

$$y = \frac{qB_0L_B}{\gamma m v_z}\left(\frac{L_B}{2} + D_B\right) \propto \frac{q}{m}\frac{1}{\gamma v_z}, \tag{6.8}$$

with Lorentz factor γ, electric field strength E_0, magnetic flux density B_0. Additionally, geometrical constraints have to be considered, as the length of magnetic and electric field regions L_B and L_E and their distance to the detector D_B and D_E, as indicated in Figure 6.9.
A fixed charge to mass ratio q/m is thereby proportional to a parabolic arc on the detector[113]

$$\frac{q}{m} \propto \frac{x^2}{y}\gamma. \tag{6.9}$$

[112] J. J. Thomson. *Philos. Mag. Ser. 6* **21**, 225–249, 1911.
[113] A. Alejo et al. *J. Instrum.* **11**, C10005, 2016.

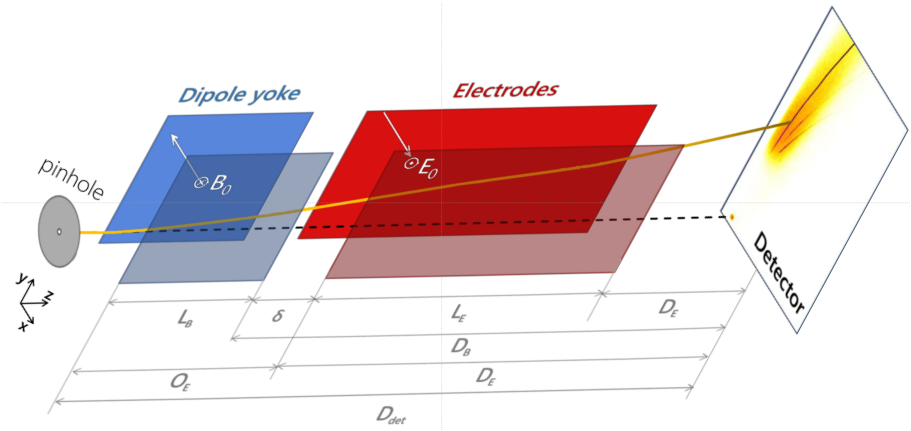

Figure 6.9.: Schematic illustration of the working principle of a Thomson parabola ion spectrometer. Magnetic fields (dipole yoke) and electric fields (electrodes) deflect charged particles, entering the diagnostic through a pinhole to probe a collimated sample, based on their kinetic energy. Neutral particles and radiation are not interacting with these field (dashed line). The change of momentum by the magnetic field is directed along y, perpendicular to the field lines and the direction of movement. For the electric field the deflection is directed along x, coplanar to the field lines. The combined deflection from the reference point on the detector (here, image plates are used) leads to parabolic traces that depend on the geometric distances (L, D) and field strengths (E_0, B_0) and charge to mass ratio of the ion. Reprinted from Ref. [113] (figure 1).

An exemplary image plate scan from this experiment is shown in figure 6.10. The zero point is shown together with the magnetic and electric force vector. Four prominent parabolic traces can be identified with a charge to mass ratio of 1:1, 1:2, 5:12 and 1:3. The most prominent 1:1 line represents protons (H^+), the other three parabolic arcs carbon ions (C^{6+}, C^{5+} and C^{4+}).
Converting the image plate scan intensity to PSL and transferring the pixel position to the corresponding kinetic energy value, the spectrum for a certain q/m is evaluated. Figure 6.10 (bottom) illustrates the proton spectrum from the IP scan seen in figure 6.10 (top). Here, intensity values are binned with a width of 0.5 MeV. The resulting spectrum can be approximated by a two-temperature distribution, shown in red. For one mean temperature $k_B T$ the intensity distribution is proportional to

$$I(E_{\text{kin}}) \propto \frac{N_{\text{ion}}}{\sqrt{k_B T_{\text{ion}}}} e^{-\frac{E_{\text{kin}}}{k_B T_{\text{ion}}}}, \tag{6.10}$$

with the mean ion temperature T_{ion} and number N_{ion}, kinetic energy E_{kin} and Boltzmann constant k_B.

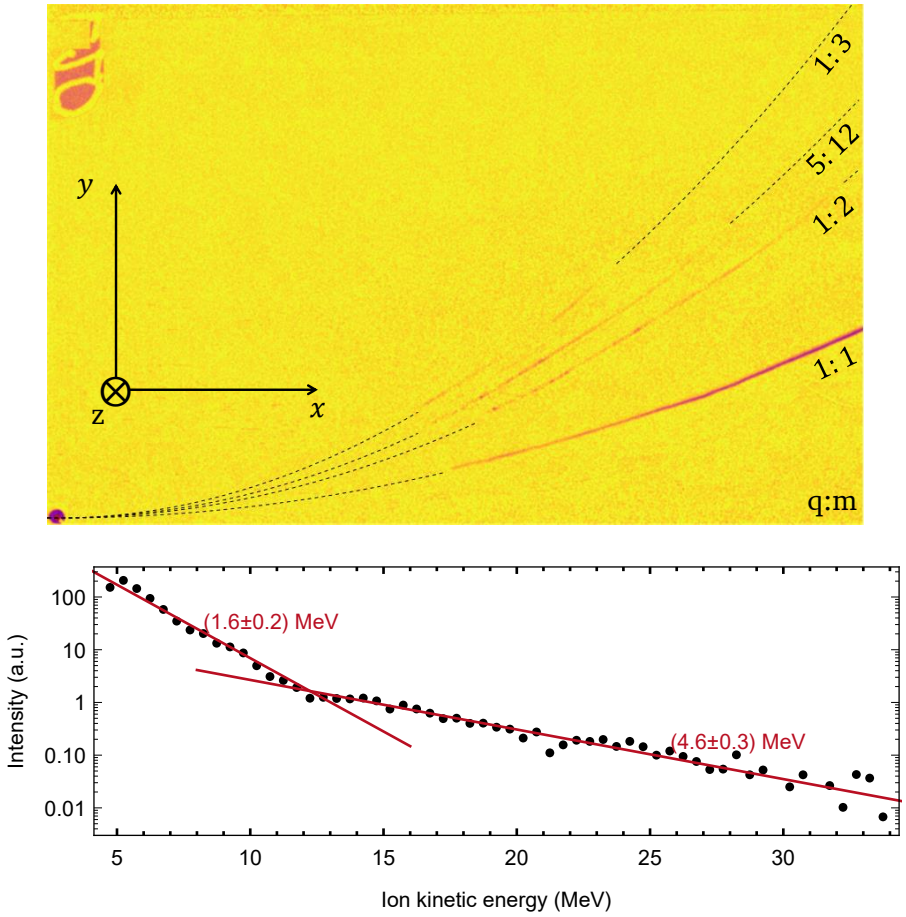

Figure 6.10.: Exemplary Thomson parabola traces measured in the experiment (top). Four parabolic lines are visible due to different charge to mass ratios q/m of ions present in the acceleration spectrum from a solid silicon target. The dominant line with a ratio of 1:1 represent protons (H^+), the remaining arcs carbon ions (C^{6+}, C^{5+}, C^{4+}) from a contamination layer on the target backside. The proton spectrum shows a two-temperature distribution, when shown against kinetic energy (bottom). Approximating both spectral regions (black) each by a Maxwell-Boltzmann distribution with single temperature (red) the mean kinetic energy can be extracted.

7 Results

Within the following sections main results of the experimental campaign are portrayed. Thereby, the influence of structured targets to reflected and emitted light (section 7.1), dynamic of electrons (section 7.2), generated x-ray radiation (section 7.3) and acceleration of ions (section 7.4) is demonstrated.

During the experiment a preferably extensive amount of the laser pulse parameters and data of the individual shots is collected. The setup of the experiment is optimised to take four successive laser shots on different targets during a single pump down of the vacuum chamber. After a maximum of four shots the image plates of the individual diagnostics are scanned and documented together with the information gathered by other diagnostics. This collection is critical for the proper analysis of the experimental campaign and further processing and categorising of data.

All shots are ranked individually by the performance of the laser system (pulse energy, pulse length, position of focus, etc.) and successful operation of the diagnostic channels. Due to the comprehensive experimental structure, a number of parameters have to be considered. As a result, the collection of *successful* and *unsuccessful* shot numbers for the different target types is identified. With a total of 115 shots during the campaign (including calibration and alignment), this set consists of 24 individual and favourable events. Thereby included, 8 flat, 5 groove, 4 pillar and 7 needle targets were probed.

In the following discussion, typically the averaged value and standard deviation of the signal is presented. Thereby, a general trend and measurement of fluctuations between shots per target type can be presented. Please note, that it is generally not feasible to include all possible sources of uncertainty and eventuality. Whenever viable a contemplation and propagation of uncertainties is presented.

7.1 Reflected and emitted light

The efficient absorption into the target is important, as the conversion efficiency of all further processes (e.g. acceleration of electrons and ions, generation of x-ray radiation) depend on the initial interaction of the laser with electrons in the target. Furthermore, applying surface structures with highly light absorbing properties in the regime of linear optics does not naturally increase the absorption of laser light to an intense plasma region. Therefore, a thorough investigation of reflected and emitted light is necessary.

The reflection of fundamental radiation ($\lambda_{\mathrm{FUN}} = 1053\,\mathrm{nm}$) from the target front onto the scattering screen is shown in figure 7.1 for a flat, groove, pillar and needle target, as indicated. For visibility, the pixel brightness values of the image have been inverted. Furthermore, the individual images share an absolute brightness scale that is calibrated to the energy per pixel.

The four targets show a characteristic reflection pattern, depending on the structure type. For flat targets a bright circular reflection is observed. For groove and pillar targets the pattern indicates that a geometric structure is still present at the time the peak pulse intensity is interacting with the target. The overall brightness is decreased, while a distinct pattern is observed. For the grooved target three well-defined circles are visible, that are shifted vertically in accordance with the orientation of grooves on the target surface. For the pillar structure the pattern is apparent both horizontal and vertical, for the same reason. Using the needle targets a dim concentric reflection is observed.

In addition to the exemplary shots shown in figure 7.1, the averaged fundamental reflection ($\lambda_{\mathrm{FUN}} = 1053\,\mathrm{nm}$), together with the emission of frequency doubled light ($\lambda_{\mathrm{SHG}} = 527\,\mathrm{nm}$) for flat, groove, pillar and needle targets is summarised in table 7.1. The measurements for the different target types show mean value and standard deviation for the number of shots taken.

As described in section 6.3, the diagnostic for fundamental radiation shows an absolute measurement of reflected energy in J. The frequency doubled camera is not calibrated and intended to present a relative measurement valid for a comparison in arbitrary units (a.u.).

The amount of 1053 nm light reflected is significantly decreased for pillar and needle targets in comparison to flat foils. This means, for the latter an additional $(14 \pm 3)\,\%$ of the initial laser energy is transferred to an increased absorption into target or off-axis scattering from the front surface. In addition, the frequency doubled signal emission detected, shows a strong reduction for

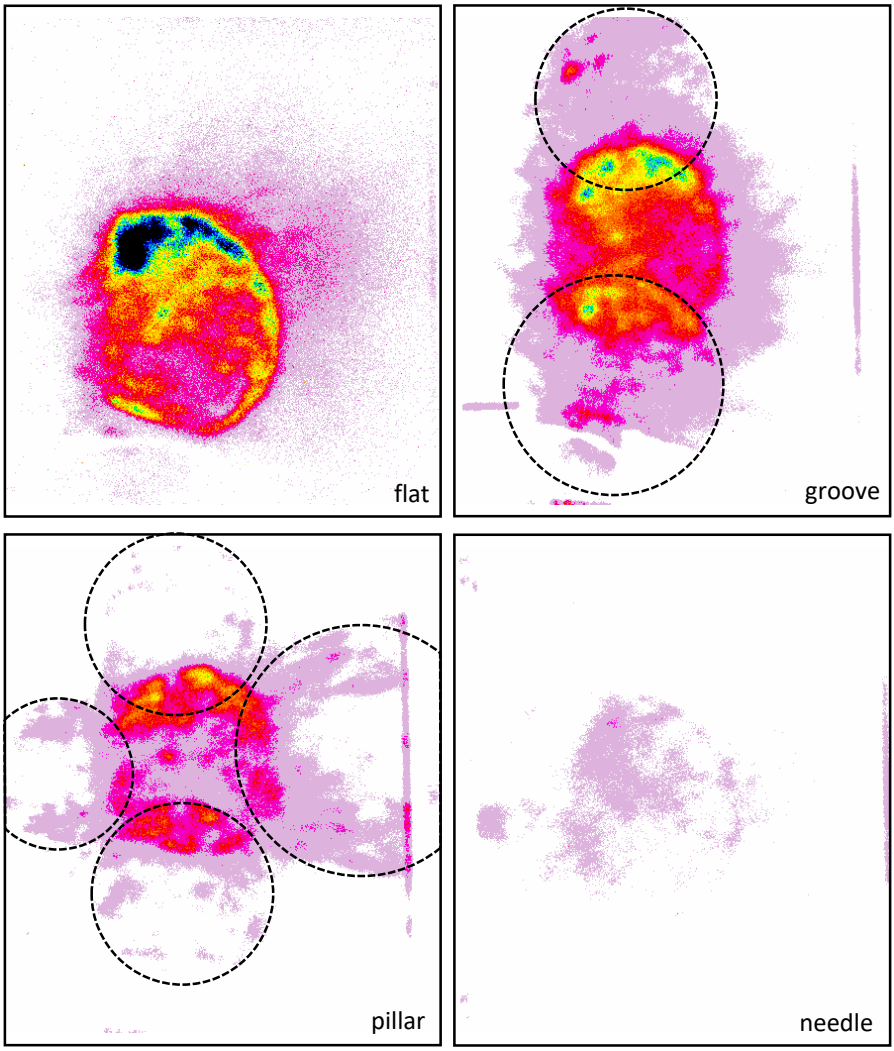

Figure 7.1.: The reflection of $1053\,\mathrm{nm}$ light from target is strongly affected by the front surface structure type. A flat silicon target shows a strong illumination of the scattering screen. Needle structures in comparison show very little reflection from the target front. Intermediate, groove and pillar structures show diffraction patterns related to the initial surface structure (dashed).

Table 7.1.: Averaged fundamental reflection and second harmonic emission signal for the four target types. A total number of 8, 5, 4 and 7 successful shots is considered for these measurements. Needle structured targets show a remarkable decrease for both detection channels. Fundamental reflection drops to 30%, second harmonic emission to 11% of the value achieved with flat targets. Groove and pillar targets, cover the intermediate range.

target type	**flat**	**groove**	**pillar**	**needle**
no. of shots	8	5	4	7
$\lambda_{FUN} = 1053\,\text{nm}$	$(20 \pm 3)\,\%$	$(21 \pm 3)\,\%$	$(13 \pm 3)\,\%$	$(6 \pm 1)\,\%$
$\lambda_{SHG} = 527\,\text{nm}$	$(13 \pm 6)\,\text{a.u.}$	$(4 \pm 2)\,\text{a.u.}$	$(2.0 \pm 0.8)\,\text{a.u.}$	$(1.4 \pm 0.6)\,\text{a.u.}$

pillar and needle in comparison to flat targets. An absolute measure for the amount of scattering in the experiment is important, in order to quantise the absorption to target.

Figure 7.2 shows the spectral distribution, collected by the fibre spectrometers at the chamber window. For visibility, the montage shows a close-up of the fundamental ($\lambda_{FUN} = 1053\,\text{nm}$), frequency doubled ($\lambda_{SHG} = 527\,\text{nm}$) and tripled ($\lambda_{THG} = 351\,\text{nm}$) spectral region. From the spectra decreased reflection (and scattering) characteristics are visible. Between flat, groove, pillar and needle structures, the spectral intensity for all three regions decreases continuously. At the same time the standard deviation reduces, resulting in the most reliable spectrum for needle targets. The generation of higher harmonics scales with intensity as $I_{SHG} \propto I^2$ and $I_{THG} \propto I^3$?[77] The decrease for structured targets is thereby not only due to enhanced light trapping, but also due to an increased interacting surface area.

In summary, the reduction in light escaping the front surface indicates that the energy coupling to the target is enhanced significantly. At the same time, the surface energy is decreased due to an increase in interacting area. With the improved energy coupling to the target there are significant changes in the laser-driven radiation and particle sources.

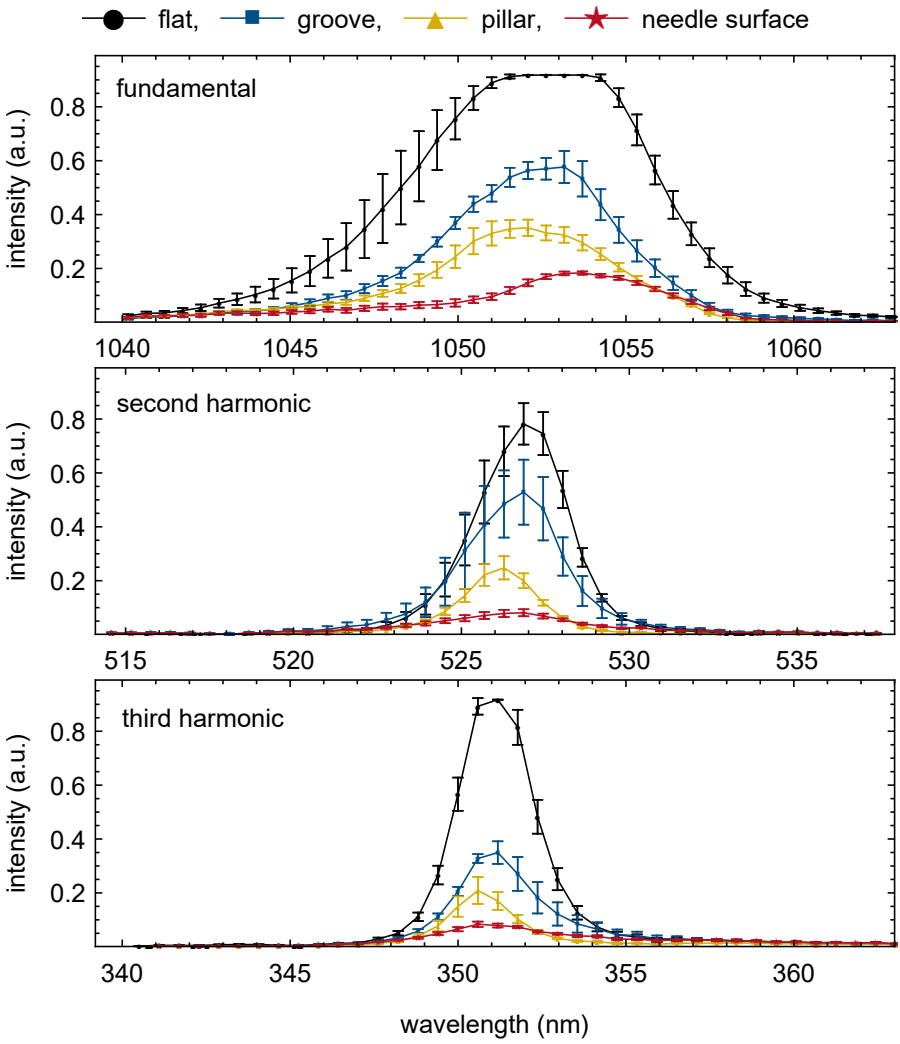

Figure 7.2.: Averaged reflection spectrum from the front surface for four different structure types. The spectral intensity measured for fundamental (top), second harmonic (middle) and third harmonic radiation (bottom) demonstrate a clear picture for the reflection from different structured surfaces. Flat targets (black) show the strongest emission for all lines. For needle targets a consistent and reliable reflection behaviour is observed in comparison to the other target types. Error bars show the standard deviation.

7.2 Production of electrons

The distribution of electrons generated and accelerated by an intense laser pulse is expected to be altered depending on the shape and structure of the laser incident surface. In addition, a modified flux of electrons through the target will change the electron sheath on the target backside and thereby modify the acceleration of ions. The spatial and spectral distribution of electrons is measured in the experiment with a magnetic electron spectrometer and image plate wraparound stack.

The averaged electron spectra for different structured targets in figure 7.3 are depicted in relation to the mean flat foil spectrum. For all target types a two-temperature distribution is apparent for warm ($100-160$ MeV) and hot ($160-250$ MeV) electron energies. The corresponding Maxwell-Jüttner distributions obtained for each region are indicated by solid lines. The spectra show a modified production mechanism of highly energetic particles for the four structure types. A strong increase in the flux of low energetic electrons is visible.

Table 7.2 shows the mean electron temperature for the two regions and the relative spectral brightness. The latter is determined by identifying the maximum intensity value in the range observed, from 50 Mev to 200 Mev, and taking the average value and standard deviation for the according structure type.

Table 7.2.: Averaged spectral brightness and two-temperature distribution obtained from the electron spectra in figure 7.3. For needle targets in comparison to flat foils the electron number, i.e. spectral brightness increases by 300% while the mean temperatures stays comparable. For groove and pillar targets the spectral brightness decreases.

target type	**flat**	**groove**	**pillar**	**needle**
no. of shots	8	5	4	7
spectral brightness (a.u.)	1.0 ± 0.8	0.6 ± 0.2	0.7 ± 0.2	3.1 ± 1
mean electron temperature (MeV)	14	26	15	14
mean electron temperature (MeV)	26	20	23	27

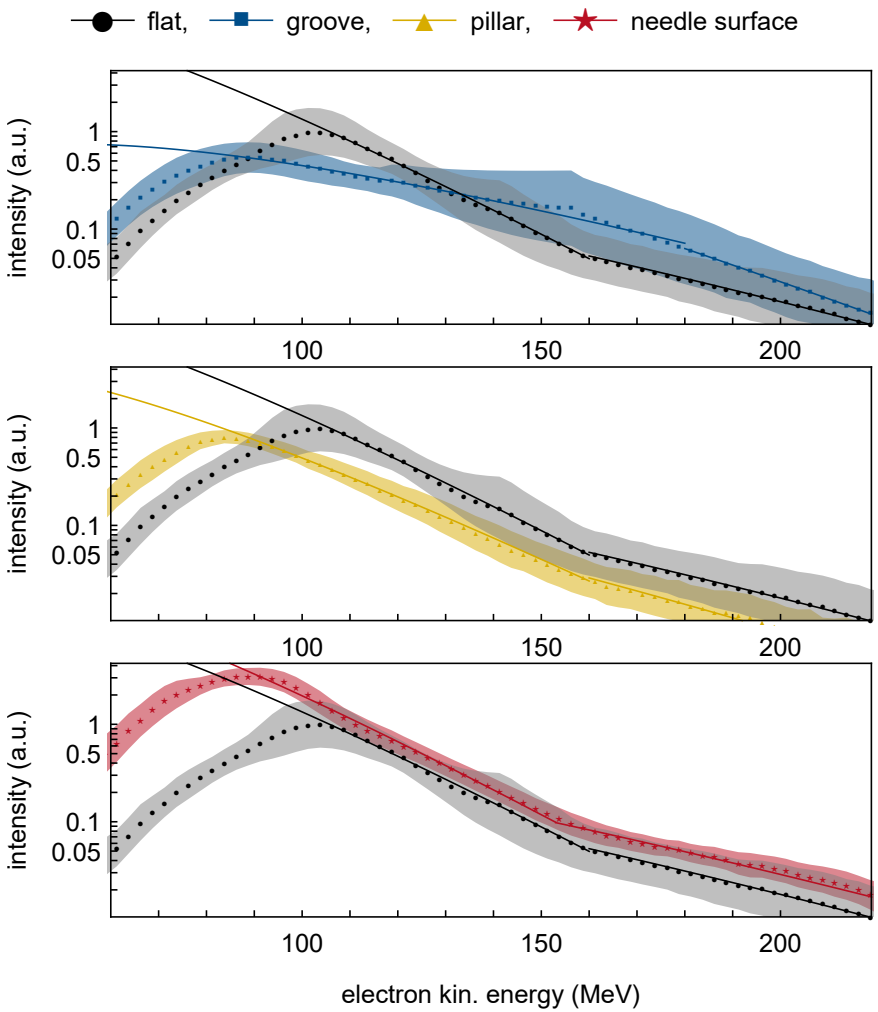

Figure 7.3.: Averaged electron spectrographs for the different structures in comparison to flat foils (black). The spectral distribution is approximated by Maxwell-Jüttner functions (lines). Two-temperature regions for warm ($100-160\,\mathrm{MeV}$) and hot ($160-250\,\mathrm{MeV}$) electrons are observed. The standard deviation of the averaged shots is shown as shaded regions. The spectral brightness using needle targets is increased by 300% in comparison to flat silicon targets.

Needle targets show a substantial increase for low energetic ($E_{\mathrm{kin}} \lesssim 120\,\mathrm{MeV}$) electrons in comparison to flat foils, increasing the spectral brightness by a factor of 3.1 ± 1, while the mean electron temperature is comparable between the two target types. These two observations suggest, that most of the additional laser energy absorbed by the needle targets is used for generating a higher flux of electrons, rather than affecting the temperature distribution. This means, that extreme field gradients are distributed over a larger area in comparison to flat targets. At the same time, the standard deviation of the mean electron spectrum for needle structures is smaller in comparison to the other targets and therefore provides a more reliable source of electrons.

For groove and pillar targets a decrease of spectral brightness is observed in comparison to flat targets. This is contradictory to the increased initial absorption of laser energy with these targets, suspected from the reflection measurements.

Looking at the spatial distribution of electrons emitted from the target backside with the angular wraparound stack in figure 7.4, a possible cause for the suppressed spectral brightness, measured with the electron spectrometer, for groove and pillar targets can be identified.

The angular position of laser axis (LA) and target backside normal (TN) are indicated for the four target types. The wraparound stack covers an angle of 120°. For flat and needle targets a broad emission of electrons around the interaction plane is observed with the strongest signal pointing in the direction of backside target normal. The spectrum for needle targets is thereby brighter.

For groove and pillar targets a rectangular feature around the pointing direction of backside target normal is visible. In addition, a bright edge near the laser axis is apparent. The cause of the rectangular feature can be found in the design of the target frame for pillar and needle targets (compare to section 5.2). On the target backside a $1 \times 1\mathrm{mm}^2$ frame is surrounding the centre of the structure embedded on the front side. Therefore, electrons are emitted particularly from the edges of the frame. The electron spectrum and distribution is heavily disturbed by these geometrical constraints.

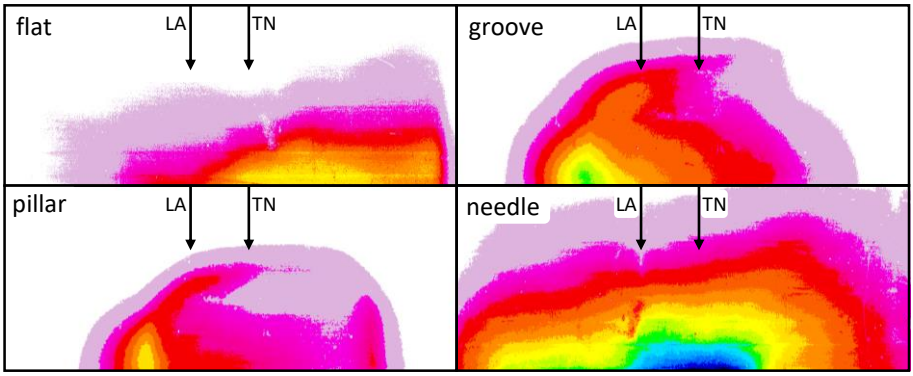

Figure 7.4.: The spatial distribution of electrons on the target backside is measured with a wraparound image plate stack for the four target types. The stack covers a solid angle of 120° around the target. The position of laser axis (LA) and target backside normal (TN) is illustrated (arrows). The spatial emission and flux of electrons from the backside is altered significantly when using structured front surfaces. In addition, for groove and pillar targets strong edge emission from the surrounding target frame is visible, disturbing the electron spectrum heavily.

7.3 Generation of X-ray radiation

High energetic electrons interacting with the target material will generate characteristic electromagnetic x-ray radiation, as well as bremsstrahlung. For an increased flux of electrons for structured targets, a stronger x-ray signal is expected. Here, characteristic transitions in silicon between 1.60 keV and 1.88 keV are observed.

The averaged X-ray spectra emitted from the target front for the three structure types is shown in figure 7.5, relative to flat targets. For groove and pillar targets, due to the low number of shots measured with the spectrometer, no standard deviation is given. In the spectra, the prominent characteristic transitions He_α (1), Li-like (2) and Ly_α (3) of silicon are shown. These spectral lines emerge from specific atomic transitions in the periphery plasma, surrounding the solid-density plasma (region within the laser spot).

The overall spectral brightness is enhanced using structured targets. This change is strongly dependent on the target type used. For grooved targets, the characteristic lines almost vanish in an increased background. For pillar and needle structures, these spectral lines sharpen, while the overall brightness increases. Table 7.3 summarises the spectral characteristics for the four target types in more detail.

Table 7.3.: Averaged information of the x-ray spectrum emitted from the front surface for the different target types. The overall brightness is shown together with the spectral brightness of the He_α transition. In addition, the ratio of the He_α and Ly_α line is an indicator for the strength of the initial interaction. The emission and transition strength from needle surfaces is dramatically increased in comparison to the other target types.

target type	**flat**	**groove**	**pillar**	**needle**
no. of shots	8	2	2	7
overall brightness (a.u.)	1.0	1.8	2.2	7.0
spectral brightness (a.u.)	1.0	1.2	3.2	16.5
He_α-Ly_α ratio	1.0	0.8	0.7	1.7

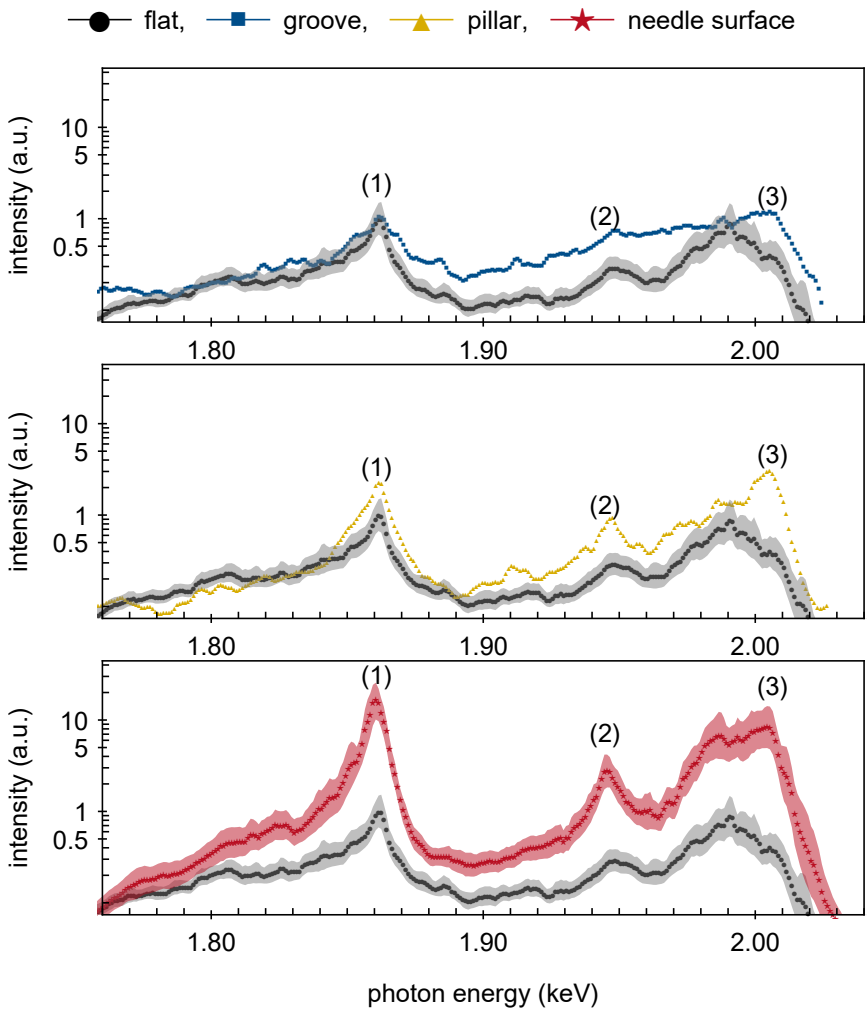

Figure 7.5.: Averaged X-ray spectra for different target structures in comparison to flat silicon foils (black) on a logarithmic scale. The three dominant transitions He_α (1), Li-like (2) and Ly_α (3) in silicon are indicated. Needle targets show a strong spectral increase of the signal. For flat and needle targets the standard deviation is indicated by shaded regions. For groove and pillar targets due to the low number of data points only the average signal is given.

The spectral brightness is amplified by a factor of 1.2 for groove, 3.2 for pillar and 16.5 for needle targets, respectively. Besides the observation of an increased brightness, the spectral intensity ratio of Ly_α (3) to He_α (1) is boosted by a factor of 1.7 for needle targets and decreased to 0.8 for groove and 0.7 for pillar structures. The ratio change for needle targets indicates, that the estimated radiation temperature is higher. Studies focussing on in-situ X-ray spectroscopy of ultra-intense laser-solid interactions suggest, that an enhancement in this spectral ratio emerges from a brighter X-ray source generated within the solid-density plasma.[114,115] The ratio decrease to 0.8 for groove and 0.7 for pillar targets implies that for these structures a lower radiation temperature is existent.

7.4 Acceleration of ions

The characteristics of ions emitted are dependent on the driving electric and magnetic fields and initial interaction of the laser pulse with the target. The front side structure thereby has a strong influence on the spatial and spectral energy distribution of ions. Furthermore, the distribution of electrons, as described in section 7.2, is the guiding factor for the characteristics of generated ions. Figure 7.6 shows the first three layers of radiochromic film for selected shots with the four target types. The first three layers of the RCF stack represent mean ion energies of 4.7 Mev (1), 8.2 Mev (2) and 11.3 Mev (3).
Thereby a strong dependency on the structure used is visible. In comparison to flat foils, experiments with groove and pillar structures the first layer of RCF shows a strong saturation. A dominant burst of low energetic ions is observed. For needle targets, a comparable spatial distribution to that of flat foils is visible. The total number of ions is thereby increased significantly. In the polarisation direction of the driving laser field a linear burst of ions is visible.
Figure 7.7 (left column) shows the averaged ion spectra derived from the RCF stacks for the different target types after a thorough conversion of the scan pictures to absolute ion numbers. The first five layers of the stack with energies between 5 MeV and 25 MeV are considered for this illustration. In addition, the regression of a Maxwell-Boltzmann distribution is shown together with the data points. From this, the average ion spectrum of the three target types in comparison to flat foils becomes clear. The energy distribution for groove and

[114] J. Colgan et al. *Phys. Rev. Lett.* **110**, 125001, 2013.
[115] S. B. Hansen et al. *Phys. Plasmas* **21**, 031213, 2014.

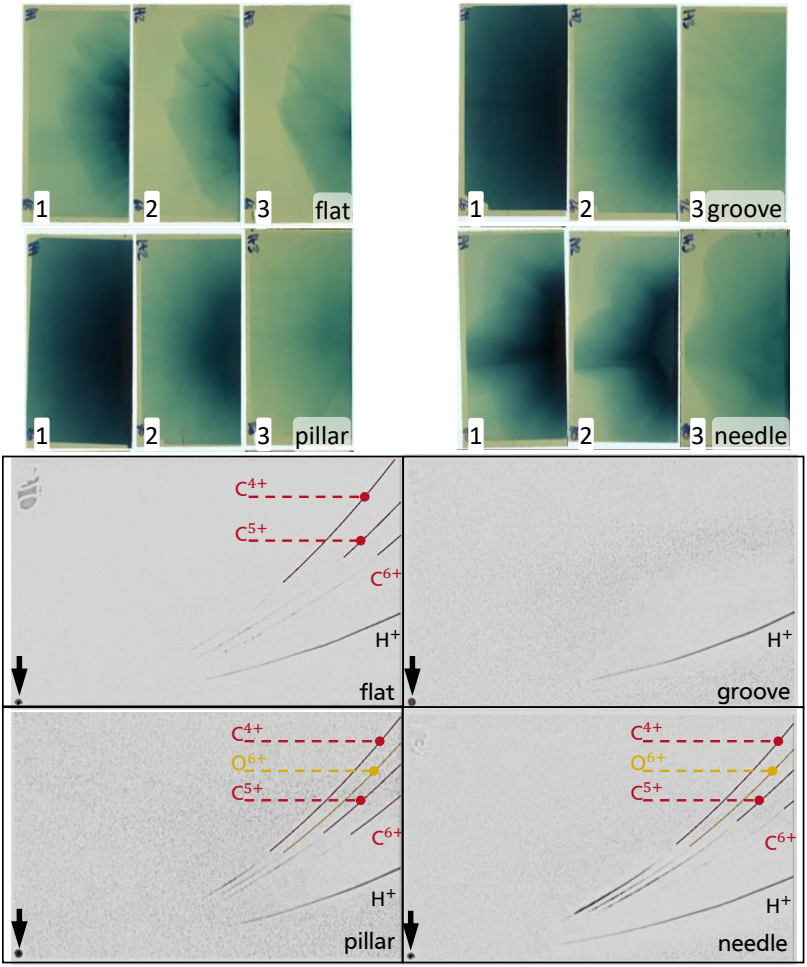

Figure 7.6.: Exemplary radiochromic film (RCF) data (top) and Thomson parabola traces (bottom) for the four target types. The first three layers of the RCF stack represent mean ion energies of $4.7\,\mathrm{Mev}$ (1), $8.2\,\mathrm{Mev}$ (2) and $11.3\,\mathrm{Mev}$ (3). A strong emission of low energetic particles by groove and pillar targets is observed. The overall brightness increases for needle structures in comparison to flat silicon foils. For the image plate scans (bottom) the zero point is indicated (arrows). Besides protons (H^+) carbon and oxygen ions are present for flat, pillar and needle targets. The latter target type demonstrates the highest ion and proton energies observed during the campaign.

Table 7.4.: Averaged measurements of ion numbers and energies for the different target types. The absolute number of ions in general and isolated protons above 4 MeV increases continuously, when changing the surface structure. The mean ion and proton temperature stays comparable between the target types with one exception: the temperature of hot protons from the needle target increases significantly by a factor of 4.

target type	**flat**	**groove**	**pillar**	**needle**
no. of shots	8	5	4	7
number of ions > 4 MeV ($\times 10^{11}$)	1.6	1.7	2.6	6.9
mean ion temperature (MeV)	2.9	3.5	1.9	2.7
relative number of protons > 4 MeV	1.0	1.9	1.8	3.2
mean 1st proton temperature (MeV)	1.8	2.2	2.1	2.3
mean 2nd proton temperature (MeV)	4.2	5.6	5.2	16.0

pillar targets is dominated by low energetic ions. Overall, no improvement in comparison to flat targets is evident. In contrast, needle structures show a similar mean ion temperature, whereas the overall amount of ions is significantly increased by a factor of 4.3. Fluctuations between shots in the spectrum are decreased considerably for needle targets, as indicated by the standard deviation (error bars).

The Thomson parabola, in contrast to the RCF stack, covers only a small fraction of the angular distribution of ions, but is able to analyse ion species with different charge-to-mass ratio (see section 6.6). Figure 7.7 (right column) shows the average proton spectrum for the different target types in relation to flat foils.

A two-temperature distribution of proton energies is visible that follows the general trend of flat targets. The transition to a secondary temperature distribution occurs at roughly 15 MeV. The approximated spectrum (solid lines) is shown together with the data points.

Table 7.4 shows extracted information from Maxwell-Boltzmann regression curves to RCF and Thomson spectra (figure 7.7). The general dynamic for groove and pillar structures is comparable to that of flat targets. The absolute particle number in the ion and proton spectra is slightly increased, whereas the

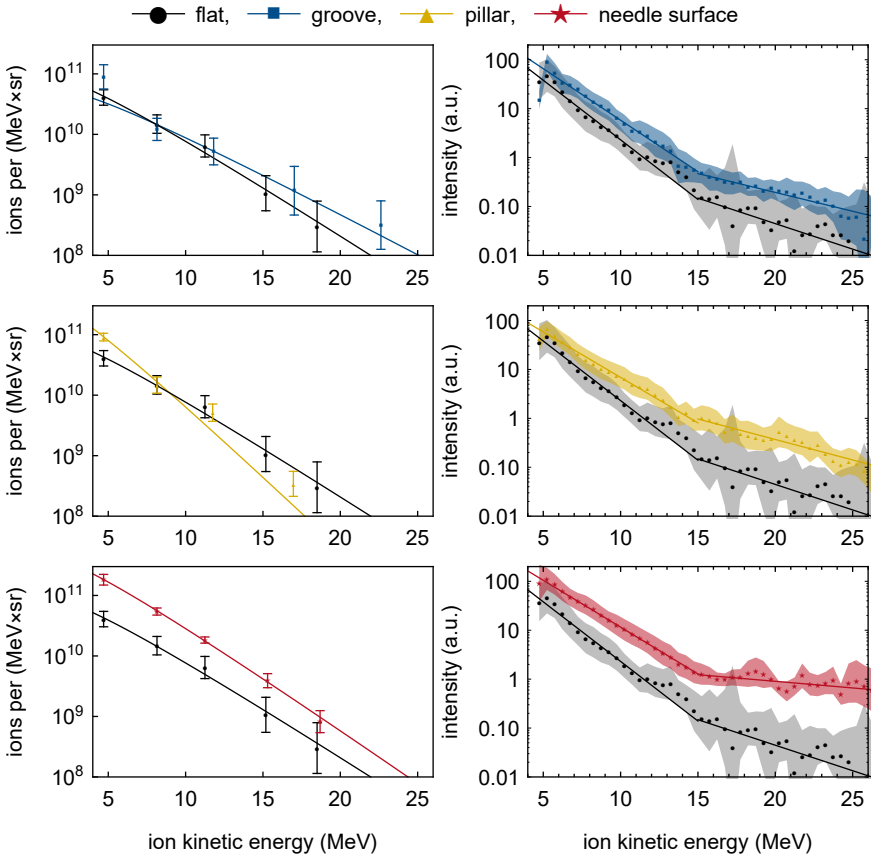

Figure 7.7.: Averaged spectral distribution of ions derived from the RCF stack (left column) and Thomson parabola ion spectrometer (right column). The first five layers of the RCF stack are considered for this illustration. It is shown together with the regression of a Maxwell-Boltzmann distribution for the different target types. The energy distribution for groove and pillar targets is dominated by low energy ions. For needle structures an increased yield of ions over the whole spectral range covered is visible. From the Thomson parabola traces the proton spectra are obtained and show a two-temperature distribution for all target types in contrast to the RCF stack (that covers all ion species present in the experiment within the first layers). The proton spectra is shown together with the according two-temperature Maxwell-Boltzmann distribution.

temperature is similar. In contrast, for needle targets an increase in the number of ions and an enhanced two-temperature distribution is observed.
A valuable addition to the proton spectra discussed above is the analysis of heavier ions (like carbon and oxygen). Figure 7.7 (right column) shows raw Thomson spectrometer traces for the four target types.
The zero point position is indicated on the bottom right. Flat targets show a dominant proton trace together with fully and partially ionised carbon (C^{6+}, C^{5+} and C^{4+}). For grooved targets only protons are visible. Using complex structures like pillar and needle, in addition to more carbon ions, ionised oxygen (O^{6+}) can be identified. For needle targets the number of protons and heavier ions is significantly enhanced.
In the Thomson spectra no silicon ions can be identified, which suggests that accelerated ions originate from a hydrogen and carbon rich contamination layer on the target backside and not from the bulk silicon. This contamination layer is always present on the target surface, without additional precautions.[52] Protons, being the highest charge-to-mass ratio ion species are always accelerated first, independently from the target material. Protons and ions from this layer are exposed to the highest field strengths and screen the field for ions from profound layers. The enhancement of energies for heavier ions represents a strong limitation of the proton spectrum, as only a limited number is present in the contamination layer. The estimated source size of ions and therefore the size of the contributing contamination volume is a key factor to understanding the ion dynamics presented here.

Source size and contamination

Attaching a copper mesh with a line spacing of 12.7 µm to the target backside frame imprints the mesh on the RCF stack and enables the estimation of the ion source size. The mesh thereby has a distance of 560 µm to the target backside surface from where the ions are emitted. The projection of the mesh lines onto the RCF is shown in figure 7.8 for flat and needle targets.
For flat foils, approximately 23 lines, for needle targets 26 lines are visible on the film. Therefore, a diameter of 287 µm (flat) and 332 µm (needle) of the mesh is illuminated. For flat, the proton signal covers a circle with diameter of approximately 40.2 mm on the RCF, for needle 43.0 mm, respectively. With the distance of RCF stack to the target front of 80 mm, the source size diameter is estimated to be (25 ± 10)µm for flat and (100 ± 10)µm for needle targets.

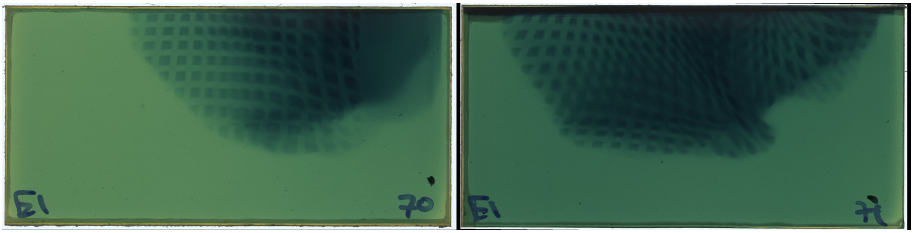

Figure 7.8.: Radiochromic films from source size estimation measurements. A thin copper mesh was attached to the target backside frame for a shot on a flat target (left) and a shot on a needle target (right). From the scanned RCF together with the position and spacing of the mesh the source size and divergence angle can be approximated.

The opening angle of the protons emitted accounts to 28° for flat and 30° for needle targets.
The estimation of source size (and opening angle) is strongly dependent on the distance of the considered RCF layer to the copper mesh. If available, the choice of two parallel meshes with a skewed orientation eliminates the RCF distance from the calculation. With a well-known separation between the two meshes, a more precise estimate for the source size is feasible.
From the source size calculation, the number of available protons on the target backside can be assessed. With an estimated contamination layer density of $(4 \pm 1) \times 10^{16}$ protons/cm^2,[52] the number of protons in the contamination layer accounts to $(2 \pm 1) \times 10^{11}$ protons/cm^2 for flat targets and $(3 \pm 1) \times 10^{12}$ protons/cm^2 for needle structures in agreement with the number of ions observed in the experiment. Here, the conversion efficiency is thus significantly limited by the amount of protons present on the target backside.

7.5 Conclusion

A broad and consistent picture of the influences of different microstructured target types on the laser incident surface can be painted with the discussion of the data points shown above. The needle structures created here outperformed other target types substantially. The direct reflection of laser energy from the target is decreased and the electromagnetic spectrum reflected and scattered into the target chamber is decreased over the full spectral range observed.

Obviously, a significant amount of energy is absorbed to generate and push energetic electrons into the target bulk. As a result of an increased surface area interacting with the driving laser field using this structure, a higher number of electrons is observed. Ideal conditions for the directed acceleration of energetic protons are generated. In the experiment the number and mean temperature of hot protons is increased, even so the achievable number of protons is limited by the contamination layer on the target backside. At the same time, using needle structures the emission of X-ray lines from transitions in the solid-density and periphery plasma is enhanced. The spectral brightness of the characteristic He_α line increases.

8 Summary and prospects

Core and motivation of this thesis was to investigate on the influence of surfaces with increased light absorption to intense laser-plasma experiments. Therefore, the scientific basis and fundamental research in the field of laser-plasma experiments as well as the fabrication of highly light absorbing structures was presented in chapter 2.

Inspired by the elaborate research of the group around ERIC MAZUR at the *Harvard University Department of Physics*,[6,9,25,26,38,70,71] an experimental setup for the fabrication of microstructured silicon surfaces was developed within the framework of this work and presented in chapter I. The underlying technique utilises the unique properties of ultra-short femtosecond laser pulses to ablate materials from a cold silicon lattice. This system can operate with a variety of processing substances and parameter ranges.

With a successful proof of principle and characterisation of the fabrication system in the laboratory, first steps have been taken to further optimise and employ the system to applications.

Structured targets have been produced for a high power experimental campaign at the *Vulcan* laser system of the *Central Laser Facility*, Oxfordshire, UK. They are compared to flat silicon foils and differently structured targets. Motivated by the author, this campaign focussed on the influence of these structures on the acceleration of particles and generation of highly intense radiation. The planning and preparation of this campaign, presented in chapter 5, demonstrated the complex experimental setup necessary to measure reflection and emission of light, generation of energetic electrons, X-ray radiation and the acceleration of ions at the same time. The production and requirements of the different target designs were explained.

The laser contrast and intensity have been shown to be a critical parameter for the investigation of effects by an unmodified surface structure. Peak intensities before the main laser pulse arrives on the target are typically enough to dramatically alter the shape and temperature of the target without additional means. Here, a double plasma mirror system was designed and used to generate a high temporal contrast of the main laser pulse intensity to perturbations

without confining the experimental conditions too much or overcomplicating the setup and use of diagnostics.
The experimental setup designed and successfully used for the campaign was presented in chapter 6. Eleven main diagnostic setups were used to generate a complete as possible picture of the central interaction of the laser pulse with the target. Thereby, diagnostics for reflected and scattered laser light, spatial and spectral distribution of electrons, ions and X-ray radiation were considered. The working principle and exemplary data acquisition for these measurement techniques were illustrated.
With the run of a beamtime over six weeks a substantial number of 115 laser shots on targets with different microstructures was performed. The discussion and evaluation of the data points (chapter 7) for the four different target types used (flat, groove, pillar, needle) shows a significant performance of the targets developed within the framework of this thesis in comparison to existing target designs. The reflection and scatter of light from the laser incident surface of the target was shown to decrease over the broad spectral range covered. As a result, a higher flux of energetic electrons is present and enables supreme conditions for the acceleration of ions and generation of X-ray radiation. The spectral brightness of the characteristic X-ray transitions observed increases by orders of magnitude for needle targets. A higher number of protons and different carbon and oxygen ions are observed with higher kinetic energies. Furthermore, it was shown that the efficient acceleration of ions from the target backside was limited by the number of protons and contamination ions available for acceleration.
A promising optimisation for future experiments is the deliberate addition of a proton-rich layer to the target backside. With this, the performance of these structured targets for the acceleration of ions is most likely increased dramatically. Therefore, advanced techniques for the characterisation of the ion source size and collimation are suggested here. A reliable source of intense X-ray photons could be generated by adding a confined region of copper or tungsten to the target backside. Thence, a brilliant point-like source of characteristic X-ray radiation could become available. For future experiments, the investigation of the characteristic K_α line of the material, as well as the bremsstrahlung spectrum is strongly recommended. In addition, mass limitation of the target and removing the supporting frame from the silicon membranes is advised.
Further optimisation and evaluation of the fabrication system for the production of targets for high repetition rate laser facilities could solve the issue we face in target supply for these experiments today. With the single exposure

setup employing custom shaped intensity profiles for the structuring process the full production time for a single structured silicon target could be reduced to 100 ms. Thereby, the production of structured solid targets with a repetition rate of 10 Hz is in reach. A further automation of the fabrication system is recommended.
In addition, structures on materials other than silicon in combination with a variety of process substances should be investigated for possible applications not only in laser-driven acceleration experiments. Already today, the successful application of microstructured silicon and functional surfaces has been demonstrated in a range of fields.
In summary, with the results of this thesis a prosperous influence of microstructured surfaces with increased light absorption to the field of intense laser-plasma experiments has been demonstrated.

Bibliography

[1] J.-N. Wang, Y.-Q. Liu, Y.-L. Zhang, J. Feng, and H.-B. Sun. Pneumatic smart surfaces with rapidly switchable dominant and latent superhydrophobicity. *Nat. Publ. Gr.* **10**, e470, 2018. doi: 10.1038/am.2017.218 (see p. 11).

[2] N. Li, E. Xu, Z. Liu, X. Wang, and L. Liu. Tuning apparent friction coefficient by controlled patterning bulk metallic glasses surfaces. *Sci. Rep.* **6**, 39388, 2016. doi: 10.1038/srep39388 (see p. 11).

[3] D. Berman, B. Narayanan, M. J. Cherukara, S. K.R.S. Sankaranarayanan, A. Erdemir, A. Zinovev, and A. V. Sumant. Operando tribochemical formation of onion-like-carbon leads to macroscale superlubricity. *Nat. Commun.* **9**, 1164, 2018. doi: 10.1038/s41467-018-03549-6 (see p. 11).

[4] L. Wang, M. S. H. Boutilier, P. R. Kidambi, D. Jang, N. G. Hadjiconstantinou, and R. Karnik. Fundamental transport mechanisms, fabrication and potential applications of nanoporous atomically thin membranes. *Nat. Nanotechnol.* **12**, 509–522, 2017. doi: 10.1038/nnano.2017.72 (see p. 11).

[5] M. Malinauskas, A. Žukauskas, S. Hasegawa, Y. Hayasaki, V. Mizeikis, R. Buividas, and S. Juodkazis. Ultrafast laser processing of materials: from science to industry. *Light Sci. Appl.* **5**, e16133, 2016. doi: 10.1038/lsa.2016.133 (see p. 11, 12).

[6] C. Wu, C. H. Crouch, L. Zhao, J. E. Carey, R. Younkin, J. A. Levinson, E. Mazur, R. M. Farrell, P. Gothoskar, and A. Karger. Near-unity below-band-gap absorption by microstructured silicon. *Appl. Phys. Lett.* **78**, 1850–1852, 2001. doi: 10.1063/1.1358846 (see p. 11, 42, 137).

[7] S. Kontermann, T. Gimpel, A. L. Baumann, K. M. Guenther, and W. Schade. Laser processed black silicon for photovoltaic applications. *Energy Procedia* **27**, 390–395, 2012. doi: 10.1016/j.egypro.2012.07.082 (see p. 11, 42).

[8] J. Lv, T. Zhang, P. Zhang, Y. Zhao, and S. Li. Review Application of Nanostructured Black Silicon. *Nanoscale Res. Lett.* **13**, 110, 2018. doi: 10.1186/s11671-018-2523-4 (see p. 11).

[9] Z. Huang, J. E. Carey, M. Liu, X. Guo, E. Mazur, and J. C. Campbell. Microstructured silicon photodetector. *Appl. Phys. Lett.* **89**, 033506, 2006. doi: 10.1063/1.2227629 (see p. 11, 42, 137).

[10] M. Borghesi, J. Fuchs, S. V. Bulanov, A. J. MacKinnon, P. K. Patel, and M. Roth. Fast Ion Generation by High-Intensity Laser Irradiation of Solid Targets and Applications. *Fusion Sci. Technol.* **49**, 412–439, 2006. doi: 10.13182/FST06-A1159 (see p. 11, 40).

[11] S. C. Wilks and W. L. Kruer. Absorption of ultrashort, ultra-intense laser light by solids and overdense plasmas. *IEEE J. Quantum Electron.* **33**, 1954–1968, 1997. doi: 10.1109/3.641310 (see p. 11, 35).

[12] G. A. Mourou, T. Tajima, and S. V. Bulanov. Optics in the relativistic regime. *Rev. Mod. Phys.* **78**, 309–371, 2006. doi: 10.1103/RevModPhys.78.309 (see p. 11, 40).

[13] H. Daido, M. Nishiuchi, and A. S. Pirozhkov. Review of laser-driven ion sources and their applications. *Reports Prog. Phys.* **75**, 056401, 2012. doi: 10.1088/0034-4885/75/5/056401 (see p. 11, 40).

[14] A. Macchi, M. Borghesi, and M. Passoni. Ion acceleration by super-intense laser-plasma interaction. *Rev. Mod. Phys.* **85**, 751–793, 2013. doi: 10.1103/RevModPhys.85.751 (see p. 11, 37, 38, 40).

[15] I. Prencipe, J. Fuchs, S. Pascarelli, D. W. Schumacher, R. B. Stephens, N. B. Alexander, R. Briggs, M. Büscher, M. O. Cernaianu, A. Choukourov, M. De Marco, A. Erbe, J. Fassbender, G. Fiquet, P. Fitzsimmons, C. Gheorghiu, J. Hund, L. G. Huang, M. Harmand, N. J. Hartley, A. Irman, T. Kluge, Z. Konopkova, S. Kraft, D. Kraus, V. Leca, D. Margarone, J. Metzkes, K. Nagai, W. Nazarov, P. Lutoslawski, D. Papp, M. Passoni, A. Pelka, J. P. Perin, J. Schulz, M. Smid, C. Spindloe, S. Steinke, R. Torchio, C. Vass, T. Wiste, R. Zaffino, K. Zeil, T. Tschentscher, U. Schramm, and T. E. Cowan. Targets for high repetition rate laser facilities: Needs, challenges and perspectives. *High Power Laser Sci. Eng.* **5**, e17, 2017. doi: 10.1017/hpl.2017.18 (see p. 12, 40).

[16] O. KLIMO, J. PSIKAL, J. LIMPOUCH, J. PROSKA, F. NOVOTNY, T. CECCOTTI, V. FLOQUET, and S. KAWATA. Short pulse laser interaction with micro-structured targets: Simulations of laser absorption and ion acceleration. *New J. Phys.* **13**, 053028, 2011. DOI: 10.1088/1367-2630/13/5/053028 (see p. 12, 40).

[17] G. CRISTOFORETTI, P. LONDRILLO, P. K. SINGH, F. BAFFIGI, G. D'ARRIGO, A. D. LAD, R. G. MILAZZO, A. ADAK, M. SHAIKH, D. SARKAR, G. CHATTERJEE, J. JHA, M. KRISHNAMURTHY, G. R. KUMAR, and L. A. GIZZI. Transition from Coherent to Stochastic electron heating in ultrashort relativistic laser interaction with structured targets. *Sci. Rep.* **7**, 1479, 2017. DOI: 10.1038/s41598-017-01677-5 (see p. 12, 40).

[18] A. LÜBCKE, A. A. ANDREEV, S. HÖHM, R. GRUNWALD, L. EHRENTRAUT, and M. SCHNÜRER. Prospects of target nanostructuring for laser proton acceleration. *Sci. Rep.* **7**, 44030, 2017. DOI: 10.1038/srep44030 (see p. 12).

[19] Z. ZHAO, L. CAO, L. CAO, J. WANG, W. HUANG, W. JIANG, Y. HE, Y. WU, B. ZHU, K. DONG, Y. DING, B. ZHANG, Y. GU, M. Y. YU, and X. T. HE. Acceleration and guiding of fast electrons by a nanobrush target. *Phys. Plasmas* **17**, 123108, 2010. DOI: 10.1063/1.3507292 (see p. 12).

[20] L. C. JARROTT, A. J. KEMP, L. DIVOL, D. MARISCAL, B. WESTOVER, C. MCGUFFEY, F. N. BEG, M. SUGGIT, C. CHEN, D. HEY, B. MADDOX, J. HAWRELIAK, H. S. PARK, B. REMINGTON, M. S. WEI, and A. MACPHEE. Kα and bremsstrahlung x-ray radiation backlighter sources from short pulse laser driven silver targets as a function of laser pre-pulse energy. *Phys. Plasmas* **21**, 031211, 2014. DOI: 10.1063/1.4865230 (see p. 12).

[21] W. YAN, C. FRUHLING, G. GOLOVIN, D. HADEN, J. LUO, P. ZHANG, B. ZHAO, J. ZHANG, C. LIU, M. CHEN, S. CHEN, S. BANERJEE, and D. UMSTADTER. High-order multiphoton Thomson scattering. *Nat. Photonics* **11**, 514–520, 2017. DOI: 10.1038/nphoton.2017.100 (see p. 12).

[22] F. RÁKSI, K. R. WILSON, Z. JIANG, A. IKHLEF, C. Y. CÔTÉ, and J.-C. KIEFFER. Ultrafast x-ray absorption probing of a chemical reaction. *J. Chem. Phys.* **104**, 6066–6069, 1996. DOI: 10.1063/1.471305 (see p. 12).

[23] K. SUGIOKA and Y. CHENG. Ultrafast lasers-reliable tools for advanced materials processing. *Light Sci. Appl.* **3**, e149, 2014. DOI: 10.1038/lsa.2014.30 (see p. 12).

[24] J. Bonse, S. Höhm, S. Kirner, A. Rosenfeld, and J. Krüger. Laser-induced Periodic Surface Structures (LIPSS) - A Scientific Evergreen. *Conf. Lasers Electro-Optics* **23**, 9000615, 2016. DOI: 10.1364/CLEO_SI.2016.STh1Q.3 (see p. 12, 41).

[25] T. H. Her, R. J. Finlay, C. Wu, S. Deliwala, and E. Mazur. Microstructuring of silicon with femtosecond laser pulses. *Appl. Phys. Lett.* **73**, 1673–1675, 1998. DOI: 10.1063/1.122241 (see p. 12, 23, 41, 43, 137).

[26] M. A. Sheehy, L. Winston, J. E. Carey, C. M. Friend, and E. Mazur. Role of the background gas in the morphology and optical properties of laser-microstructured silicon. *Chem. Mater.* **17**, 3582–3586, 2005. DOI: 10.1021/cm049029i (see p. 12, 41, 42, 45, 80, 137).

[27] M. Wollenhaupt, A. Assion, and T. Baumert. Springer Handbook of Lasers and Optics. 2012. 1047–1094 DOI: 10.1007/978-3-642-19409-2_12 (see p. 18–24, 27, 59).

[28] J. C. Diels and W. Rudolph. Ultrashort Laser Pulse Phenomena. Elsevier, 2006. DOI: 10.1016/B978-012215493-5/50021-5 (see p. 18–20, 22–24, 59).

[29] M. Lax, W. H. Louisell, and W. B. McKnight. From Maxwell to paraxial wave optics. *Phys. Rev. A* **11**, 1365–1370, 1975. DOI: 10.1103/PhysRevA.11.1365 (see p. 20).

[30] *Lasers and laser-related equipment — Test methods for laser beam widths, divergence angles and beam propagation ratios — Part 2: General astigmatic beams*. Standard Geneva, CH: International Organization for Standardization., 2005 (see p. 22).

[31] E. G. Gamaly and A. V. Rode. Physics of ultra-short laser interaction with matter: From phonon excitation to ultimate transformations. *Prog. Quantum Electron.* **37**, 215–323, 2013. DOI: 10.1016/j.pquantelec.2013.05.001 (see p. 24, 30).

[32] Tina Ebert. Homogeneous Surface Structuring of Silicon with Ultrashort Laser Pulses. Master Thesis. Technische Universität Darmstadt, 2017. (see p. 24, 68, 69, 72–74, 77, 79–81).

[33] T. H. Maiman. Stimulated optical radiation in Ruby. *Nature* **187**, 493–494, 1960. DOI: 10.1038/187493a0 (see p. 24, 41).

[34] D. E. SPENCE, P. N. KEAN, and W. SIBBETT. 60-fsec pulse generation from a self-mode-locked Ti:sapphire laser. *Opt. Lett.* **16**, 42, 1991. DOI: 10.1364/OL.16.000042 (see p. 24, 39).

[35] F SALIN, J SQUIER, and M PICHÉ. Mode locking of Ti:AI(2)O(3) lasers and self-focusing: a Gaussian approximation. *Opt. Lett.* **16**, 1674–1676, 1991. DOI: 10.1364/OL.16.001674 (see p. 24).

[36] M. L. M. BALISTRERI. Tracking Femtosecond Laser Pulses in Space and Time. *Science (80-.).* **294**, 1080–1082, 2001. DOI: 10.1126/science.1065163 (see p. 24).

[37] P. CORKUM and R. L. DAVIS. Attosecond pulses at last. *Nature* **403**, 845–846, 2000. DOI: 10.1038/35002711 (see p. 24, 39).

[38] S. K. SUNDARAM and E. MAZUR. Inducing and probing non-thermal transitions in semiconductors using femtosecond laser pulses. *Nat. Mater.* **1**, 217–224, 2002. DOI: 10.1038/nmat767 (see p. 24, 30–32, 137).

[39] H. FROWEIN. Titan-Saphir Laser. *Opt. Photonik* **1**, 48–53, 2007. (see p. 24, 26, 27).

[40] K. F. RENK. Basics of Laser Physics: For Students of Science and Engineering. 2nd ed. Graduate Texts in Physics, Springer, 2012. (see p. 25–27).

[41] P. F. MOULTON. Spectroscopic and laser characteristics of Ti:Al_2O_3. *J. Opt. Soc. Am. B* **3**, 125, 1986. DOI: 10.1364/JOSAB.3.000125 (see p. 25, 39).

[42] C. RULLIÈRE. Femtosecond Laser Pulses: Principles and Experiments. 2nd ed. Springer, 2005. (see p. 26, 27).

[43] D. STRICKLAND and G. MOUROU. Compression of amplified chirped optical pulses. *Opt. Commun.* **55**, 447–449, 1985. DOI: 10.1016/0030-4018(85)90151-8 (see p. 28, 39).

[44] A. VAUPEL, N. BODNAR, B. WEBB, L. SHAH, and M. RICHARDSON. Concepts, performance review, and prospects of table-top, few-cycle optical parametric chirped-pulse amplification. *Opt. Eng.* **53**, 051507, 2013. DOI: 10.1117/1.OE.53.5.051507 (see p. 28).

[45] Eugene HECHT. Optik. 6., De Gruyter, 2014. (see p. 29, 30, 52).

[46] M. A. GREEN. Self-consistent optical parameters of intrinsic silicon at 300K including temperature coefficients. *Sol. Energy Mater. Sol. Cells* **92**, 1305–1310, 2008. DOI: 10.1016/j.solmat.2008.06.009 (see p. 30, 31).

[47] A. PIEL. Plasma Physics: An Introduction to Laboratory, Space, and Fusion Plasmas. 2nd ed. Springer, 2017. (see p. 33, 34, 112).

[48] P. MULSER and D. BAUER. High Power Laser-Matter Interaction. 2nd ed. Springer, 2010. DOI: 10.1007/978-3-540-46065- (see p. 33, 35).

[49] W. L. KRUER and K. ESTABROOK. J×B heating by very intense laser light. *Phys. Fluids* **28**, 430–432, 1985. DOI: 10.1063/1.865171 (see p. 36, 37).

[50] B. BEZZERIDES, S. J. GITOMER, and D. W. FORSLUND. Randomness, maxwellian distributions, and resonance absorption. *Phys. Rev. Lett.* **44**, 651–654, 1980. DOI: 10.1103/PhysRevLett.44.651 (see p. 37).

[51] F. JÜTTNER. Das Maxwellsche Gesetz der Geschwindigkeitsverteilung in der Relativtheorie. *Annalen der Physik* **339**, 856–882, 1911. DOI: 10.1002/andp.19113390503 (see p. 37).

[52] G. HOFFMEISTER, C. BELLEI, K. HARRES, D. IVANOV, D. KRAUS, A. PELKA, B. RETHFELD, G. SCHAUMANN, and M. ROTH. Influence of fs-laser desorption on target normal sheath accelerated ions. *Phys. Rev. Spec. Top. - Accel. Beams* **16**, 041304, 2013. DOI: 10.1103/PhysRevSTAB.16.041304 (see p. 38, 134, 135).

[53] V. I. VEKSLER. The principle of coherent acceleration of charged particles. *Sov. J. At. Energy* **2**, 525–528, 1957. DOI: 10.1007/BF01491001 (see p. 39).

[54] N. SARUKURA, Y. ISHIDA, and H. NAKANO. Generation of 50-fsec pulses from a pulse-compressed, cw, passively mode-locked Ti:sapphire laser. *Opt. Lett.* **16**, 153–155, 1991. DOI: 10.1364/OL.16.000153 (see p. 39).

[55] R. A. SNAVELY, M. H. KEY, S. P. HATCHETT, T. E. COWAN, M. ROTH, T. W. PHILLIPS, M. A. STOYER, E. A. HENRY, T. C. SANGSTER, M. S. SINGH, S. C. WILKS, A. MACKINNON, A. OFFENBERGER, D. M. PENNINGTON, K. YASUIKE, A. B. LANGDON, B. F. LASINSKI, J. JOHNSON, M. D. PERRY, and E. M. CAMPBELL. Intense High-Energy Proton Beams from Petawatt-Laser Irradiation of Solids. *Phys. Rev. Lett.* **85**, 2945–2948, 2000. DOI: 10.1103/PhysRevLett.85.2945 (see p. 39).

[56] E. L. Clark, K. Krushelnick, M. Zepf, F. N. Beg, M. Tatarakis, A. Machacek, M. I. K. Santala, I. Watts, P. A. Norreys, and A. E. Dangor. Energetic Heavy-Ion and Proton Generation from Ultraintense Laser-Plasma Interactions with Solids. *Phys. Rev. Lett.* **85**, 1654–1657, 2000. DOI: 10.1103/PhysRevLett.85.1654 (see p. 39).

[57] A. Maksimchuk, S. Gu, K. Flippo, D. Umstadter, and V. Y. Bychenkov. Forward Ion Acceleration in Thin Films Driven by a High-Intensity Laser. *Phys. Rev. Lett.* **84**, 4108–4111, 2000. DOI: 10.1103/PhysRevLett.84.4108 (see p. 39).

[58] H. Daido. Review of soft x-ray laser researches and developments. *Reports Prog. Phys.* **65**, 1513, 2002. DOI: 10.1088/0034-4885/65/10/204 (see p. 39).

[59] E. Esarey, C. B. Schroeder, and W. P. Leemans. Physics of laser-driven plasma-based electron accelerators. *Rev. Mod. Phys.* **81**, 1229–1285, 2009. DOI: 10.1103/RevModPhys.81.1229 (see p. 39).

[60] V. Malka, J. Faure, Y. A. Gauduel, E. Lefebvre, A. Rousse, and K. T. Phuoc. Principles and applications of compact laser-plasma accelerators. *Nat. Phys.* **4**, 447–453, 2008. DOI: 10.1038/nphys966 (see p. 40).

[61] H. Habara, S. Honda, M. Katayama, H. Sakagami, K. Nagai, and K. A. Tanaka. Efficient energy absorption of intense ps-laser pulse into nanowire target. *Phys. Plasmas* **23**, 063105, 2016. DOI: 10.1063/1.4953092 (see p. 40).

[62] K. A. Ivanov, A. V. Brantov, S. I. Kudryashov, S. V. Makarov, D. A. Gozhev, R. V. Volkov, A. A. Ionin, V. Yu Bychenkov, and A. B. Savelev. Enhanced relativistic laser-plasma coupling utilizing laser-induced micromodified target. *Laser Phys. Lett.* **12**, 046005, 2015. DOI: 10.1088/1612-2011/12/4/046005 (see p. 40).

[63] L. Cao, M. Chen, Z. Zhao, H. Cai, S. Wu, Y. Gu, W. Yu, M. Y. Yu, and X. T. He. Efficient laser absorption and enhanced electron yield in the laser-target interaction by using a cone-nanolayer target. *Phys. Plasmas* **18**, 054501, 2011. DOI: 10.1063/1.3589303 (see p. 40).

[64] M. C. Levy, S. C. Wilks, M. Tabak, S. B. Libby, and M. G. Baring. Petawatt laser absorption bounded. *Nat. Commun.* **5**, 4149, 2014. DOI: 10.1038/ncomms5149 (see p. 40).

[65] S. JIANG, A. G. KRYGIER, D. W. SCHUMACHER, K. U. AKLI, and R. R. FREEMAN. Effects of front-surface target structures on properties of relativistic laser-plasma electrons. *Phys. Rev. E - Stat. Nonlinear, Soft Matter Phys.* **89**, 013106, 2014. DOI: 10.1103/PhysRevE.89.013106 (see p. 40).

[66] S. JIANG, A. G. KRYGIER, D. W. SCHUMACHER, K. U. AKLI, and R. R. FREEMAN. Enhancing Bremsstrahlung production from ultraintense laser-solid interactions with front surface structures. *Eur. Phys. J. D* **68**, 283, 2014. DOI: 10.1140/epjd/e2014-50339-4 (see p. 40).

[67] G. KULCSAR, D. AL MAWLAWI, F. W. BUDNIK, P. R. HERMAN, M. MOSKOVITS, L. ZHAO, and R. S. MARJORIBANKS. Intense picosecond x-ray pulses from laser plasmas by use of nanostructured velvet targets. *Phys. Rev. Lett.* **84**, 5149–5152, 2000. DOI: 10.1103/PhysRevLett.84.5149 (see p. 40).

[68] M. BIRNBAUM. Semiconductor surface damage produced by Ruby lasers. *J. Appl. Phys.* **36**, 3688–3689, 1965. DOI: 10.1063/1.1703071 (see p. 41).

[69] H. M. VAN DRIEL, J. E. SIPE, and J. F. YOUNG. Laser-induced periodic surface structure on solids: A universal phenomenon. *Phys. Rev. Lett.* **49**, 1955–1958, 1982. DOI: 10.1103/PhysRevLett.49.1955 (see p. 41).

[70] R. YOUNKIN, J. E. CAREY, E. MAZUR, J. A. LEVINSON, and C. M. FRIEND. Infrared absorption by conical silicon microstructures made in a variety of background gases using femtosecond-laser pulses. *J. Appl. Phys.* **93**, 2626–2629, 2003. DOI: 10.1063/1.1545159 (see p. 42, 137).

[71] T. H. HER, R. J. FINLAY, C. WU, and E. MAZUR. Femtosecond laser-induced formation of spikes on silicon. *Appl. Phys. A Mater. Sci. Process.* **70**, 383–385, 2000. DOI: 10.1007/s003390051052 (see p. 42, 80, 82, 83, 137).

[72] X. LIU, P. R. COXON, M. PETERS, B. HOEX, J. M. COLE, and D. J. FRAY. Black silicon: fabrication methods, properties and solar energy applications. *Energy Environ. Sci.* **7**, 3223–3263, 2014. DOI: 10.1039/C4EE01152J (see p. 42).

[73] M. U. Pralle, J. E. Carey, H. Haddad, C. Vineis, J. Sickler, X. Li, J. Jiang, F. Sahebi, C. Palsule, and J. McKee. IR CMOS: infrared enhanced silicon imaging. *Proc. SPIE* **8704**, 8704 –8704 –7, 2013. DOI: 10.1117/12.2015959 (see p. 42).

[74] Griffin - Ultrafast Ti:sapphire oscillator series. KMLabs Inc. URL: https://kmlabs.com/wp-content/uploads/2017/02/km_labs_Griffin_datasheet_180125.pdf (accessed 01 April 2018) (see p. 52).

[75] Ti:sapphire - Ultrafast amplifiers. Quantronix Corp. URL: http://www.quantron.com/files/dl/Integra-C%20v8.pdf (accessed 01 April 2018) (see p. 54).

[76] Handbuch SAM 10800 und 108003 S10 analog SSV10. SCANLAB AG. 2018-04-01 URL: http://www.scanlab.de/en/downloads/data-sheets (see p. 58, 66).

[77] R. Boyd. Nonlinear Optics. 3rd ed. Academic Press, 2008. DOI: 10.1016/B978-0-12-369470-6.00011-3 (see p. 59, 122).

[78] B. Schwarz, G. Ritt, M. Koerber, and B. Eberle. Laser-induced damage threshold of camera sensors and micro-optoelectromechanical systems. *Opt. Eng.* **56**, 034108, 2017. DOI: 10.1117/1.OE.56.3.034108 (see p. 62).

[79] UI-1220LE-M-GL (AB.0010.1.25600.23). IDS Imaging Development Systems GmbH. URL: https://de.ids-imaging.com/IDS/datasheet_pdf.php?sku=AB.0010.1.25600.23 (accessed 01 April 2018) (see p. 62).

[80] L. D. Geulig. Diffraktive optische Strahlformung zur homogenen Strukturierung von Oberflächen mittels ultrakurzer Laserpulse. Bachelor Thesis. Technische Universität Darmstadt, 2018. (see p. 63, 64).

[81] P. M. Celliers, K. G. Estabrook, R. J. Wallace, J. E. Murray, L. B. Da Silva, B. J. MacGowan, B. M. Van Wonterghem, and K. R. Manes. Spatial filter pinhole for high-energy pulsed lasers. *Appl. Opt.* **37**, 2371, 1998. DOI: 10.1364/AO.37.002371 (see p. 63).

[82] Technical Note: Spatial Filters. Newport Corporation. URL: https://www.newport.com/n/spatial-filters (accessed 01 April 2018) (see p. 63).

[83] H. ZHANG, C. LI, E. BEVILLON, G. CHENG, J. P. COLOMBIER, and R. STOIAN. Ultrafast destructuring of laser-irradiated tungsten: Thermal or nonthermal process. *Phys. Rev. B* **94**, 224103, 2016. DOI: 10.1103/PhysRevB.94.224103 (see p. 63).

[84] R. LEONHARDT. Aufbau und Charakterisierung eines zweidimensionalen Galvanometersystems. Bachelor Thesis. Technische Universität Darmstadt, 2016. (see p. 66–69).

[85] *Interchangeable Variable Block Data Format for Positioning, Contouring, and Contouring/Positioning Numerically Controlled Machines*. Standard 2001 Eye Street, NW, Washington, D.C.: Electronic Industries Association., 1979 (see p. 68).

[86] Techspec: variable beam expander instructions. Edmund Optics Ltd. URL: https://www.edmundoptics.de/document/download/395858 (accessed 01 April 2018) (see p. 70).

[87] W. DEMTRÖDER. Experimentalphysik 2 (Elektrizität und Optik). Springer, 2013. DOI: 10.1007/978-3-642-29944-5 (see p. 73, 76).

[88] Arduino Uno. Arduino AG. URL: https://www.farnell.com/datasheets/1682209.pdf (accessed 01 April 2018) (see p. 73, 75).

[89] J. NETHERCOTT Capacitance measurement with the Arduino Uno. URL: http://wordpress.codewrite.co.uk/pic/2014/01/21/cap-meter-with-arduino-uno/ (accessed 01 April 2018) (see p. 73).

[90] MS5803-01BA Miniature Variometer Module. TE Connectivity Corporation. URL: http://www.te.com/deu-de/product-CAT-BLPS0038.html?q=MS5803-01BA&source=header (accessed 01 April 2018) (see p. 75).

[91] Sensofar PLu neox. Sensofar Metrology. URL: https://www.sensofar.com/metrology/ (accessed 01 April 2018) (see p. 75).

[92] A. FINE, W. B. AMOS, R. M. DURBIN, and P. A. MCNAUGHTON. Confocal microscopy: applications in neurobiology. *Trends Neurosci.* **11**, 346–351, 1988. DOI: 10.1016/0166-2236(88)90056-2 (see p. 76).

[93] P. W. HAWKES, J. C. H. SPENCE, and R. REICHELT. Scanning Electron Microscopy. Springer, 2007. 133–272 DOI: 10.1007/978-0-387-49762-4_3 (see p. 76).

[94] J. T. Zhu, Y. F. Shen, W. Li, X. Chen, G. Yin, D. Y. Chen, and L. Zhao. Effect of polarization on femtosecond laser pulses structuring silicon surface. *Appl. Surf. Sci.* **252**, 2752–2756, 2006. doi: 10.1016/j.apsusc.2005.04.048 (see p. 80).

[95] I. Musgrave, M. Galimberti, A. Boyle, C. Hernandez-Gomez, A. Kidd, B. Parry, D. Pepler, T. Winstone, and J. Collier. Review of laser diagnostics at the Vulcan laser facility. *High Power Laser Sci. Eng.* **3**, e26, 2015. doi: 10.1017/hpl.2015.27 (see p. 92).

[96] X. Wang, Z. H. Shen, J. Lu, and X. W. Ni. Laser-induced damage threshold of silicon in millisecond, nanosecond, and picosecond regimes. *J. Appl. Phys.* **108**, 033103, 2010. doi: 10.1063/1.3466996 (see p. 93).

[97] V. Bagnoud and F. Wagner. Ultrahigh temporal contrast performance of the PHELIX petawatt facility. *High Power Laser Sci. Eng.* **4**, e39, 2016. doi: 10.1017/hpl.2016.38 (see p. 94).

[98] B. Hidding, G. Pretzler, M. Clever, F. Brandl, F. Zamponi, A. Lübcke, T. Kämpfer, I. Uschmann, E. Förster, U. Schramm, R. Sauerbrey, E. Kroupp, L. Veisz, K. Schmid, S. Benavides, and S. Karsch. Novel method for characterizing relativistic electron beams in a harsh laser-plasma environment. *Rev. Sci. Instrum.* **78**, 083301, 2007. doi: 10.1063/1.2775668 (see p. 102).

[99] B. R. Maddox, H. S. Park, B. A. Remington, N. Izumi, S. Chen, C. Chen, G. Kimminau, Z. Ali, M. J. Haugh, and Q. Ma. High-energy x-ray backlighter spectrum measurements using calibrated image plates. *Rev. Sci. Instrum.* **82**, 023111, 2011. doi: 10.1063/1.3531979 (see p. 102).

[100] A. L. Meadowcroft, C. D. Bentley, and E. N. Stott. Evaluation of the sensitivity and fading characteristics of an image plate system for x-ray diagnostics. *Rev. Sci. Instrum.* **79**, 113102, 2008. doi: 10.1063/1.3013123 (see p. 102).

[101] C. G. Freeman, G. Fiksel, C. Stoeckl, N. Sinenian, M. J. Canfield, G. B. Graeper, A. T. Lombardo, C. R. Stillman, S. J. Padalino, C. Mileham, T. C. Sangster, and J. A. Frenje. Calibration of a Thomson parabola ion spectrometer and Fujifilm imaging plate detectors for protons, deuterons, and alpha particles. *Rev. Sci. Instrum.* **82**, 073301, 2011. doi: 10.1063/1.3606446 (see p. 102).

[102] K. A. TANAKA, T. YABUUCHI, T. SATO, R. KODAMA, Y. KITAGAWA, T. TAKAHASHI, T. IKEDA, Y. HONDA, and S. OKUDA. Calibration of imaging plate for high energy electron spectrometer. *Rev. Sci. Instrum.* **76**, 013507, 2005. DOI: 10.1063/1.1824371 (see p. 102).

[103] G. J. WILLIAMS, B. R. MADDOX, H. CHEN, S. KOJIMA, and M. MILLECCHIA. Calibration and equivalency analysis of image plate scanners. *Rev. Sci. Instrum.* **85**, 11E604, 2014. DOI: 10.1063/1.4886390 (see p. 103).

[104] T. BONNET, M. COMET, D. DENIS-PETIT, F. GOBET, F. HANNACHI, M. TARISIEN, M. VERSTEEGEN, and M. M. ALÉONARD. Response functions of imaging plates to photons, electrons and 4He particles. *Rev. Sci. Instrum.* **84**, 103510, 2013. DOI: 10.1063/1.4826084 (see p. 103).

[105] Gafchromic HDV2. Ashland Global Speciality Inc. URL: http://www.gafchromic.com/documents/gafchromic-hdv2.pdf (accessed 01 April 2018) (see p. 104).

[106] GafChromic EBT3. Ashland Global Speciality Inc. URL: http://www.gafchromic . com / documents / EBT3 _ Specifications . pdf (accessed 01 April 2018) (see p. 104).

[107] J. L. BASDEVANT, J. RICH, and M. SPIRO. Fundamentals In Nuclear Physics. 2nd ed. Springer, 2005. (see p. 104).

[108] A. SCHREIBER. RGB-Farbkalibrierung von radiochromatischen Filmen. Bachelor Thesis. Technische Universität Darmstadt, 2012. (see p. 105).

[109] R. J. GRAY, X. H. YUAN, D. C. CARROLL, C. M. BRENNER, M. COURY, M. N. QUINN, O. TRESCA, B. ZIELBAUER, B. AURAND, V. BAGNOUD, J. FILS, T. KÜHL, X. X. LIN, C. LI, Y. T. LI, M. ROTH, D. NEELY, and P. MCKENNA. Surface transport of energetic electrons in intense picosecond laser-foil interactions. *Appl. Phys. Lett.* **99**, 171502, 2011. DOI: 10.1063/1.3655909 (see p. 105).

[110] E. MARTINOLLI, M. KOENIG, J. M. BOUDENNE, E. PERELLI, D. BATANI, and T. A. HALL. Conical crystal spectrograph for high brightness x-ray Ka spectroscopy in subpicosecond laser-solid interaction. *Rev. Sci. Instrum.* **75**, 2024–2028, 2004. DOI: 10.1063/1.1753098 (see p. 108).

[111] T. A. HALL. A focusing x-ray crystal spectrograph. *J. Phys. E Sci. Instrum.* **17**, 110, 1984. (see p. 108).

[112] J. J. THOMSON. XXVI. Rays of positive electricity. *Philos. Mag. Ser. 6* **21**, 225–249, 1911. DOI: 10.1080/14786440208637024 (see p. 114).

[113] A. ALEJO, D. GWYNNE, D. DORIA, H. AHMED, D. C. CARROLL, R. J. CLARKE, D. NEELY, G. G. SCOTT, M. BORGHESI, and S. KAR. Recent developments in the Thomson Parabola Spectrometer diagnostic for laser-driven multi-species ion sources. *J. Instrum.* **11**, C10005, 2016. DOI: 10.1088/1748-0221/11/10/C10005 (see p. 114, 115).

[114] J. COLGAN, J. ABDALLAH, A. Ya FAENOV, S. A. PIKUZ, E. WAGENAARS, N. BOOTH, O. CULFA, R. J. DANCE, R. G. EVANS, R. J. GRAY, T. KAEMPFER, K. L. LANCASTER, P. MCKENNA, A. L. ROSSALL, I. Yu SKOBELEV, K. S. SCHULZE, I. USCHMANN, A. G. ZHIDKOV, and N. C. WOOLSEY. Exotic dense-matter states pumped by a relativistic laser plasma in the radiation-dominated regime. *Phys. Rev. Lett.* **110**, 125001, 2013. DOI: 10.1103/PhysRevLett.110.125001 (see p. 130).

[115] S. B. HANSEN, J. COLGAN, A. Ya FAENOV, J. ABDALLAH, S. A. PIKUZ, I. Yu SKOBELEV, E. WAGENAARS, N. BOOTH, O. CULFA, R. J. DANCE, G. J. TALLENTS, R. G. EVANS, R. J. GRAY, T. KAEMPFER, K. L. LANCASTER, P. MCKENNA, A. K. ROSSALL, K. S. SCHULZE, I. USCHMANN, A. G. ZHIDKOV, and N. C. WOOLSEY. Detailed analysis of hollow ions spectra from dense matter pumped by X-ray emission of relativistic laser plasma. *Phys. Plasmas* **21**, 031213, 2014. DOI: 10.1063/1.4865227 (see p. 130).

Acknowledgements

Zum Schluss dieser Arbeit möchte ich mich bei allen Personen bedanken, die zu meiner Promotion auf vielfältige Weise beigetragen haben.

Allen voran möchte ich Dr. GABRIEL SCHAUMANN danken. Du hast mich nicht nur motiviert eine Doktorarbeit im Detekor- und Targetlabor zu wagen, sondern stehst mir täglich mit Rat und Tat bei, nicht nur als Mentor und Laborleiter, insbesondere als verlässlicher Freund und Gefährte!

Ich danke Prof. Dr. MARKUS ROTH für die Möglichkeit die Arbeit in seiner Gruppe durchzuführen. Du hast bei mir mit der Ausrichtung der Doktorarbeit genau ins Schwarze getroffen! Die Möglichkeit an einem eigenständigen Projekt mit allen Freiheiten forschen und zu jedem noch so fernen Ziel reisen zu dürfen, erachte ich nicht als selbstverständlich. Ich danke dir für eine lange Leine und das Vertrauen, welches Du deinen großen und kleinen *Minions* zugestehst, während du im Ernstfall jederzeit ein offenes Ohr und Lösungsansätze bereithälst.

Ich danke Prof. Dr. THOMAS WALTHER für mehr als zehn Jahre Begeisterung für *Saturday Morning Physics* und die Möglichkeit interessierte Schülerinnen und Schüler für Physik zu motivieren. Darüber hinaus freue ich mich über die Bereitschaft meine Dissertation als Zweitgutachter mit Zeit und Mühe zu unterstützen. Prof. Dr. REINHOLD WALSER und Prof. Dr. MICHAEL VOGEL danke ich für Zeit und Arbeit als Prüfer, das ist bei Weitem nicht selbstverständlich.

Ohne meine Studentinnen und Studenten, deren Arbeiten ich im Labor und darüber hinaus betreuen durfte, wäre diese Arbeit *so* nicht möglich gewesen. Besonderen Dank möchte ich TINA EBERT aussprechen. Du hast mich im Verlauf deiner Masterarbeit über ein Jahr nicht nur motiviert, sondern jeden Tag aufs Neue angespornt neue Dinge auszuprobieren und zu wagen. Mit dir habe ich die fähigste Kandidatin für den Ausbau und die Nachfolge meiner experimentellen Arbeit gefunden. Auch meinen Bachelorküken LAURA-DESIREE GEULIG und RENÉ LEONHARDT bin ich für die Unterstützung im Verlauf ihrer Arbeiten voll freudiger Neugierde dankbar.

Von morgens bis abends gemeinsam zu arbeiten ist das Eine. Sechs volle Wochen aufzubringen um mit einem dickköpfigen Kollegen zum Experimentieren auf eine verregnete Insel zu fliegen, ein ganz besonderes Eingeständnis! Ich

bin TINA EBERT, MARKUS HESSE und ALEXANDRA TEBARTZ in großer Anerkennung und von tiefstem Herzen unendlich zum Dank verpflichtet. Ohne Euch als Team an meiner Seite wäre ich an mir und der Strahlzeit verzweifelt. Ich danke LEO DÖHL, JONATHAN JARRETT, DEAN RUSBY, AASIA HUGHES, DAVID NEELY, PAUL MCKENNA, NIGEL WOOLSEY, und vielen weiteren mehr für die Unterstützung meiner Kampagne in England. Der Central Laser Facility und dem englischen Steuerzahler zudem für das Ermöglichen dieses erfolgreichen und umfangreichen Experiments.
Dabei zuhause geblieben, danke ich meinen zahlreichen Kollegen, allen voran TORSTEN ABEL, ROBERT JÄGER, STEFFEN SANDER, DIANA JAHN, uvm. Mit euch habe ich wunderbare und produktive Stunden verbracht und konnte mich stets auf Hilfe verlassen. Darüberhinaus gilt mein Dank der feinmechanischen Werkstatt und der elektrotechnischen Werkstatt, die jederzeit für eine direkte Problemlösung verfügbar waren.
Kollegen kann man sich mit der Wahl der Arbeitsgruppe aussuchen (das hat hier gut geklappt!). Ein großes familiäres Umfeld ist mir gegeben und ein riesiges Glück. Meinem Großvater GERHARD NEUMANN (Vermieter und ältestem Mitbewohner) verdanke ich die Anerkennung einer fundierten schulischen und wissenschaftlichen Ausbildung (Letzteres war ihm verwehrt). Meinem Vater, ULRICH NEUMANN, verdanke ich bedingungslose Unterstützung während der Doktorarbeit, einen wunderbaren Freund und meine von Neugier getriebene und experimentelle Art. Meinen Geschwistern CATHERINE SENN, TILL NEUMANN und TIMO NEUMANN danke ich ebenfalls für die Unterstützung und ihr Vertrauen. Mit OLE SENN habe ich zudem einen Neffen (und Patenkind) geschenkt bekommen, der mich mit seiner kindlichen Neugier inspiriert und auf neue Gedanken bringt.

> *The highest forms of understanding we can achieve are laughter and human compassion.*"
>
> – RICHARD P. FEYNMAN

Seit den ersten Semestern des Physikstudiums, durch die Doktorarbeit und darüber hinaus verbindet mich die Freundschaft mit TOBIAS EGGERT, DOMINIK GEIST, JULIUS GRONEFELD, SEBASTIAN FISCHER, MICHAELA HAMM, DIRK HEINEN, LARS JÜRGENSEN, MICHÈLE KLEIN, LEA KUHN, JONAS LÖBIG, MICHAEL PRASCH, STEFAN SCHÜRL und insbesondere ROBERT STEGMANN. Auf eure Hilfestellungen kann ich bauen. Mit euch kann ich lachen, Abenteuer erleben und den Alltag hinter mir lassen.

Mit Torsten Abel, Marvin Groeb, Markus Hesse, Sebastian Hundertmark, Stefan Koitzsch, Stefan Krippner, Gabriel Schaumann, Christoph Wagner, Tobias Weber und Stefan Zucca habe ich wunderbare Freunde gefunden und mit 99 weiteren Mitgliedern unseres gemeinnützigen Werkstattprojekts *Makerspace Darmstadt e.V.* einen Traum der Zusammenarbeit, des Selbermachens und voneinander Lernens verwirklicht.
Zudem möchte ich allen weiteren Freunden, Verwandten, Bekannten und Wegbereitern für ihre Unterstützung danken.

Physics isn't the most important thing. Love is."

– Richard P. Feynman

Von Antje Neumann habe ich gelernt das Beste zum Schluss aufzuheben und Perfektion und Struktur an den Tag zu legen, für Dinge die ich liebe und schätze. Mit dir habe ich nicht nur, seit bald 12 Jahren, eine unschlagbare Partnerin, Seelenverwandte und beste Freundin gefunden. Seit dem 22. Juli 2016, in der Hochphase meiner Promotion, bist Du meine Frau und ich genieße und freue mich über jeden Tag an deiner Seite und die gegenseitige Unterstützung. Mit dir kann ich nicht nur das Leben und die weite Welt in wunderbaren Reisen entdecken. Durch dich verschwende ich nicht einen Gedanken an eine unsichere Zukunft, weil ich weiß was noch für wunderbare Momente und Dinge kommen werden.
Es geht nicht um Physik. Es geht um Fantasie und Neugierde.

Nico Wilfrid Neumann
Darmstadt im Mai 2018

This work received financial support by the DFG in the framework of the Excellence Initiative, Darmstadt Graduate School of Excellence Energy Science and Engineering (GSC 1070).

Erklärung zur Dissertation

Hiermit versichere ich, die vorliegende Dissertation ohne Hilfe Dritter nur mit den angegebenen Quellen und Hilfsmitteln angefertigt zu haben. Alle Stellen, die aus Quellen entnommen wurden, sind als solche kenntlich gemacht. Diese Arbeit hat in gleicher oder ähnlicher Form noch keiner Prüfungsbehörde vorgelegen.

Darmstadt, den 8. Mai 2018

(Nico Wilfrid Neumann)